

**Improved Heat Assisted Magnetic Recording via Ultrathin  
Nonlocal Spin Valves and Three-Layer Composite Media**

**A DISSERTATION  
SUBMITTED TO THE FACULTY OF THE GRADUATE SCHOOL  
OF THE UNIVERSITY OF MINNESOTA  
BY**

**Yijia Liu**

**IN PARTIAL FULFILLMENT OF THE REQUIREMENTS  
FOR THE DEGREE OF  
Doctor of Philosophy**

**Advisor: Randall H. Victora**

**August, 2024**

© Yijia Liu 2024  
ALL RIGHTS RESERVED

# Acknowledgements

Reflecting on this doctoral journey, I would characterize it as transformative experience, defined by various challenges, perseverance and intellectual and personal growth. I feel privileged that this enduring and rewarding journey have been witnessed and supported by intelligent, compassionate, and encouraging individuals whose support and guidance been significant to me. This endeavor would not have been possible without them.

First and foremost, my immense gratitude goes to my supervisor, Prof. Randall H. Victora whose mentorship has been indispensable to my doctoral journey. Prof. Victora has not only provided me with invaluable opportunity to delve into the rigorous scientific realm with him but also has been an inspiring role model demonstrating me dedication, passion, and unwavering commitment to excellence. His profound wisdom, expertise, encouragement and patience have guided me through the challenges of my research and refining my work as well as nurturing a resilient and optimistic mindset, motivating me to excel academically and personally.

I would also like to express my gratitude the members of my doctoral committee for their time and insightful feedback, which significantly contributed to the refinement of this dissertation. In particular, I extend my sincere appreciation to Prof. Jorge Viñals for his advice and guidance during the early stages of my doctoral journey.

Furthermore, I would also like to thank Professor Chris Leighton, Dr. Justin Watts, Dr. Ganping Gu, Benjamin Kaiser, Dr. Niranjana Natekar, Kun Xue and Yifei Chen for the constructive discussions on my research projects which are integral to this endeavor.

I am also grateful to my colleagues, fellow graduate students, including Runzi Hao, Shuang Liang, Kun Xue, Yifei Chen, Kamal Hosen, Dr. Tao Qu, Dr. Rizvi Ahmed, Dr. Wei-Heng Hsu, Dr. Niranjana Natekar and Dr. Aneesh Venugopal. Their friendship, moral support, and academic exchange have enriched my doctoral experience and

made it truly memorable. Special thanks to Dr. Wei-Heng Hsu for his mentorship and constant guidance throughout my time in Prof. Victora's research group.

I am also indebted to my friends Xintian Sun, Lichen Zhang, Yishi Ping, Yibo Chang and Kai Zhang. Their camaraderie, companion and encouragements help me navigate through the ups and downs during my doctoral life.

Last but not least, I would like to express my heartfelt gratitude to my family for their unconditional love, encouragement, support and understanding, carrying me throughout this journey.

# Dedication

To my family, who have always believed in me and supported me at every step of my journey, and to all the people who have offered their guidance, patience, wisdom, encouragement, camaraderie and intellectual exchanges that have been invaluable throughout this journey.

## Abstract

This dissertation is structured into two main parts, dedicated to exploring potential optimizations in read head and recording media, two integral hard disk drive (HDD) components, for achieving reliable recording performance with high areal density.

The first part delves into the complexity of transport within Al-based Nonlocal Spin Valves (NLSVs), particularly addressing spin relaxation induced by structural defects in the material. This can significantly enhance the spin relaxation and is likely responsible for the observed deteriorated performance of the devices, especially notable for metallic channels thinner than 10nm. To exclusively study the spin relaxation induced by surface and bulk defects, all the calculations are implemented at  $T=0K$  to eliminate temperature-dependent contributions such as phonon scattering. Resistivity, spin diffusion length and Elliott-Yafet constant  $\beta$  are determined in a simplified 3.6nm-thick Al-system where both leads and transport channel are made of Al and embedded in vacuum.

Utilizing the Landauer-Büttiker formalism and a recursive Green's function technique, predictions are made regarding the effects of surface and bulk scattering on electronic and spin transport including surface roughness, grain boundaries, vacancies, and surface reconstruction. It is demonstrated that for thin sputtered films, point vacancies contribute dominantly to the momentum relaxation, and spin relaxation is dominated by the combined effect of surface reconstruction and point vacancies. This yields reasonable spin diffusion lengths and Elliott-Yafet constants. Further analysis reveals that the presence of surface corrugations leads to a clear departure from Matthiessen's rule and the Elliott-Yafet prediction of  $\beta$ . However, this deviation is rectified in the presence of random surface corrugations with higher vacancy concentration, as the symmetry breaking is closely dependent on the characteristic scattering length and concentration of random defects.

It is discovered that the spin diffusion length induced by surface roughness is proportional to the inverse square root of the ratio between the root mean square height ( $\delta h$ ) and the lateral correlation length ( $\xi$ ) of a given rough surface, i.e.  $(\delta h/\xi)^{-1/2}$ , as opposed to  $(\delta h/\xi)^{-1}$  as is the mean free path. This phenomenon is attributed to the

interference of extended surface features. Additionally, a pronounced anisotropy of spin relaxation is observed for spins parallel to the propagation direction, which is pertinent to surface corrugations. Overall, these findings can potentially facilitate the realization of magnetic recording read heads based on metallic nonlocal spin valves with sub-10nm shield-to-shield spacing, thereby improving head resolution.

The second part of the dissertation shifts focus toward mitigating transition noise with a novel proposed heat-assisted magnetic recording (HAMR) media in order to achieve higher areal density of HAMR-based devices. Conventional two-layer thermally exchange coupled composition media (ECC) exhibit robust tolerance to noise induced by  $T_c$  variance and offer tunability of writing temperature but suffer from adjacent track interference issue with reduced writing temperature. To inherit these merits while addressing the thermal susceptibility, the recording performance of three-layer (3-ly) FePt-based ECC structure with reduced  $T_c = 500$  K for FePt is evaluated, with predictions for transition jitter, erasure-after-write (EAW), bit error rate and switching probability distribution. The original two-layer ECC structure features a magnetic soft writing layer with high  $T_c$  and a magnetic hard FePt-layer for long-term storage. In contrast, the proposed three-layer structure consists of a high- $M_s$  and moderate- $K_u$  writing layer, a middle layer with the same  $K_u$  as FePt but low- $M_s$  and a FePt layer attached at the bottom, each layer being 3nm thick. The optimized parameters at 300K for the writing layer are  $M_s = 1300$  emu/cm<sup>3</sup> and  $K_u = 1.3 - 1.8 \times 10^7$  erg/cm<sup>3</sup> and  $T_c = 600$  K and  $M_s = \sim 350$  emu/cm<sup>3</sup> and  $K_u = 3.3 \times 10^7$  erg/cm<sup>3</sup> at 300 K and  $T_c = 500$  K for the middle layer.

Compared to the conventional 2ly-ECC, the switching mechanism for proposed 3ly-ECC highlights the Zeeman effect that switches the writing layer and anisotropy field gradients to switch the middle layer. By decoupling the Zeeman effect and anisotropy field gradients, the proposed 3ly-ECCs effectively improve transition jitter by  $\sim 15\%$  and BER by  $\sim 85\%$  in the absence of intergranular exchange, compared to 2ly-ECC with the same total thickness. These improvements are attributed to large anisotropy and small magnetization in the middle layer, aligning with the analytical analysis of energy function based on a simple spin model.

In addition, the exploration of the switching rate at a constant temperature suggests that fast switching induced by the moderately soft writing layer can also potentially contribute to jitter improvement at the expense of enhanced EAW. It is also observed that the 3ly-ECC is more susceptible to EAW effect than 2ly-ECC. Calculations indicate that the suppression of EAW in 3ly-ECCs relies on the increase in the anisotropy of writing layer which adversely affects BER due to the loss of rapid switching. Overall, the proposed 3ly-ECCs effectively balance fast switching and EAW and thus exhibit superior jitters and BERs compared to the two-layer counterpart.



# Contents

<b>Acknowledgements</b>	<b>i</b>
<b>Dedication</b>	<b>iii</b>
<b>Abstract</b>	<b>iv</b>
<b>List of Tables</b>	<b>x</b>
<b>List of Figures</b>	<b>xii</b>
<b>1 Part I: Spin Transport</b>	<b>1</b>
1.1 Spintronics . . . . .	1
1.1.1 GMR . . . . .	2
1.1.2 Non-Local Spin Valve . . . . .	5
1.2 Elliott-Yafet theory . . . . .	7
1.2.1 Challenges for Al . . . . .	11
1.2.2 Spin hot spots . . . . .	12
1.2.3 Size effect on metallic NLSV . . . . .	13
1.3 Outline . . . . .	15
<b>2 Modeling Methods for Electron and Spin Transport</b>	<b>16</b>
2.1 Landauer-Büttiker formalism and Transmission Function . . . . .	16
2.1.1 Landauer-Büttiker formalism . . . . .	18
2.1.2 Recursive Green's Function Method . . . . .	21
2.1.3 Tight-Binding Model . . . . .	25

<b>3</b>	<b>Electron and Spin transport in ultra-thin Al films</b>	<b>28</b>
3.1	Introduction . . . . .	28
3.2	Methods . . . . .	29
3.3	Preliminary Results . . . . .	31
3.4	Results and Discussion . . . . .	34
3.4.1	Surface Roughness . . . . .	34
3.4.2	Grain Boundary Scattering . . . . .	38
3.4.3	Vacancy Scattering . . . . .	41
3.4.4	Surface Reconstruction . . . . .	46
3.4.5	Anisotropy of Spin Relaxation . . . . .	51
3.4.6	Spin Hot Spots . . . . .	52
3.5	Conclusion . . . . .	53
<b>4</b>	<b>Part II: Micromagnetics</b>	<b>54</b>
4.1	History of Hard Disk Drives . . . . .	54
4.1.1	Structure of HDDs . . . . .	56
4.2	Magnetic Recording Trilemma . . . . .	57
4.3	From LMR to PMR to HAMR . . . . .	58
4.3.1	HAMR . . . . .	59
4.3.2	HAMR Media . . . . .	62
4.3.3	Noise in HAMR . . . . .	64
4.3.4	Thermal exchange coupled composite media . . . . .	65
4.3.5	Low-T ECC . . . . .	70
4.3.6	Adjacent Track Erasure (ATE) . . . . .	71
4.3.7	Outline . . . . .	72
<b>5</b>	<b>Modeling Methods of Magnetic Recording</b>	<b>74</b>
5.1	LLG equation . . . . .	74
5.2	Numerical Implementation of LLG equation . . . . .	75
5.2.1	Hamiltonian of a spin system . . . . .	76
5.2.2	Crystalline Anistropy Energy . . . . .	77
5.2.3	Exchange field . . . . .	77
5.2.4	Magnetostatic Energy . . . . .	79

5.2.5	Thermal agitation field . . . . .	80
5.2.6	Zeeman Energy . . . . .	81
5.3	Renormalization method for HAMR . . . . .	81
5.4	Voronoi Media . . . . .	83
5.5	Recording Process . . . . .	84
5.6	Readback Process . . . . .	85
<b>6</b>	<b>Reducing Transition Jitter with Composite Media for HAMR</b>	<b>87</b>
6.1	Introduction . . . . .	87
6.2	Methods . . . . .	88
6.3	Results and Discussions . . . . .	91
6.3.1	Transition Jitter . . . . .	91
6.3.2	Erasure-After-Write effect . . . . .	102
6.3.3	Switching Rate . . . . .	104
6.3.4	BER . . . . .	105
6.3.5	SPD . . . . .	107
6.4	Conclusion . . . . .	108
	<b>References</b>	<b>109</b>

# List of Tables

3.1	Summary of the effect of surface roughness on electric and spin transport in a 3.6 nm-thickness Al film at $T = 0$ K. . . . .	37
3.2	Summary of the effect of grain boundaries on electric and spin transport in a 3.6 nm-thickness Al film at $T = 0$ K. . . . .	38
3.3	Summary of the effect of 2% vacancies on spin transport in an Al film with 3.6 nm thickness at $T = 0$ K. . . . .	42
3.4	Summary of resistivity induced by vacancies at $t_N = 3.6$ nm and $T = 0$ K. . . . .	43
3.5	Summary of the effect of surface reconstruction on electric and spin transport in an Al film with 3.6 nm thickness at $T = 0$ K. . . . .	46
3.6	Summary of anisotropy of spin transport in an 3.6nm thick Al film with 0.4 nm periodicity of surface corrugation and 0.8% vacancies or 2% vacancies alone at $T=0$ K. . . . .	51
3.7	Summary of the experimental results on spin transport in Al-NLSV at $T= 4$ K (Adapted from Ref.[52]) . . . . .	52
4.1	A list of high-Ku magnetic materials from Ref. [108]. . . . .	63
4.2	Magnetic parameters in two different designs of thermal ECC media at 300 K [121]. . . . .	70
4.3	Adjacent track erasure evaluated with different HAMR media. . . . .	72
6.1	Summary of Transition Jitter for $T_{c1} = 560$ K and 0% IGE. . . . .	93
6.2	Summary of Transition Jitter for $T_{c1} = 600$ K and 0% IGE. Note that All the Associated Errors are within 3%. . . . .	93
6.3	Summary of Transition Jitter for $T_{c1} = 630$ K and 0% IGE. Note that All the Associated Errors are within 3%. . . . .	94
6.4	Summary of the Optimized 3ly-ECC's Configurations. . . . .	94

6.5	Summary of Transition Jitters of 3LYs and 2LY-ECC at Different Shield to Shield Spacing with IGE = 0 and 5%. . . . .	95
6.6	Summary of EAW for 3Lys and 2Ly-ECC in the Presence/Absence of IGE.	102
6.7	Summary of BERs of 3LYs and 2LY-ECC at Different Shield to Shield Spacing with IGE = 0 and 5%. . . . .	107

# List of Figures

1.1	The GMR results founded by Albert Fert group: change in the resistance of Fe/Cr superlattices at 4.2 K in an external magnetic field $\vec{H}$ . The current and magnetic field were along the same in-plane axis. $H_s$ is saturation field (left); the GMR founded by Peter Grünberg group at room temperature with Fe-Cr-Fe trilayer (right). . . . .	2
1.2	An illustration of GMR effect in a trilayer structure with the two-current model and circuit diagrams. a. parallel configuration with low resistance; b. anti-parallel configuration with high resistance. [5] . . . . .	3
1.3	Geometry of NLSV; $F_1$ and $F_2$ separated by distance L, serve as spin injector and spin detector, respectively. Note that the charge current is designed to flow toward the opposite direction. . . . .	5
1.4	The dependence of MR ratio on RA product of metallic and tunneling spin valves hints the potential of metallic spin valves to meet the high areal density requirements of HDDs. . . . .	6
1.5	The schematic illustration of the locations for spin “hot spots” on Fermi surface of polyvalent metal. Color violet, blue green, yellow and red represent the increase in intensity of spin relaxation. Adpated from Ref. [40]. . . . .	12
2.1	A schematic diagram for the system sliced layer by layer, where L, R and S stand for the left lead, the right lead and the scattering region in the Landauer-Büttiker formalism. A principal layer consisting of two atomic layers is included in the Hamilton of the system with second nearest neighbor interaction. . . . .	17

3.1	Schematic of the transport model in the presence of surface roughness and vacancies. L denotes the left lead and R denotes the right lead. To simulate the surface roughness, twice of $\delta h$ is included in both leads and scattering region for surface bumps. The yellow region indicates the positions with 5 Ry added to simulate the vacuum environment. The white circles represent vacancies, which is achieved with 1.5 Ry onsite-offset potential exerted. Note that the transport model shown here is for visualization and the actual dimensions and scales of each region may vary.	30
3.2	Transmission function for the linear chain (onsite energy $E = 0$ , coupling $t = 1$ ) without defects and with a single defect at $\epsilon = 0.5$ and $\epsilon = 0.8$ .	31
3.3	Transmittance of an infinite plane with a groove defect at $\epsilon = 0.5$	32
3.4	Density of states computed by Green's function technique with $\delta = 0.002$ and by counting the numbers of states at each energy level through diagonalizing the Hamiltonian.	33
3.5	(a) Resistivity of Al with 3.6 nm thickness versus channel length under different sets of surface roughness parameters. (b) Spin diffusion lengths under the same sets of roughness parameters as above. P is the spin polarization.	36
3.6	Resistivity of 3.6 nm thick film varies with $\delta h/\xi$ in blue and the corresponding $\beta$ in red. The fitting dashed lines are used to show the linear trend. Note that the larger error bar for $\delta h/\xi = 0.05$ is due to the weak tunneling effect.	37
3.7	(a) Resistivity of 3.6 nm thick film versus channel length for different grain boundary parameters. (b) Spin diffusion lengths for a 3.6 nm thick channel under the same sets of grain boundary parameters as above.	39

3.8	(a) Resistivity of 3.6 nm thick film versus channel length with 2% line vacancies (with surf.1) in purple (blue) and 2% point vacancies (with surf.1) in yellow (red); surface 1 is modulated by $\delta h = 0.8$ nm and $\xi = 20$ nm. Note that the case with the 2% line vacancies and surface 1 is only plotted to 250nm because the strong tunneling effect makes the transmission function too small to acquire an accurate resistivity. (b) Spin diffusion lengths for a 3.6 nm thick channel under the same condition as above. . . . .	41
3.9	Resistivity of 3.6 nm thick film varies with $C_{vac}$ in blue; the linear fitting on $C_{vac}$ in a red dashed line and the quadratic fitting on $C_{vac}$ in a yellow dashed line with the fitting equation $y = 284.2x(1 - 6.56x)$ . . . . .	45
3.10	(a) Resistivity of 3.6 nm thick film versus channel length in the presence of periodic surface corrugations/random surface corrugations and 0.1%, 0.4% point vacancies.(b) Spin diffusion lengths for a 3.6 nm thick film with varying widths of surface corrugation and varying vacancy concentration. . . . .	48
3.11	$L_{sd}$ versus $\rho^{-1}$ for all the cases shown in Table 3.5 except the case with PSC alone. The fitting equations are $y = 115.2x + 143$ for vacancies and PSC in the blue dash line and $y = 841x - 13.3$ for vacancies and RSC in the red dash line. The associated $\beta_{RSC+vac}$ is determined from the slope. . . . .	50
4.1	a. Areal density evolution of HDDs from Ref. [90]; b. the ASTC roadmap of areal density from Ref. [91]. . . . .	55
4.2	the basic structure of an HDD [97]. . . . .	56
4.3	The basic illustration of longitudinal magnetic recording and perpendicular magnetic recording from Ref. [103]. . . . .	59
4.4	The schematic of HAMR demonstrating its recording mechanism [104]. . . . .	60
4.5	a. A illustration of a "lollipop" NFT heating a HAMR media [107]; b. A PSIM converging light waves to NFT [106]. . . . .	61
4.6	A schematic drawing of HAMR media consisting of a recording layer and functional layers from Ref. [109]. . . . .	62



4.7	Typical HAMR noise contributors; a. $\sigma Tc$ and $\sigma H_k$ degrade transition jitters [113]; b. The Curie temperature dependence on grain size [114]; c. The grain geometry induced variation of power absorption [115]. . . . .	64
4.8	Illustration of switching mechanism in thermal ECC media initiated at different temperatures and cooled to 350 K (3rd column) [119]. . . . .	67
4.9	a. SPDs for conventional HAMR media and thermal ECC media [119]; b. The dependence of transition jitter on grain pitch for single-layer FePt and thermal ECC media [120]. . . . .	69
4.10	Transition jitters evaluated with high-T and low-T thermal ECC media at different grain pitches. . . . .	71
5.1	An illustration of the atomistic discretized (left) and coarse-grained (middle) 6-nm spin blocks with 0.3 nm and 1.5 nm-renormalized cells, respectively, along with the mapping from the renormalized cell to Voronoi media (right). . . . .	81
5.2	The renormalized parameters determined with different grid sizes [128].	82
5.3	An illustration of Bowyer-Watson algorithm [132]. . . . .	83
5.4	The dependence of down-track thermal gradient on heatsink (left) and the response of transition jitters to down-track thermal gradient (right) [133]. . . . .	85
6.1	Sketches of the proposed 3ly-ECC and 2ly-ECC [143] structure with total thickness of 9nm. The magnetic properties listed are evaluated at 300 K.	88
6.2	(a) Transition jitters comparison between 2ly-ECC and 3ly-ECCs at different SSSs in absence of IGE. (b) Transition jitters comparison between 2ly-ECC and 3ly-ECCs at different SSSs in the presence of 5% IGE. . .	91
6.3	Energy contour plots for 3ly-model at T = 420K (a), T=450K (b) and T=475K (c) from left to right, where critical points are labeled from A to I. $H_{appl}=7400$ Oe. $M_1(T) = 1600(1-T/560)^{1/3}$ , $K_1(T) = 2.4 \times 10^7(1-T/560)$ . $M_2(T) = 460(1-T/500)^{1/3}$ , $K_2(T) = 7.4 \times 10^7(1-T/500)$ . $M_3(T) = 1100(1-T/500)^{1/3}$ , $K_3(T) = 7.0 \times 10^7(1-T/500)$ . $J_{ex,1,2}/V = 4.8 \times 10^6 \text{erg/cm}^3$ and $J_{ex,2,3}/V = 4.6 \times 10^6 \text{erg/cm}^3$ . Note all the energy is scaled with $E/Ku_{3,0}V$ .	96

6.4	Energy contour plots for 2ly-model at $T = 420\text{K}$ (a), $T=450\text{K}$ (b) and $T= 470\text{K}$ (c) from left to right, where critical points are labeled from A to I. $H_{appl}=7400$ Oe. $M_1(T) = 960(1-T/600)^{1/3}$ , $K_1(T) = 1.8 \times 10^7(1-T/600)$ . $M_2(T) = 1100(1-T/500)^{1/3}$ , $K_2(T) = 7.0 \times 10^7(1-T/500)$ . $M_3(T) = 1100(1-T/500)^{1/3}$ , $K_3(T) = 7.0 \times 10^7(1-T/500)$ . $J_{ex,1,2}/V = 4.5 \times 10^6 \text{erg/cm}^3$ and $J_{ex,2,3}/V = 5.3 \times 10^6 \text{erg/cm}^3$ . Note all the energy is scaled with $E/Ku_{2,0}V$ .	98
6.5	The energy barrier AB $\Delta E_{AB}$ varies with temperature for 3ly-model in red and 2ly-model in blue. Inset: derivative of the fitting function of $\Delta E_{AB}(T)$ .	100
6.6	(a) Switching rate comparisons between 2ly-ECC and 3ly-ECCs in absence of IGE. (b) Switching rate comparison between 2ly-ECC and 3ly-ECCs in the presence of 5% IGE.	104
6.7	(a) BER comparisons between 2ly-ECC and 3ly-ECCs in absence of IGE.(b) BER comparison between 2ly-ECC and 3ly-ECCs in the presence of 5% IGE.	106
6.8	FWHM comparison between 2ly-ECC and 3ly-ECCs with/without IGE.	108

# Chapter 1

## Part I: Spin Transport

### 1.1 Spintronics

Spintronics, a revolutionary paradigm in electronics, may significantly broaden the functionality of electronic devices with the manipulation of the spin degree of freedom. In contrast to electronics, spintronics devices introduce unique spin-based features, promising to reduce electronics power consumption, increase the information processing capacities and speed and improve the integration density. Utilizing the spin alone or integrating it with current electronic devices, the application of spintronics device has been crucial in both scientific exploration and technological innovation. For instance, spin valves, used to discover giant magnetoresistance (GMR), initiated the study of magnetotransport and boosted the storage density in hard disk drives (HDD). Magnetic tunnel junctions (MTJ), composed of a pinned layer and a free layer separated by a thin insulating layer, widely serve as memory/storage device such as magnetic random access memory (MRAM) owing to its high tunneling magnetoresistance (TMR) and as magnetic sensors to probe spin-dependent phenomena.

Compared to semiconductor devices, spintronic devices can offer distinct advantages. Magnetic devices control the spin transport using nanometer-sized features, e.g. tunneling barriers, rather than using intrinsically formed depletion layers spanning from  $\sim nm$  to  $\sim \mu m$  as in semiconductors. This favors higher integration density. Moreover, its low resistivity, typically on the order of  $10^{-7}$  and  $10^{-8} \Omega \cdot m$  in magnetic metals, can significantly contribute to reduced power consumption because doping-controlled

resistivity in semiconducting devices are at least three order of magnitude higher [1, 2]. Furthermore, spin states can be rapidly configured, enabling fast access, processing and transfer of information. Additionally, electron spins are coupled by quantum mechanical exchange and thus spin-encoded data is non-volatile: information transmitted via spin remains intact even in the absence of power.

### 1.1.1 GMR

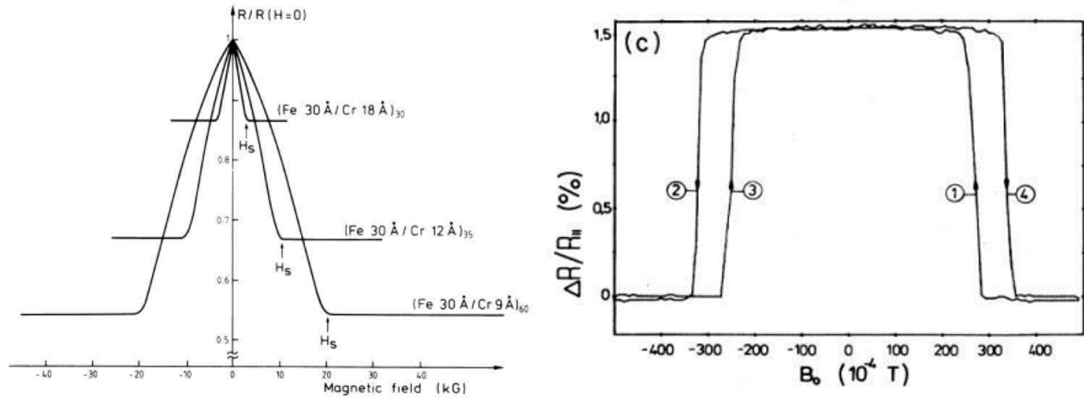


Figure 1.1: The GMR results founded by Albert Fert group: change in the resistance of Fe/Cr superlattices at 4.2 K in an external magnetic field  $\vec{H}$ . The current and magnetic field were along the same in-plane axis.  $H_s$  is saturation field (left); the GMR founded by Peter Grünberg group at room temperature with Fe-Cr-Fe trilayer (right).

Giant magnetoresistance (GMR) is a quantum mechanical effect, first discovered in a heterogeneous structure independently by two research groups lead by Fert [3] and Grünberg [4] in 1988. It was observed that magnetoresistance in multilayer structures consisting of alternate ferromagnetic and nonmagnetic layer is dependent on the relative magnetization of adjacent ferromagnetic layers. A simple GMR structure consists of two ferromagnetic layers separated by a non-magnetic layer forming a stacked structure as in Fig. 1.2, which is the prototype of spin valve. In this configuration, one of the ferromagnetic layers is pinned by an antiferromagnetic layer beneath it, while the magnetization of the other ferromagnetic layer is free to rotate under the external magnetic field. By

controlling the magnetization of the one ferromagnetic layer, the resistance of the GMR device varies accordingly: it exhibits low resistance for parallel magnetization of two ferromagnetic layer compared to antiparallel alignments. As a result, GMR device can generate binary output, making GMR-device promising for magnetic field sensors for signal detection and data storage.

The GMR ratio defined below serve as a critical measure evaluating the spin transport efficiency.

$$MR\% = \frac{\Delta R}{R} = \frac{(R_{AP} - R_P)}{R_P},$$

where  $R_P(R_{AP})$  denotes the resistance measured for parallel (antiparallel) orientations of two ferromagnetic layers. Notably, at low temperatures, the output GMR ratio exhibits a "giant" increase, much higher compared to anisotropic magnetoresistance (AMR).

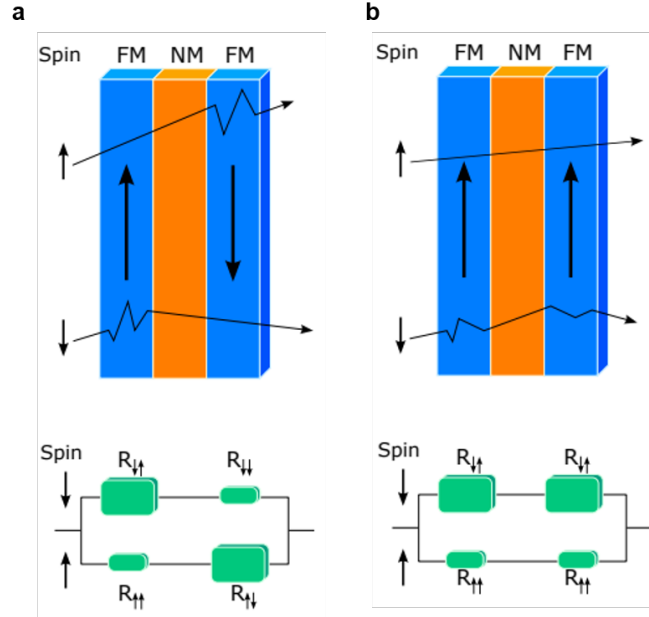


Figure 1.2: An illustration of GMR effect in a trilayer structure with the two-current model and circuit diagrams. a. parallel configuration with low resistance; b. anti-parallel configuration with high resistance. [5]

Two generally accepted explanations of the origin in GMR are based on Mott's

two current model and the Valet-Fert model (CPP) [6, 7]. Mott's two current model assumed that the conduction is dominantly through the s-electron such that the spin-mixing process is negligible (no mixing through spin-orbit coupling). This is particularly evident at the low-temperature limit where s-d interaction is further suppressed due to the absence of thermal agitation and hence the electron currents associated with two spin states can be assumed to be independently transported in ferromagnetic materials. For a magnetic transition metal, the s-d interaction generates two conduction sub-bands with varying mixing of s and d orbitals, contributing to the ferromagnetism and exchange-splitting of conduction bands. As a result, the density of states at the Fermi level differs for the spin majority and minority electrons due to this exchange-splitting. Specifically, the spin majority usually resides in the subband with less d-orbital contribution, leading to a smaller density of states (DOS) at the Fermi level than the DOS of spin minority in the sub-bands with higher d-orbital contribution.

Since the scattering rate depends on the density of state available for electrons to be scattered into, the scattering associated with the spin majority is usually weaker than that of the spin minority. Thus, for the parallel configuration, the overall resistance is primarily determined by the spin-majority channel of low resistance, which is also illustrated by the circuit diagram analogy as shown in Fig. 1.2. On the contrary, for the antiparallel configuration, the spin experiences scattering to the opposite spin direction such that the two independent scattering branches equally contribute to the total resistivity. Hence, in a GMR structure, the parallel magnetization configuration has a lower resistivity.

Experimentally, GMR has been observed in two different configurations: current-in-plane (CIP) and current-perpendicular-to-plane (CPP) geometries, which refers to the net charge current flowing in the planes of a layered structure or perpendicular to the layer structure, respectively [8, 9, 10]. Experimental results show that GMR ratio in the CPP geometry is usually larger than that obtained in the CIP geometry. Moreover, the characteristic thickness of non-magnetic (NM) spacer required to maintain the CPP-GMR is much longer than that for CIP-GMR [12].

Although the two current model effectively elucidates the fundamental transport phenomena of transition metals, the oversimplified assumption of independent spin-transport channels offers no insights on the spin mixing process in the bulk limit or

explanation on the GMR threshold spacer thickness to sustain GMR. In contrast, the Valet-Fert model provides a robust theoretical explanation of the CPP-GMR behavior based on the Boltzmann equation [7]. According to this model, when currents flow through the CPP-configuration, one spin species accumulates at the interface, resulting in the non-equilibrium in spin density [11, 13]. Subsequently, spin-flip scattering processes then work to restore the equilibrium between different spin channels, causing the spin accumulation to diminish from the interface, leading to CPP-GMR decay in an exponential-like fashion with the decay length determined by the spin-diffusion length.

### 1.1.2 Non-Local Spin Valve

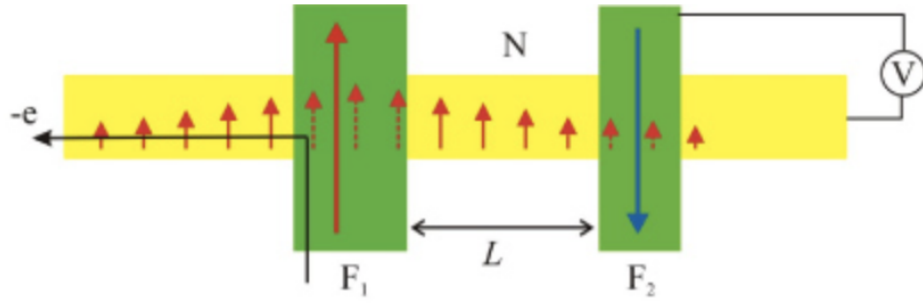


Figure 1.3: Geometry of NLSV;  $F_1$  and  $F_2$  separated by distance  $L$ , serve as spin injector and spin detector, respectively. Note that the charge current is designed to flow toward the opposite direction.

A spin valve as GMR-based magnetic device can potentially address the technical challenges such as efficient spin injection, transport and detection. Johnson first demonstrated the spin-injection into a normal metal (NM)-based spin valve [14, 15]. In 2000, Jedema et al. revitalized spin-injection research by employing a non-local geometry [15], as shown in Fig. 1.3.

Distinct from conventional spin valves that detect the spin and electronic signals at the same location, a non-local spin valve (NLSV) enables detection of spin signals at a location away from where the spin current is injected such that spin current can

be isolated from electron current. As shown in Fig. 1.3, two ferromagnetic layers are spatially separated but connected by non-magnetic material, in this case, a normal metal serving as transport channel. This spatial separation introduces a novel dimension to spintronic functionality, offering enhanced precision in manipulating spin states, such as applications in information processing, spin-based logic devices, and quantum computing. It also provides flexibility to explore efficient spin injection such as minimizing interfacial scattering in diffusive and ballistic contacts, as well as by optimizing the junction area. Most importantly, its ability to decouple spin injection and detection sites allows the downscaling of spintronic devices. In particular, NLSV is of great interest as a sub-10nm read head for magnetic recording due to its potential to reduce the shield to shield spacing and improve read head resolution.

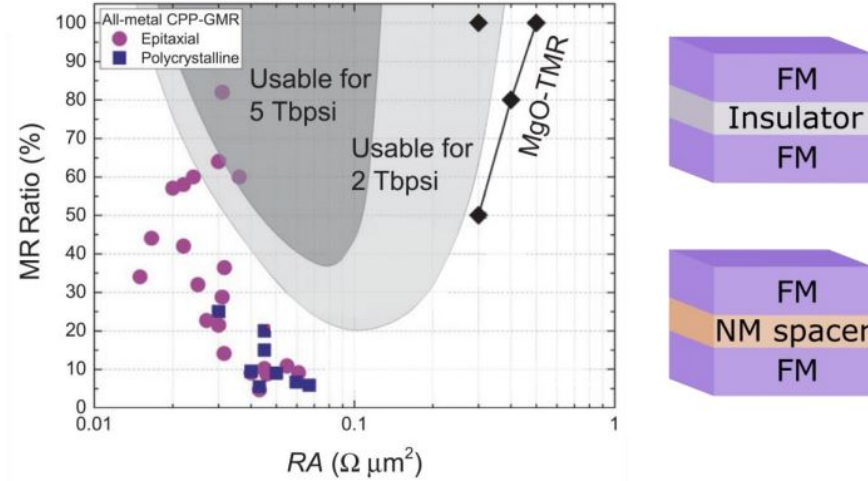


Figure 1.4: The dependence of MR ratio on RA product of metallic and tunneling spin valves hints the potential of metallic spin valves to meet the high areal density requirements of HDDs.

Furthermore, the low resistance-area (RA) product for normal metals posits all-metallic non-local spin valve as a superior candidate for integration into next-generation magnetic read heads compared to conventional MTJ-based sensors that utilize an insulating layer as spacer. The high RA product inherent to insulating materials can unfavorably impact electronics, presenting a challenge to downsize MTJs for read head



sensors. Illustrated in Fig. 1.4, achieving the target areal density of 2 Tbsi or higher with an  $RA < 0.1 \Omega \mu m^2$  suggests the exclusive feasibility of all metallic-based devices, whereas MTJs achieve a similar MR ratio ( $\sim 50\%$ ) with an RA of approximately  $0.3 \Omega \mu m^2$ , more than 10 times larger than metallic-based read heads [17, 18]. However, achieving high performance for commercialization of GMR-based read head requires further gain in Magnetoresistance (MR) ratio with reduced RA product. This hinges on a substantially long spin diffusion length within the Non-Magnetic (NM) channel and efficient spin injection to ensure accurate spin detection. Therefore, it is imperative to understand the spin relaxation mechanism in typical light metals with low spin orbit coupling.

## 1.2 Elliott-Yafet theory

The experimental and theoretical studies on spin relaxation has roots dating back to the 1950s, with a primary focus on semiconducting elements in the III-V group [19, 20, 21, 22, 23]. Partially driven by advances in experimental techniques such as spin resonance, ultrafast spectroscopy and the application of spintronics devices, increased efforts have been directed towards light metals and 2D materials. Experimentally, spin relaxaion can be studied through ultrafast magneto-optical pumping and spin transport measurements [24, 25, 26, 27], from which the direct observations of dynamical processes and determination of spin relaxation time,  $\tau_s$  can be achieved. Accurate prediction of spin lifetime and dominant relaxation mechanisms will enable the design of spin transport systems using suitable materials tailored for the intended purpose, while mitigating potential sources of degradation to enhance transport quality.

Developed independently by John H. Elliott and Y. Yafet in the 1950s [22, 23], Elliott-Yafet theory provides a theoretical framework for understanding the spin relaxation mechanisms in a wide range of materials, particularly in light metals. Formulating spin relaxation process mediated by spin-orbit coupling through ordinary scattering events involving phonons, impurities and defects, Elliott-Yafet theory has become indispensable to understanding spin dynamics for manipulating and controlling spin transports in the fields such as quantum computing, and other emerging technologies. Spin orbit coupling (SOC) is a relativistic interaction between electron spin and effective

magnetic field generated by nucleus motion around it (from the perspective of electron), which is given as

$$H_{soc} = \frac{1}{2m^2c^2} \left( r^{-1} \frac{\partial V}{\partial r} \right) = \epsilon_{SOC} \vec{L} \cdot \vec{S}$$

where  $\vec{r}$  is position of electron with respected to the nucleus.  $V(\vec{r})$  is the central potential energy derivative of the electron at  $\vec{r}$ ,  $m$  is the mass of electron and  $c$  is the speed of light.  $\vec{L}$  and  $\vec{S}$  are orbital angular momentum and spin angular momentum, respectively.  $\lambda_{SOC}$  denotes spin-orbital coupling, which is band-structure dependent.

Elliott-Yafet theory of spin relaxation originally predicted a simple linear proportionality between the spin lifetime  $\tau_s$  and the momentum relaxation time  $\tau_e$ , i.e.,  $\tau_s = \beta\tau_e$ , where  $\beta$  is sometimes referred to as an Elliott-Yafet (EY) constant.  $\beta^{-1}$  can be interpreted as the spin-flip probability during a momentum relaxation event: on average, every spin-flip event occurs in every  $\beta$  momentum relaxation events. Elliott first deduced this relation in a metal by using a perturbative approach which was later generalized with temperature dependence for different relaxation mechanisms by Yafet. The original EY theory describes the system with Kramers's degeneracy, resulting from time-reversal and inversion symmetry [28, 29]. For a system preserving both inversion and time-reversal symmetry, every state characterized by quantum numbers  $(\vec{k}, \sigma)$  has a degenerate state  $(\vec{k}, -\sigma)$ . Because of the spin-orbital coupling, Bloch states with well-defined spin polarization are no longer eigenstates of the complete Hamiltonian of the system. A general spin state  $|\tilde{\uparrow}\rangle$  can be written as a superposition of two spin degenerate eigenstate  $|\uparrow\rangle$  and  $|\downarrow\rangle$ . As a result, a new pair of degenerate eigenstates are given as follows:

$$\psi_{\vec{k}, \tilde{\uparrow}, n} = u_{\vec{k}, \tilde{\uparrow}, n} e^{i\vec{k} \cdot \vec{r}} = (a_{k,n} |\uparrow\rangle + b_{k,n} |\downarrow\rangle) e^{i\vec{k} \cdot \vec{r}}$$

$$\psi_{\vec{k}, \tilde{\downarrow}, n} = u_{\vec{k}, \tilde{\downarrow}, n} e^{i\vec{k} \cdot \vec{r}} = (a_{-k,n}^* |\uparrow\rangle - b_{-k,n}^* |\downarrow\rangle) e^{i\vec{k} \cdot \vec{r}}.$$

Here,  $n$  is the band index and  $u_{k,\sigma,n}$  is the Bloch function where  $a_{k,n}$  and  $b_{k,n}$  are the coefficients that preserve the periodicity of the lattice.  $a_{k,n}$  is of order 1 (min:  $\sqrt{1/2}$ ) and  $b$  is small, normally  $|b_{k,n}| \ll 1$ . Now if a scattering event occurs through non-spin-flip sources, e.g. impurity or phonons, the momenta is assumed to change between  $|\vec{k}, \sigma\rangle$  and  $|\vec{k}', \sigma'\rangle$ . The scattering probability to preserve and flip a spin state is determined by

the matrix element  $\langle \psi_{k,\sigma,n} | \delta H | \psi_{k',\sigma,n} \rangle$  and  $\langle \psi_{k,\sigma,n} | \delta H | \psi_{k',\sigma',n} \rangle$ , respectively, based on the a first-order perturbation theory. Assuming the scattering potential  $V(\vec{r})$  varies slowly within the length scale of several unit cells, the matrix elements can be approximately as

$$\langle \psi_{k,\sigma,n} | \delta H | \psi_{k',\sigma(\sigma'),n} \rangle \approx V_{k,k'} \langle u_{k,\sigma,n} | u_{k',\sigma(\sigma'),n} \rangle$$

with  $V_{k,k'}$  as the Fourier transform in the momentum space. The spin conserving/flip transition elements are given as

$$W_{\vec{k}\vec{k}'}^{(n)\sigma\sigma} = \frac{2\pi}{\hbar} \delta(E_k - E_{k'}) |V_{\vec{k},\vec{k}'}|^2 |\langle u_{k,\sigma,n} | u_{k',\sigma,n} \rangle|^2$$

and

$$W_{\vec{k}\vec{k}'}^{(n)\sigma\sigma'} = \frac{2\pi}{\hbar} \delta(E_k - E_{k'}) |V_{\vec{k},\vec{k}'}|^2 |\langle u_{k,\sigma,n} | u_{k',\sigma',n} \rangle|^2,$$

within approximation of Fermi's golden rule. Note that  $W_{\vec{k}\vec{k}'}^{(n)\sigma\sigma'}$  can be related to the change rate of number of spin-conserving and spin-flip electrons, which leads to the spin relaxation rate. Based on Elliott theory, the spin relaxation rate,  $\tau_s$  can be approximated with the spin flip rate,  $\Gamma_{sf}$ .

$$\Gamma_{sf} = \int d^3k d^3k' \frac{\delta(\vec{k} - \vec{k}_F)}{4\pi k_F^2} \frac{\delta(\vec{k}' - \vec{k}_F)}{4\pi k_F^2} 2W_{\vec{k}\vec{k}'}^n$$

The momentum-relaxation rate is given as

$$\Gamma = \int d^3k d^3k' \frac{\delta(\vec{k} - \vec{k}_F)}{4\pi k_F^2} \frac{\delta(\vec{k}' - \vec{k}_F)}{4\pi k_F^2} (W_{\vec{k}\vec{k}'}^n + W_{\vec{k}\vec{k}'}^n)$$

The linear proportionality between  $\Gamma$  and  $\Gamma_{sf}$  can be understood as follows. Note that the spin-conserving and spin-flip probability  $P_{\vec{k}\vec{k}'}^{\sigma\sigma} \propto \sum_n |W_{\vec{k}\vec{k}'}^{(n)\sigma\sigma}|^2$ , given as below.

$$\begin{aligned} P_{\vec{k}\vec{k}'}^{\uparrow\uparrow} &= |\langle \psi_{\vec{k}\uparrow} | \delta H | \psi_{\vec{k}'\uparrow} \rangle|^2 \\ &= |\langle a_{\vec{k}} e^{i\vec{k}\vec{r}} | \delta H | a_{\vec{k}'} e^{i\vec{k}'\vec{r}} \rangle + \langle b_{\vec{k}} e^{i\vec{k}\vec{r}} | \delta H | b_{\vec{k}'} e^{i\vec{k}'\vec{r}} \rangle|^2 \end{aligned}$$

$$\begin{aligned} P_{\vec{k}\vec{k}'}^{\uparrow\downarrow} &= |\langle \psi_{\vec{k}\uparrow} | \delta H | \psi_{\vec{k}'\downarrow} \rangle|^2 \\ &= | - \langle a_{\vec{k}} e^{i\vec{k}\vec{r}} | \delta H | b_{-\vec{k}'}^* e^{i\vec{k}'\vec{r}} \rangle + \langle b_{\vec{k}} e^{i\vec{k}\vec{r}} | \delta H | a_{-\vec{k}'}^* e^{i\vec{k}'\vec{r}} \rangle |^2 \end{aligned}$$

Estimated by perturbation theory, the resulting Bloch state can be expressed as

$$\psi_{k,\uparrow} = |\chi_{n,\vec{k}}\rangle |\uparrow\rangle + \sum_{n' \neq n} \left[ \frac{\langle \uparrow | \langle \chi_{n'\vec{k}} | \epsilon \vec{L} \cdot \vec{S} | \chi_{n,\vec{k}} \rangle | \uparrow \rangle}{E_{n\vec{k}} - E_{n'\vec{k}}} |\chi_{n'\vec{k}}\rangle |\uparrow\rangle + \frac{\langle \downarrow | \langle \chi_{n'\vec{k}} | \epsilon \vec{L} \cdot \vec{S} | \chi_{n,\vec{k}} \rangle | \uparrow \rangle}{E_{n\vec{k}} - E_{n'\vec{k}}} |\chi_{n'\vec{k}}\rangle |\downarrow\rangle \right],$$

where  $|\chi_{n,\vec{k}}\rangle$  is generic eigenstate and coefficient  $a_{k,n}$  and  $b_{k,n}$  can be determined by comparing with the unperturbed state. Define  $\Delta = \min |E_{n\vec{k}} - E_{n'\vec{k}}|$  as the minimum energy difference between two adjacent bands. Because the SOC constant is small, the coefficient associated with spin flip probability is much smaller than the coefficient associated with spin-conserving probability. Hence, summing over all the possible  $k$  states over the Fermi surface yields:

$$\frac{\tau_e}{\tau_s} = \frac{\Gamma_{sf}}{\Gamma} \approx \frac{P^{\uparrow\downarrow}}{P^{\uparrow\uparrow}} \approx \langle b^2 \rangle \approx \left( \frac{\langle \epsilon \rangle}{\Delta} \right)^2 = \beta^{-1}$$

where  $\langle b^2 \rangle$  denote the average of  $b_k$  over the entire Fermi surface. This derivation indicates that when extrinsic sources break momentum conservation, coupled with SOI, a spin-flip transition between the two degenerate spin states can occur through spin-independent scattering sources modulated by SOC, such as impurities and phonons.

In a realistic system, spin relaxation is generally induced by multiple scattering sources. The original EY formulation can be cast to a spin-relaxation form of Matthiessen's rule [53] to accommodate multiple sources of scattering. The total spin relaxation rate  $1/\tau_s$  is the sum of each individual spin scattering rate  $1/\tau_{s,i}$ , each of which follows the EY prediction with  $\beta_i$  as the proportionality associated to each scattering source, i.e.

$$1/\tau_s = \sum_i \beta_i^{-1} / \tau_{e,i}.$$

Such a formulation enables more direct comparison between experimental and theoretical works. Although precise isolation of each scattering sources could be challenging, this formulation is instrumental in selecting the dominant contributions in each category of scattering sources and benefits subsequent comparison with theoretical works. For example, separating the temperature-dependent sources such as phonon and magnetic impurities, from temperature-independent ones, such as point defects, dislocations, grain boundaries, and surface roughness, at low temperature can be used to extract  $\beta$

associated with structural defects. Specifically, via conduction electron spin resonance (CESR) measurements, the temperature-independent  $\beta$  from simple non-magnetic metals such as Au, Cu, Ag, Na, and K is determined [30, 31, 42]. However, efforts to specifically isolate defect-induced spin relaxation mechanisms are generally limited in scope and technique resolution.

Note that the Elliott-Yafet assumptions of a spherical Fermi surface for monovalent metals in a system with inversion symmetry is rarely satisfied simultaneously. Surprisingly, the Elliott-Yafet framework remains effective in describing the SOI induced spin relaxation mechanism for light metals and semi-conductors. As a result, interesting spin-relaxation phenomena have been discovered within Elliott-Yafet picture. By accurately determining  $\beta_i$  for the contribution of each individual scattering source in Cu, a wide range of  $\beta$  have been found for different scattering sources. The variation in  $\beta$  is attributed to magnetic impurity contamination even with sub- $10^{-4}\%$  dilute concentration. It has been found that magnetic impurity enhances substantially both defect-induced and phonon-induced spin relaxation in Cu, yielding large variation in  $\beta$  (Spin Kondo Effect) [32]. In Al, a wide range of reported  $\beta$  implicates the finite-size effect of surfaces and interfaces on phonon-induced spin relaxation, addressing the challenges to downsizing the spintronics device once again [33].

### 1.2.1 Challenges for Al

Among metals, aluminum is an outstanding candidate for spintronic devices due to its low resistance, inherently long spin relaxation time, low cost and manufacturability. However, the study of spin relaxation induced by defects in Al is not as intensive as that in other light metals and 2D materials. It may be attributed to growth problems and existence of spin hot spots in Al.

Al possesses a challenging growth problem characterized by ‘Hillocks’, which refers to the small, elevated mounds or bumps on the surface of a thin metallic film or layer, aggravating the surface roughness effect. The accumulation of hillocks may eventually facilitate grain boundary sliding, create mechanical instability and alter the surface topography, leading to formation of surface and bulk defects and compromising the performance of devices [34, 35, 36].

The formation of hillocks results from compressive and thermal expansion stress relaxation during deposition process. When Al is deposited on a substrate (Si or SiO<sub>2</sub>), heating procedures induce stress arising from the mismatch of thermal expansion coefficients between the Al film and the substrate and incorporation of deposition by-products. In addition, the diffusion of Al grains along with crystalline structures may further induce the stress locally, leading to inhomogeneity in the Al grain structure and formation of hillocks. Consequently, a large grain size distribution and stress-induced vacancy concentration can be expected even at low temperature [37, 38, 39]. The possible strategies to mitigate hillock formation include optimizing deposition temperature, introducing barrier layers, and implementing post-deposition annealing processes to relieve stress in the aluminum film. Yet, the realization of hillock-mitigation strategies remains challenging.

### 1.2.2 Spin hot spots

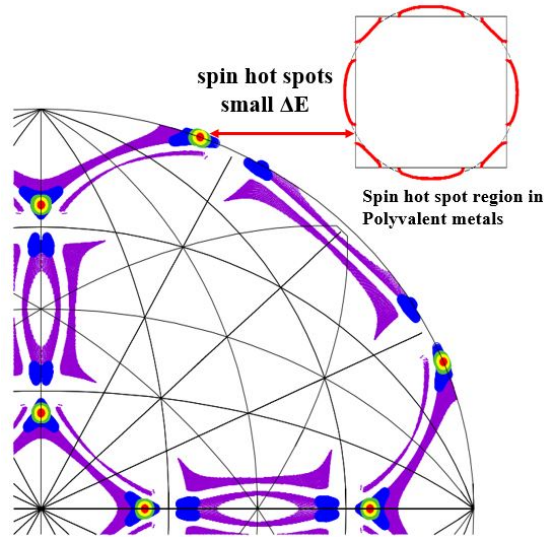


Figure 1.5: The schematic illustration of the locations for spin “hot spots” on Fermi surface of polyvalent metal. Color violet, blue green, yellow and red represent the increase in intensity of spin relaxation. Adapted from Ref. [40].

Experimental and theoretical researchers have found that Al, along with other polyvalent metals. e.g., Pd, Mg and Be, show unanticipated stronger spin relaxation than other simple metals (Cu, Ag, Au, Na, K, Rb and Cs), approximately by 2 - 3 order of magnitudes [30, 42]. The discrepancy is ascribed to an enhancement in the strength of the spin-orbit interaction from selected "outliers" in specific regions of the Fermi surface. These outliers, referred to as "spin hotspots", emerge near Brillouin zone boundaries, special symmetry points, or lines of accidental degeneracy where the associated energy difference ( $dE$ ) approaches zero [40, 41]. Despite occupying a tiny portion of the Fermi surface, the presence of these spin hotspots leads to a notable enhancement in overall spin relaxation rate even after averaging with normal  $k$  states as depicted in Fig. 1.5.

Although the presence of spin hotspots addresses the intricacies of the polyvalent-Al Fermi surface, which can explain spin relaxation strengths up to two orders of magnitude stronger than those predicted in mono-valent metals, depending on the scattering process, studies above pertain to phonon-induced spin relaxation of bulk Al. Experimental measurements suggest perturbed band structures near the surface of Al can give rise to weak surface spin relaxation [43]. In general, the effect of spin hotspots on thin polyvalent metallic films at low temperature, particularly those with sub-10nm thickness, remains unresolved [52]. These puzzles underscore the complexities in predicting  $\beta$ , even within the context of light metals and demand reliable calculations of band structure and transport properties, capable of quantifying beta for each single scattering sources.

### 1.2.3 Size effect on metallic NLSV

Downsizing spintronic devices is pivotal to next-generation technology, involving the miniaturization of components for superior performance, efficiency and higher integration density. By reducing device dimensions, spintronic components can operate at faster speeds, consume less power, and offer greater design and structure versatility especially in computing and data storage systems, which relies on spin dynamics that can preserve spin information at longer period of time and distance. Non-local spin valves (NLSV) are of great interest for their separation of pure spin currents from charge currents, which allows studying both spin injection and spin relaxation. In practice, it may also serve as read heads for magnetic recording [44, 45, 46] by utilizing its GMR-induced

binary output [3, 4].

Many have been motivated to improve the head resolution and writing density by reducing the thickness of nonmagnetic materials used as transport channels, e.g. 2D materials [47, 48, 49] and light metals [50, 51]. Nevertheless, the size effect on metallic NLSV presents challenges to reducing the thicknesses of metallic transport channel, primarily due to poorly understood spin relaxation mechanisms, even in metals with low spin-orbit interaction (SOI). In particular, for sub-10nm spin transport channel, the metallic spin valve performance deteriorates substantially [52].

Many sources inducing spin relaxation have been intensively discussed in the literature. It has been suggested that extrinsic effects acting through SOI such as charged impurities and surface roughness, grain boundary (GB) scattering and phonon scattering can be responsible for the fast spin relaxation rates in metals. Furthermore, it is expected that temperature-independent contributions, including surface and grain boundary, dominate the spin relaxation in the low temperature regime. This is because as the cross-sectional area of the transport channel decreases, the surface-to-volume ratio increases, enhancing electron interaction with the channel's surfaces leading to more frequent backscattering. Meanwhile the reduced cross-sectional dimensions lead to a decrease in grain size, forcing electrons to traverse a greater number of grains, thereby stronger spin relaxation.

It has been proposed that when the mean free path is comparable to the film dimension, surface scattering should dominate over spin relaxation [50]. However, studies addressing size effects on spin relaxation mechanism in metals suggested that GB scattering dominates spin relaxation [55, 51, 54]. So far no consensus has been reached because GB scattering and surface scattering are generally coupled and both surface roughness and GB are strongly dependent on the growth and deposition conditions, which varies among experimental groups. Therefore, the dominant contribution at low temperature to spin relaxation remains puzzling.

In addition, the limitations in Fuchs [56] and Sondheimer (FS) model [57] and the Mayadas and Shatzkes (MS) [59] model, which is used to quantitatively characterize momentum relaxations induced by surface roughness and GB scatterings, impose challenges in distinguishing GB scattering from surface roughness quantitatively. Phenomenological parameters, such as surface specularity and the grain boundary reflection coefficient,



which are fitted as free parameters or usually assigned to indicate the extreme cases, generally cannot be directly related to measured surface parameters or grain boundary structures. Consequently, accurately separating surface and GB scattering based on FS and MS model remains challenging, highlighting the necessity of theoretical work that treat them independently.

### 1.3 Outline

The dissertation is structured into two parts, focusing on optimizing HAMR-device performance and achieving higher areal through novel NLSV-based read heads and composite media structures.

The first part, consisting of Chapters 1-3, is dedicated to identifying the dominant contributions to electron and spin relaxation in ultra-thin Al films for NLSV-based read heads at  $T = 0$  K.

- Chapter 2 derives the transmission function in terms of Green's function in a simplified NLSV-transport system using the Landauer-Buttiker formalism and introduces the recursive Green's function to describe spin transport in the Al-system, which can be used to extract relevant quantities such as resistivity, spin diffusion length, and the EY constant  $\beta$ .
- Chapter 3 presents detailed simulation methods and discusses the results on the quantitative contributions to momentum and spin relaxation from various structural defects, including surface roughness, grain boundaries, vacancies, and surface reconstruction.

## Chapter 2

# Modeling Methods for Electron and Spin Transport

### 2.1 Landauer-Büttiker formalism and Transmission Function

#### Green's function

The Green's function method is known as a powerful mathematical tool for solving linear partial differential equations that describe the evolution of systems of interest, thus offering a systematic approach to understand and predict the dynamics across various physical phenomena. In the quantum context, the Green's function can be interpreted as an impulse response function or correlation function from which information regarding quantum system's characteristics can be extracted, such as density of states, relaxation time and response function. The Schrödinger equation, as a linear partial differential equation can be solved by Green's function, particularly for the systems with complex potentials and time dependence. By treating the potential terms as a superposition of weighted point sources, the wave-function solution can be found by convoluting the Green's function and the potential terms. Written in operator form, the Green's function,  $G(E)$ , is given as follows.

$$(E \pm i\delta - H)G(E) = I, \quad (2.1)$$

where  $H$  denotes the Hamiltonian of the system and  $E$  represents the energy matrix. To avoid the singularity, an infinitesimal imaginary part  $i\delta$  is introduced in the expression. The plus and minus sign in the front of the imaginary part corresponds to the retarded solution and the advanced solution, respectively.

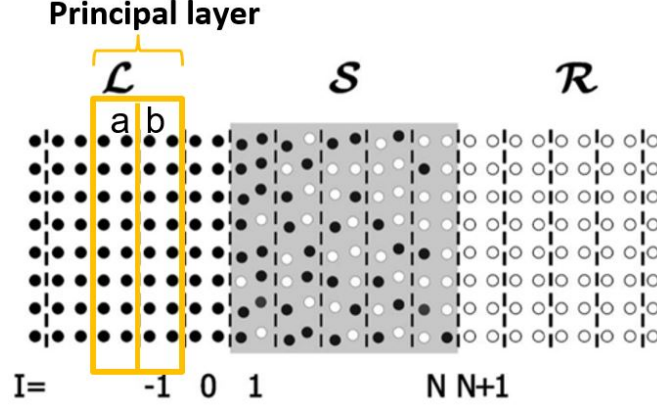


Figure 2.1: A schematic diagram for the system sliced layer by layer, where L, R and S stand for the left lead, the right lead and the scattering region in the Landauer-Büttiker formalism. A principal layer consisting of two atomic layers is included in the Hamiltonian of the system with second nearest neighbor interaction.

For a two-lead transport device, the one-particle Hamiltonian can be written in a matrix form as

$$H = H_0 + V = \begin{bmatrix} H_L & 0 & 0 \\ 0 & H_d & 0 \\ 0 & 0 & H_R \end{bmatrix} + \begin{bmatrix} 0 & V_{Ld} & 0 \\ V_{dL} & 0 & V_{dR} \\ 0 & V_{Rd} & 0 \end{bmatrix}, \quad (2.2)$$

where the  $H_{L,R}, H_d$  are the Hamiltonians describing the left/right isolated leads and central device region, respectively.  $V$  is the coupling between the leads and the device regions. The retarded Green's function can be defined for the system using eigenstates of the Hamiltonian in the form of  $H|\Psi_m(E)\rangle = E|\Psi_m(E)\rangle$ , where  $m$  is the label of different quantum states. The Green's function can also be written in the following form.

$$G(E) = [E - i\delta - H]^{-1} = \int dE' \sum_m \frac{|\Psi_m(E')\rangle \langle \Psi_m(E')|}{E - i\delta - E'} \quad (2.3)$$

By definition, the Green's function in the scattering can be computed from

$$\begin{bmatrix} E - H_L & -V_{Ld} & 0 \\ -V_{dL} & E - H_d & -V_{dR} \\ 0 & -V_{Rd} & E - H_R \end{bmatrix} \begin{bmatrix} G_L & G_{Ld} & G_{LR} \\ G_{dL} & G_d & G_{dR} \\ G_{RL} & G_{Rd} & G_R \end{bmatrix} = \begin{bmatrix} 1 & 0 & 0 \\ 0 & 1 & 0 \\ 0 & 0 & 1 \end{bmatrix} \quad (2.4)$$

Solving the equation above yields,

$$G_{Ld} = g_L V_{Ld} G_d \quad (2.5)$$

$$G_{Rd} = g_R V_{Rd} G_d \quad (2.6)$$

where  $g_{L,R} = [E - H_{L,R}]^{-1}$  are the Green's function of the isolated leads. Substituting Eq. 2.5 and Eq. 2.6 into Eq. 2.4, the Green's function of the central device is given as

$$G_d = [E - H_d - \Sigma_L - \Sigma_R]^{-1}, \quad (2.7)$$

where

$$\Sigma_L = V_{dL} g_L V_{Ld}, \quad (2.8)$$

$$\Sigma_R = V_{dR} g_R V_{Rd}, \quad (2.9)$$

is the self-energy of left and right lead, respectively. The level-width matrices relevant to the self-energy function, are defined as

$$\Gamma_L = i(\Sigma_L - \Sigma_L^\dagger) \quad (2.10)$$

$$\Gamma_R = i(\Sigma_R - \Sigma_R^\dagger), \quad (2.11)$$

where ' $\dagger$ ' denotes the complex conjugate operation.

### 2.1.1 Landauer-Büttiker formalism

The Landauer-Büttiker (LB) formalism, a cornerstone in mesoscopic physics, provides a powerful framework for understanding electron transport in nanoscale systems. Formulated in the late 20th century by R. Landauer and extended by M. Büttiker to multi-terminal systems, this formalism offers a quantum-mechanical description of electron conducting through mesoscopic conductors such as quantum dots, quantum wires and molecular junctions, by connecting the electron's transmission function and conductance of quantum system. LB formalism assumes coherent electron transport, i.e,

elastic scattering, in a quantum junction with semi-infinite leads attached to the scattering region, ensuring the equilibrium states of the system and reflection-free entry to the scattering region [60, 61, 62]. The goal of this section is to determine the conducting properties of the LB-based quantum system with transmission probability described by the Green's function of electrons.

For the two-lead system, there exist two sets of scattering states, each set originating from one of the reservoirs connected to the leads. The scattering states originating from one lead can be computed by considering the isolated eigenstates of the semi-infinite lead and treating the interaction between the leads as a perturbation. If  $|U^{(L)}\rangle$  is an orthogonal eigenstate of the isolated left leads, the resulting state  $|\Psi^{(L)}\rangle$  from  $|U^{(L)}\rangle$  propagating into the device region can be written as

$$|\Psi^{(L)}\rangle = GV|U^{(L)}\rangle + |U^{(L)}\rangle, \quad (2.12)$$

where the superscript indicates that this state originates from the left lead. In the spatial partitioning, the states  $|\Psi^{(L)}\rangle$  and  $|U^{(L)}\rangle$  are given as

$$|U^{(L)}\rangle = \begin{bmatrix} |u^{(L)}\rangle \\ 0 \\ 0 \end{bmatrix}, \quad |\Psi^{(L)}\rangle = \begin{bmatrix} |\psi_L^{(L)}\rangle \\ |\psi_d^{(L)}\rangle \\ |\psi_R^{(L)}\rangle \end{bmatrix} \quad (2.13)$$

Define projection operators  $P$  such that  $P_L + P_R + P_d = I$ , where  $P_L, P_d$  and  $P_R$  are the projection operator for left lead, device region and right lead respectively.

$$P_L = \begin{bmatrix} 1 & 0 & 0 \\ 0 & 0 & 0 \\ 0 & 0 & 0 \end{bmatrix}, \quad P_d = \begin{bmatrix} 0 & 0 & 0 \\ 0 & 1 & 0 \\ 0 & 0 & 0 \end{bmatrix}, \quad P_R = \begin{bmatrix} 0 & 0 & 0 \\ 0 & 0 & 0 \\ 0 & 0 & 1 \end{bmatrix} \quad (2.14)$$

The number of electrons in lead R is described by the projection operator  $P_R$ . The operator for current into the right leads can therefore be determined as the time derivative of this operator which results in

$$J_R = \frac{i2e}{\hbar} [H, P_R]. \quad (2.15)$$

The contribution to the current between the left and the right lead from the state  $|\Psi^{(L)}\rangle$

can be computed from

$$\begin{aligned}
j^{(L)} &= \langle \Psi^{(L)} | J_R | \Psi^{(L)} \rangle \\
&= \frac{i2e}{\hbar} [\langle \psi_d^{(L)} | V_{dR} | \psi_R^{(L)} \rangle - \langle \psi_R^{(L)} | V_{Rd} | \psi_d^{(L)} \rangle] \\
&= \frac{i2e}{\hbar} [\langle \psi_d^{(L)} | V_{dR} g_R V_{Rd} | \psi_d^{(L)} \rangle - \langle \psi_d^{(L)} | V_{dR} g_R^\dagger V_{Rd} | \psi_d^{(L)} \rangle] \\
&= \frac{2e}{\hbar} \langle \psi_d^{(L)} | \Gamma_R | \psi_d^{(L)} \rangle,
\end{aligned} \tag{2.16}$$

where the commutation relation in Eq. 2.15 is expanded using the operator block structure of  $G$  and  $V$ , based on Eq. 2.4, Eq. 2.12 and Eq. 2.13. The total current arising from all states originating in the left lead is the sum over all scattering states  $|\psi_{d,l}^{(L)}\rangle$ , indexed by  $l$ ,

$$\begin{aligned}
I^{(L)} = j_{tot}^{(L)} &= \frac{2e}{\hbar} \sum_l \langle \psi_{d,l}^{(L)} | \Gamma_R | \psi_{d,l}^{(L)} \rangle f(E_L) \\
&= \frac{2e}{\hbar} \sum_l \langle u_l^{(L)} | V_{Ld} G_d^\dagger | \Gamma_R | G_d V_{dL} | u_l^{(L)} \rangle f(E_L) \\
&= \frac{2e}{\hbar} \sum_l \langle u_l^{(L)} | \Gamma_R G_d V_{dL} a_L V_{Ld} G_d^\dagger | u_l^{(L)} \rangle f(E_L) \\
&= \frac{2e}{\hbar} \text{Tr}[\Gamma_R G_d \Gamma_L G_d^\dagger] f(E_L),
\end{aligned} \tag{2.17}$$

where  $a_L = i(g_L - g_L^\dagger) = 2\pi \sum_l |u_l^{(L)}\rangle \langle u_l^{(L)}|$  by the definition of the spectral function and  $f(E_L)$  describes the charge populations of the left states at the energy of  $E_L$ . Note that Eq. 2.17 is derived based on Eq. 2.4, Eq. 2.8, Eq. 2.10, Eq. 2.12 and Eq. 2.13.

### Transmission function

Consider a finite scattering region attached to two semi-infinite leads in the Landauer-Büttiker formalism. The expectation value of total current induced by a general potential is

$$\langle I \rangle = \frac{2e}{h} \int dE T(E) [f_L(E) - f_R(E)], \tag{2.18}$$

where  $f_L(E)$  and  $f_R(E)$  are Fermi-Dirac distribution functions. Consider a bias voltage  $V$  is applied to the system where a linear approximation suffices, the chemical potential reads  $\mu_L = \mu + \frac{eV}{2}$  and  $\mu_R = \mu - \frac{eV}{2}$ , with  $\mu$  as the equilibrium value. In the limit

of a small bias and at low temperature, the difference in the Fermi-Dirac distribution function is reduced to a delta function.

$$f_L(E) - f_R(E) = f(E - E_f - \frac{eV}{2}) - f(E - E_F + \frac{eV}{2}) = \delta(E - E_F)eV. \quad (2.19)$$

Compared with Eq. 2.17 and Eq. 2.18,  $T(E)$  is given in terms of the Green's function is as follows.

$$T(E) = Tr[\Gamma_R G_d \Gamma_L G_d^\dagger] = Tr[\Gamma_L G_d \Gamma_R G_d^\dagger] \quad (2.20)$$

The elastic scattering assumption justifies Eq. 2.20, because the transmission from the left lead to the right is the same as the transmission from the right lead to the left.

Substituting Eq. 2.19 into Eq. 2.18, the conductance of the system becomes

$$G = I/V = \frac{2e^2}{h} T(E_F) = \frac{2e^2}{h} Tr[\Gamma_R G_d \Gamma_L G_d^\dagger], \quad (2.21)$$

where the factor 2 comes from the spin degeneracy. This equation is called the *Caroli* formula [66].

### 2.1.2 Recursive Green's Function Method

Recall that the inhomogeneous part of the Schrodinger equation also depends on the wavefunction itself. Such self-consistent equations would normally need recursive procedures to find the Green's function. Consider a system A consisting of N layers with M atoms in one atomic layer, this  $MN \times MN$  matrix requires the steps of  $O(M^3 N^3)$  to obtain its Green's function.

Fortunately, Dyson's equation provides a way to systematically incorporate interaction between two sub-systems into the Green's function of the entire physical systems by treating the sub-systems one by one, or in the case of LB systems, layer by layer. Mathematically, Dyson's equation can be written as

$$G = G_0 + G_0 V G, \quad (2.22)$$

where  $G_0$  is the non-perturbed or isolated Green's function,  $G$  denotes the Green's function with full interaction  $V$  between any subsystems. For example, for the same system A, to couple the Green's function of zeroth layer  $g_0$  to that of first layer  $g_1$  with

interaction  $V$ ,  $G_0$  is defined as  $|0\rangle g_1 \langle 0| + |1\rangle g_0 \langle 1|$  and  $V$  is  $|0\rangle t_{0,1} \langle 1| + |1\rangle t_{1,0} \langle 0|$ , where  $|0\rangle$  and  $|1\rangle$  are two orthonormal states for layer 0 and layer 1. Let  $\langle n|G|m\rangle$  be  $G_{n,m}$ , where  $n$  and  $m$  are orthonormal states for the  $n$ th and  $m$ th layer, respectively. Based on Dyson's equation,

$$G_{1,1} = g_1 + g_1 t_{1,0} G_{0,1} \quad (2.23)$$

$$G_{0,1} = g_0 t_{0,1} G_{1,1} \quad (2.24)$$

Therefore,

$$G_{1,1} = (I - g_1 t_{1,0} g_0 t_{0,1})^{-1} g_1 = (E - h_1 - t_{1,0} g_0 t_{0,1})^{-1} \quad (2.25)$$

where  $g_1 = (E - h_1)^{-1}$  by definition and  $h_1$  is the Hamiltonian of the first layer. As shown above, the matrix inversion operation is exclusively applied to the diagonal element of the Green's function and off-diagonal terms can be obtained by matrix multiplication. Thus, it takes only  $N$  inversions of  $M \times M$  matrix, which will require approximately steps of  $O(N \times M^3)$ . In the transport calculations,  $N$  is typically larger than 100. Thus, the recursive method is four orders of magnitude faster than direct inversion.

Similarly, Dyson's equation can apply to the interface Green's function of semi-infinite leads. Let  $L$  and  $R$  denote the left and right lead, respectively. In this case, Dyson's equation is used to obtain recursive relations for the exact Green's function of a quasi-one dimensional system coupled to leads as an example. The basic idea is to break up the system into independent parts and associate these parts to isolated Green's functions, as in Fig. 2.1. The hopping matrix elements connecting those parts are built into the perturbation. By recursively applying Dyson's equation, the full Green's function of the entire system can be constructed layer by layer.

The rightmost layer of the left lead is denoted as the zeroth slice and the leftmost layer of the right lead is denoted as the  $N + 1^{th}$  slice. The goal is to obtain the Green's function,  $G_{0,N+1}$ .

Similar to the example of coupling two layers, the Green's function can be evaluated recursively for  $n = 2, \dots, N$ . Then  $G_{0,N+1}^r$  can be found by

$$G_{0,N+1}^r = G_{0,N}^r t_{N,N+1} G_{N+1,N+1}^r, \quad (2.26)$$

where

$$G_{N+1,N+1}^r = (g_R^{-1} - t_{N+1,N} G_{N,N}^r t_{N,N+1})^{-1} \quad (2.27)$$



The recursive method shown above is based on the known interface Green's function of both leads, i.e.  $g_L$  and  $g_R$ , which can be numerically evaluated following Sancho Lopez's paper [63]. The method works as follows. For translational-invariant semi-infinite leads, by definition, the Green's function obeys  $[(E - H)G(E)]_{n,m} = \delta_{n,m}$ , where  $H$  is defined over a chain of principal layers. Assume that all these connections are represented by operators  $t$  (hopping from left to right) and  $t^\dagger$  (hopping from right to left). The isolated Hamiltonian is denoted by  $h$ . Then one can write that

$$(E - h)G_{0,0} = I + tG_{1,0}, \quad (2.28)$$

$$(E - h)G_{1,0} = tG_{2,0} + t^\dagger G_{0,0}, \quad (2.29)$$

$$\vdots$$

$$(E - h)G_{n,0} = tG_{n+1,0} + t^\dagger G_{n-1,0} \quad (2.30)$$

for  $n \geq 1$ . With Eq. 2.28,  $G_{1,0}$  is substituted with  $G_{0,0}$  and  $G_{2,0}$  is given as

$$[E - h - t(E - h)^{-1}t^\dagger]G_{0,0} = I + t(E - h)^{-1}tG_{2,0} \quad (2.31)$$

Similarly,  $G_{n,0}$  can be related to  $G_{n-2,0}$  and  $G_{n+2,0}$  by eliminating  $G_{n-1,0}$  and  $G_{n+1,0}$ . For any value of  $n$ , one can find that

$$G_{n+1,0} = (E - h)^{-1}(tG_{n+2,0} + t^\dagger G_{n,0}) \quad (2.32)$$

and

$$G_{n-1,0} = (E - h)^{-1}(t^\dagger G_{n-2,0} + tG_{n,0}). \quad (2.33)$$

Combining these two equations, one find that

$$\begin{aligned} [E - h - t(E - h)^{-1}t^\dagger - t^\dagger(E - h)^{-1}t]G_{n,0} = \\ t(E - h)^{-1}tG_{n+2,0} + t^\dagger(E - h)^{-1}t^\dagger G_{n-2,0}. \end{aligned} \quad (2.34)$$

Comparing these equations above with Eq. 2.32, a new recursive series only involving even layers can be constructed, where one can write

$$(E - \epsilon_1^s)G_{0,0} = I + \alpha_1 G_{2,0} \quad (2.35)$$

$$(E - \epsilon_1)G_{2,0} = \alpha_1 G_{4,0} + \beta_1 G_{0,0} \quad (2.36)$$

$$\vdots$$

$$(E - \epsilon_1)G_{n,0} = \alpha_1 G_{n+2,0} + \beta_1 G_{n-2,0}. \quad (2.37)$$

Here

$$\alpha_1 = t(E - h)^{-1}t \quad (2.38)$$

$$\beta_1 = t^\dagger(E - h)^{-1}t^\dagger \quad (2.39)$$

$$\epsilon_1^s = h + t(E - h)^{-1}t^\dagger \quad (2.40)$$

and

$$\epsilon_1 = \epsilon_1^s + t^\dagger(E - h)^{-1}t \quad (2.41)$$

Notice that Eq. 2.35 - 2.37 involve only even sites (i.e. multiples of  $2^1$ ) and they are in the identical form of Eq. 2.28 - 2.32. This procedure can be repeated by eliminating the Green's functions related to the nearest neighbor layers and involving only layers that are multiple of  $2^k$ . For the  $k^{th}$  iteration,

$$(E - \epsilon_k^s)G_{0,0} = I + \alpha_k G_{2^k,0} \quad (2.42)$$

$$(E - \epsilon_k)G_{2^k,0} = \alpha_k G_{2^{k+1},0} + \beta_k G_{0,0} \quad (2.43)$$

$$\vdots$$

$$(E - \epsilon_k)G_{2^k n,0} = \alpha_k G_{2^{k(n+1)},0} + \beta_k G_{2^{k(n-1)},0} \quad (2.44)$$

where for  $n \geq 1$ ,

$$\alpha_k = \alpha_{k-1}(E - \epsilon_{k-1})^{-1}\alpha_{k-1} \quad (2.45)$$

$$\beta_k = \beta_{k-1}(E - \epsilon_{k-1})^{-1}\beta_{k-1} \quad (2.46)$$

$$\epsilon_k^s = \epsilon_{k-1} + \alpha_{k-1}(E - \epsilon_{k-1})^{-1}\beta_{k-1} \quad (2.47)$$

and

$$\epsilon_k = \epsilon_k^s + \beta_{k-1}(E - \epsilon_{k-1})^{-1}\alpha_{k-1} \quad (2.48)$$

This decimation can stop when  $\|\alpha_k\|$  and  $\|\beta_k\|$  are sufficiently small, allowing us to approximate the surface Green's function by  $G_{0,0} \simeq (E - \epsilon_k^s)^{-1}$ .

### 2.1.3 Tight-Binding Model

It is convenient to study the disordered systems with a Green's function described by the tight-binding model [64]. The Hamiltonian of the system is described as  $H = H_{TB} + H_{SOC}$ , where  $H_{TB}$  is the Hamiltonian in the tight-binding structure with first and second nearest-neighbor hopping and  $H_{SOC}$  denotes the intrinsic spin-orbit interaction.  $H_{TB}$  is determined by the Slater-Koster (SK) parameters for s, p and d orbitals [65]. A principal layer consisting of two atomic layers is incorporated in the Hamiltonian to accommodate second-nearest-neighbor hopping given in the SK parameters. For a Al-system with  $N$  principal layers, the general structure of  $H_{TB}$  for a given spin state is in the block tridiagonal form as follows:

$$\begin{bmatrix} H_L & t_L & 0 & 0 & 0 & \cdots & 0 \\ t_L^\dagger & H_1 & t & 0 & 0 & \cdots & 0 \\ 0 & t^\dagger & H_2 & t & 0 & \vdots & 0 \\ \vdots & \vdots & \ddots & \ddots & \ddots & \cdots & \vdots \\ 0 & \cdots & & t^\dagger & H_i & t & \vdots \\ & & & 0 & t^\dagger & H_N & t_R \\ 0 & & \cdots & & t_R^\dagger & H_R \end{bmatrix} \quad (2.49)$$

In Eq. 2.49,  $H_L/H_R$  denotes the Hamiltonian of the left/right semi-infinite leads respectively;  $t_R$  and  $t_L$  represent the interaction between the leads and layers in the scattering regions. The on-site Hamiltonian for the  $i^{\text{th}}$  principal layer is denoted by  $H_i$  for  $1 \leq i \leq N$ .  $t$  is the hopping matrix between two adjacent principal layers which is identical for any two adjacent principal layers as the scattering potential only alters the on-site Hamiltonian  $H_i$  in the simulation. Each entry in Eq. 2.49 is a submatrix, whose dimension is determined by the number of orbitals for each Al atom and the number of atoms in one atomic layer.

Periodic boundary conditions are applied in one transverse direction with a wave vector  $k_y$  and the other two directions are treated in real space. For an Al system described by the Slater-Koster parameters with second-nearest neighbor hopping [65],  $H_i$  is a  $2N_{orb}M \times 2N_{orb}M$  matrix given as follows, where  $N_{orb} = 9$  is the number of orbitals for each Al atom and  $M$  is the number of atoms.

$$H_i = \begin{bmatrix} h_a^0(k_y) & h_{ab}^0(k_y) \\ h_{ab}^{0\dagger}(k_y) & h_b^0(k_y) \end{bmatrix}, \quad (2.50)$$

where  $h_a^0(k_y)$  and  $h_b^0(k_y)$  stand for the Hamiltonian in the first and second atomic layers respectively and  $h_{ab}^0(k_y)$  represents the interaction between the first and second atomic layer within the principal layer.

Similarly, the structure of a hopping matrix  $t$  can be written as below.

$$t = \begin{bmatrix} h_a^1(k_y) & 0 \\ h_{ab}^{1\dagger}(k_y) & h_b^1(k_y) \end{bmatrix} \quad (2.51)$$

where  $h_a^1(k_y)$  ( $h_b^1(k_y)$ ) stands for the interaction between two first(second) atomic layers in two adjacent principal layers through second nearest neighbor hopping.  $h_{ab}^1(k_y)$  represents the interaction between the second atomic layer in the first principal layer and its adjacent first atomic layer in the second principal layer.

$H_{SOC}$  is the spin-orbit coupling term that can be written as

$$H_{SOC} = \lambda \hat{L} \cdot \hat{S} \quad (2.52)$$

where  $\lambda = 0.0018Ry$  is the spin-orbit coupling constant for aluminum.  $\hat{L}$  and  $\hat{S}$  are angular momentum and spin operators of the system, respectively.

It is useful to express  $H_{SOC}$  as

$$H_{SOC} = \sum_{i;l,m} \lambda_{i;l} \left[ \frac{\hat{L}_{i;l}^+ \hat{S}_{i;m}^- + \hat{L}_{i;l}^- \hat{S}_{i;m}^+}{2} + \hat{L}_{i;l}^z \hat{S}_{i;m}^z \right], \quad (2.53)$$

where  $\hat{O}^\pm = \hat{O}^x \pm i\hat{O}^y$  are the standard ladder operators, with  $\hat{O} = \hat{L}, \hat{S}$ . One can distinguish two different contributions to the SOC Hamiltonian: the first term corresponds to a spin-flip process, and the latter is a spin-conserving term. Including spin-orbit coupling, the Green's function can be written as

$$G(\epsilon) = \begin{bmatrix} G_{\uparrow\uparrow}(\epsilon) & G_{\uparrow\downarrow}(\epsilon) \\ G_{\downarrow\uparrow}(\epsilon) & G_{\downarrow\downarrow}(\epsilon) \end{bmatrix} \quad (2.54)$$

where  $\epsilon = E \pm i\delta$ . Note that all the relevant quantities are evaluated at Fermi level with an imaginary convergent parameter of 0.002Ry which is carefully chosen to achieve

numerical stability with fast convergence speed.  $\Sigma_{R/L,\sigma}$  is the self-energy function of the left or right lead for electrons with up or down spin ( $\sigma = \uparrow, \downarrow$ ), defined as

$$\Sigma_{\alpha,\sigma} = t_{\alpha,\sigma}^\dagger g_{\alpha,\sigma}(\epsilon) t_{\alpha,\sigma}, \quad (2.55)$$

where  $g_\alpha$  is the interface Green's function of the semi-infinite left or right lead. Assuming that the spin-flip process only occurs in the scattering region, the transmission function is given by

$$T_{\uparrow\uparrow} = Tr[\Gamma_{L\uparrow} G_{\uparrow\uparrow}^r \Gamma_{R\uparrow} G_{\uparrow\uparrow}^a], \quad (2.56)$$

$$T_{\uparrow\downarrow} = Tr[\Gamma_{L\uparrow} G_{\uparrow\downarrow}^r \Gamma_{R\downarrow} G_{\downarrow\uparrow}^a], \quad (2.57)$$

where  $T_{\uparrow\uparrow}$  denotes the up-spin-conserving transmission function between the left lead and the right lead and  $T_{\uparrow\downarrow}$  refers to the transmission function with opposite spin states between the two leads.  $\Gamma_{\alpha\sigma}$  is the level width function for spin state  $\sigma$ . It broadens the width of energy level in the lead and is defined as

$$\Gamma_{\alpha\sigma} = i(\Sigma_{\alpha\sigma}(\epsilon) - \Sigma_{\alpha\sigma}^\dagger(\epsilon)). \quad (2.58)$$

## Chapter 3

# Electron and Spin transport in ultra-thin Al films

### 3.1 Introduction

Downsizing spintronic devices, which are essential for long-distance information transmission, has become crucial to achieve low power consumption, high data processing speed, and large integration densities. Decreasing spin diffusion lengths with thickness have been experimentally found, even in light metals with high conductivity and weak spin-orbit interaction (SOI), such as copper and aluminum [67, 16, 68, 55, 69, 70]. In recent years, there has been increasing focus on the spin transport properties in thin metallic Nonlocal Spin Valves (NLSVs) due to their significant potential as read heads [44, 46, 45] for magnetic recording, utilizing the output generated from giant magnetoresistance (GMR) effects [3, 4]. Many have been motivated to improve the head resolution and writing density by reducing the thickness of nonmagnetic materials used as transport channels, e.g. 2D materials [47, 48, 49] and light metals [50, 51]. However, experimental measurements have shown that the output signal of NLSVs diminishes rapidly, even with light metals as spin channels. In particular, for the thickness of a channel smaller than 10nm, the metallic spin valve performance declines substantially [52].

In this work, an ultrathin Al film is used to investigate the effect on the spin relaxation induced by surface roughness, GB scatterings, vacancy scatterings and surface reconstruction respectively, employing the Green's function method. Based on the Landauer-Büttiker formalism [60, 61], a 3.6nm thick Al system is connected to two semi-infinite and translationally invariant Al leads; resistivity, mean free path, spin diffusion length and EY constant  $\beta$  are determined at zero temperature using the transmission function  $T(E)$  which is obtained from the Green's function at the Fermi energy. Explicit contributions from grain boundaries, surface roughness and vacancies in the thin film regime are determined and compared with various experimental results. Our results can potentially widen the application of nonlocal spin valves for spintronics and magnetic recording read heads with smaller shield-shield spacing.

The section is presented by first providing the simulation details for a transport model that includes various sources of defects, followed by discussion of the results for momentum relaxation and spin relaxation induced by surface roughness, GB scattering, vacancy scatterings, surface reconstruction and anisotropy in spin relaxation in Sec. 3.4. A summary of the conclusions is in Sec. 3.5.

## 3.2 Methods

The simulation is conducted under the assumption that the system is in a surrounding vacuum. Both leads and the scattering region as shown in Fig. 3.1, are made of a thin film of Al with 3.6nm thickness. Periodic boundary conditions are applied with wavevectors sampled along the transverse direction (in the y direction as shown in Fig. 3.1), which achieves convergence within 6%. The other transverse direction (in the z direction as shown in Fig. 3.1) is treated in real space. As a result, surface roughness can be achieved with a one-dimensional surface height. For simplicity, the 1D surface height is generated by a Gaussian distribution function modulated by a Gaussian autocorrelation function with specified RMS height  $\delta h$  and correlation length  $\xi$ . First, a random Gaussian Surface is generated with a mean of 0 and standard deviation of  $\delta h$ . To smooth the random surface with a correlation length  $\xi$ , a 1D Gaussian auto-correlation function is defined as  $\exp(-x^2/2\xi^2)$ , where x is the position along the propagation direction. The resulting surface is computed by convoluting

the random Gaussian surface with the Gaussian auto-correlation function as a filter in Fourier Space and transforming back to the spatial domain.

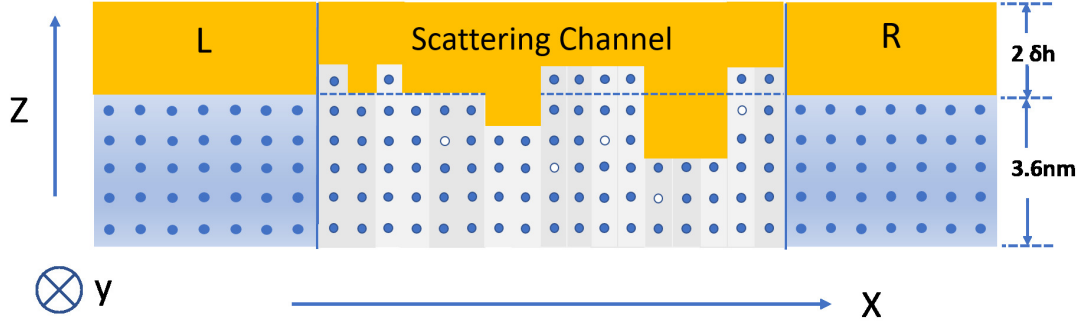


Figure 3.1: Schematic of the transport model in the presence of surface roughness and vacancies. L denotes the left lead and R denotes the right lead. To simulate the surface roughness, twice of  $\delta h$  is included in both leads and scattering region for surface bumps. The yellow region indicates the positions with 5 Ry added to simulate the vacuum environment. The white circles represent vacancies, which is achieved with 1.5 Ry onsite-offset potential exerted. Note that the transport model shown here is for visualization and the actual dimensions and scales of each region may vary.

Depending on the roughness of a surface, extra atomic layers equivalent to twice  $\delta h$  are preserved for atomic protrusions. A 5 Ry offset-potential is added to simulate the vacuum environment and missing atoms on the surface as indicated in the yellow region of Fig. 3.1. To ensure the 5 Ry offset potential effectively simulates the vacuum, without introducing a repulsive effect on the surface scattering, a modulation of the onsite-energy is provided at top and bottom surface layers, maintaining the electron occupancy of these two surface layers. The surface electron occupation number is determined by integrating the surface density of states to the Fermi level at  $T = 0$  K in the presence of the vacuum potential.

Grain boundary scattering is achieved by introducing grains whose size follows a log normal distribution [71]. Vacancies are introduced by adding a 1.5 Ry potential offset at the vacancy sites that is larger than the difference between the bottom of the band and the Fermi level. It is assumed that vacancies are randomly and uniformly



distributed with a probability  $C_{vac}$ , which denotes the vacancy concentration. Lastly, surface reconstruction is investigated with surface corrugations with varying periods and a random period, where a repeated pattern or random patterns of missing atoms are placed at the surface. All the quantities are computed by averaging over the number of defect configurations and the associated errors are determined from the standard deviation of the relevant quantities. Note that depending on the distributions followed by different types of defects, the number of defect configurations used in the simulations is deliberately chosen such that doubling the number kept the error within 5%.

### 3.3 Preliminary Results

To test the recursive Green's function algorithm, the transmission function for an infinite linear chain with only one orbital is computed, where the onsite energy is set to zero and the hopping constant  $t$  is equal to one as an energy unit.

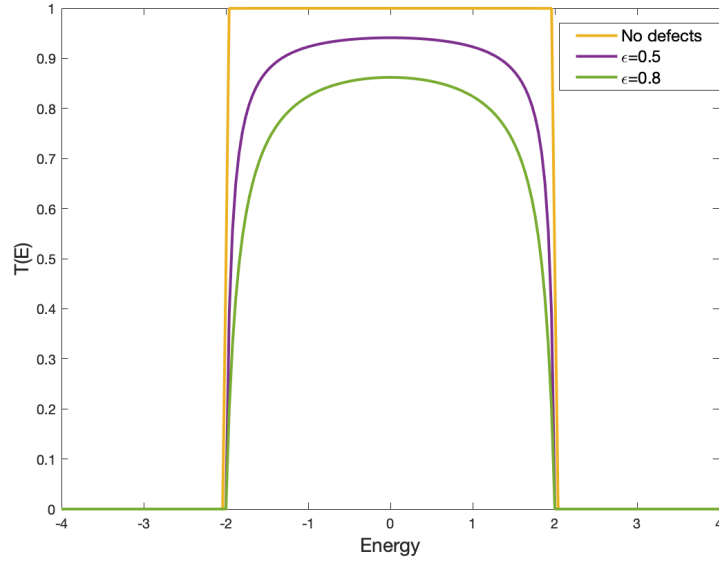


Figure 3.2: Transmission function for the linear chain (onsite energy  $E = 0$ , coupling  $t = 1$ ) without defects and with a single defect at  $\epsilon = 0.5$  and  $\epsilon = 0.8$ .

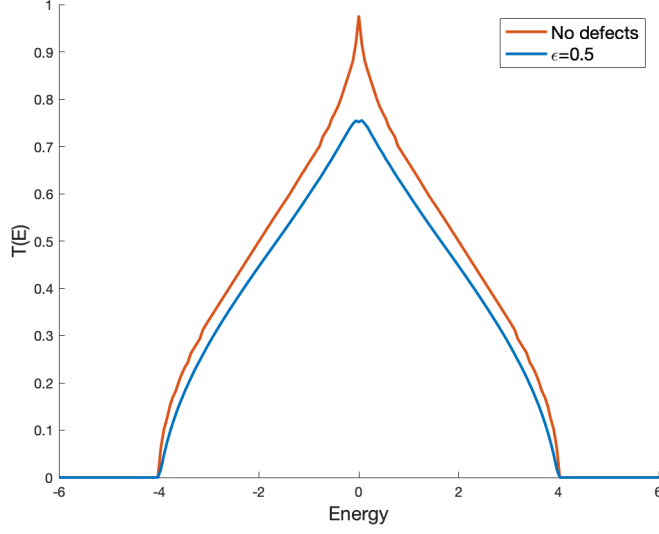


Figure 3.3: Transmittance of an infinite plane with a groove defect at  $\epsilon = 0.5$

With the parameters given above, the energy band is between -2 and 2. As shown in Fig. 3.2, without defects, the transmission has to be 100 % within the tight-binding band width and zero outside the band. As the energy of the defects increase, the transmission goes down because of the higher possibility to get reflected by defects, which is expected.

To test the reliability of the algorithm further, a higher dimension model of an infinite plane is used to compute the transmission function with a single groove, where the on-site energy in the groove is set to be one. In the transverse direction, the infinite linear chain is treated in momentum space. Then the infinite plane can be converted to an infinite linear chain with an onsite energy  $-2t \cos(ka)$ , where  $a$  is the lattice constant and  $t$  is the hopping term. Compared to the case of the linear chain, the energy band is wider, from -4 to 4, which is expected. The transmission function is also zero outside that range. As shown in Fig. 3.3, there exists a singularity at  $E = 0$ , which is attributed to a Van-Hove singularity in the density of states of the infinite plane at  $E = 0$ . As expected, the presence of defects lowers the transmission function as it does in the linear chain.

Next, the density of states is calculated via the Green's function method, which is given by

$$g_{dos}(E) = -\frac{Im[Tr(G^r(E))]}{\pi},$$

where  $Tr$  denotes the trace of the Green's function. Fig. 3.4 shows the density of states of Al calculated under the periodic boundary conditions by the Green's function method and by directly diagonalizing the Hamiltonian. As expected, both methods produce the same result for the DOS of Al, which again indicates the reliability of the Green's function method and the accuracy of the code.

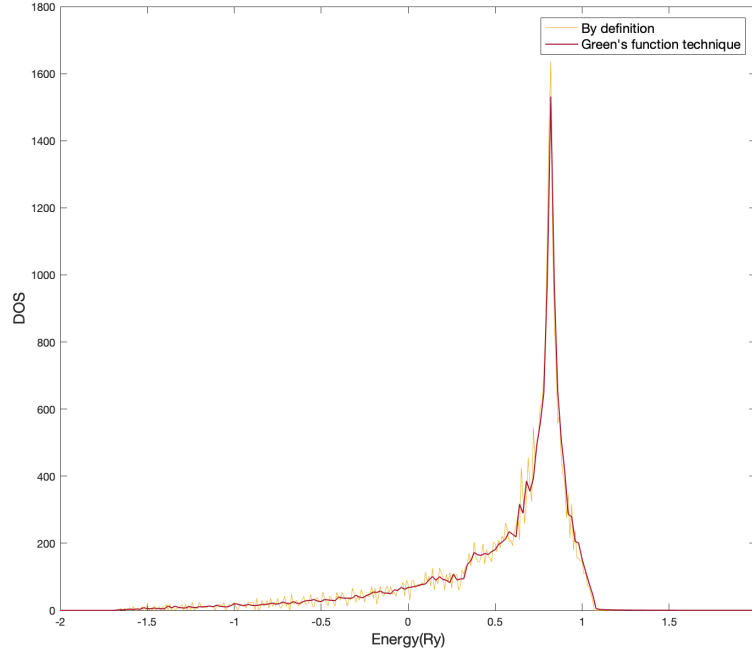


Figure 3.4: Density of states computed by Green's function technique with  $\delta = 0.002$  and by counting the numbers of states at each energy level through diagonalizing the Hamiltonian.

## 3.4 Results and Discussion

### 3.4.1 Surface Roughness

From the transmission function predicted by the Green's function, resistivity can be obtained through  $G(E) = 2e^2T(E)/h$ , where  $G$  is conductance. Assuming that the size effect on the density of states and Fermi velocity can be neglected and the Drude model for the free-electron is valid in the system with defects, then the momentum relaxation rate  $\tau_p^{-1} \propto \rho$  and the mean free path is given by  $\lambda_{\text{mfp}} = \sqrt{3}/\rho g e^2 v_F$ , where the density of states at the Fermi level  $g = 2.4 \times 10^{28} \text{ eV}^{-1}\text{m}^{-3}$  and Fermi velocity  $v_F = 2.03 \times 10^6 \text{ m/s}$  [72]. The effective mass of a 3.6 nm-thick system with defects is estimated to be  $\sim 90\%$  of the predicted values determined by the SK parameters and hence the free electron assumption will be accurate to within 10%. Spin diffusion length is determined from spin polarization  $P$ , which is defined as  $P = (T_{\uparrow\uparrow} - T_{\uparrow\downarrow})/(T_{\uparrow\uparrow} + T_{\uparrow\downarrow})$  and  $P \propto \exp(-d/L_{\text{sd}})$  in the diffusive regime, where  $L_{\text{sd}}$  is the spin diffusion length and  $d$  is the channel length. The EY constant  $\beta$  is determined by  $\beta = \tau_s/\tau_p = (L_{\text{sd}}/\lambda_{\text{mfp}})^2$ .

As shown in Fig. 3.5(a), the resistivity due to surface roughness  $\rho_{\text{surf}}$  exhibits an ohmic behavior as expected for the cases where the root mean squared height  $\delta h$  is below 1.0 nm and the lateral correlation length  $\xi = 10 \text{ nm}$  or  $20 \text{ nm}$ . A minor tunneling effect occurs when  $\delta h$  is increased to 1.0 nm. The fact that an increase in resistivity and a decrease in spin diffusion length correlate to the rougher surfaces demonstrates that the surface roughness enhances the momentum and spin relaxation.

As shown in Table 3.1, the values of resistivity scale linearly with  $\delta h/\xi$ , i.e.  $\rho \propto \delta h/\xi$ . Note that an  $\sim 10\%$  difference in  $\rho$  is observed in Table 3.1 between the case where  $\delta h = 0.4 \text{ nm}$  and  $\xi = 10 \text{ nm}$  and that where  $\delta h = 0.8 \text{ nm}$  and  $\xi = 10 \text{ nm}$ , which have the identical ratio of  $\delta h/\xi$ . But this difference is within the uncertainty, which increases with the surface roughness.

$\delta h/\xi$  can be understood as the average slope of the surface protrusions. An increase in  $\delta h/\xi$  leads to a steeper slope of the surface bumps, which will increase the backscattered probability for electrons and hence a higher resistivity is expected. This result is consistent with the model for surface roughness scattering dependent on resistivity proposed in Ref. [73] (by Zhang et al.) at the sub-10nm regime of thickness. In contrast, it has been shown that treating surface roughness perturbatively in the Kubo linear

response theory [74, 54] brings about  $\delta h^2$  dependence in resistivity, i.e.  $\rho \propto \delta h^2$ . This discrepancy arises because the first order perturbation treatment on surface roughness is not well justified. In particular, at the sub-10nm regime of film thickness where surface scattering dominates, the electron coherence length is comparable to the lateral correlation length such that the resulting wave function for the electron scattering is associated with multiple scattering events and cannot be described independently.

In order to extract the spin diffusion length, the range of the channel lengths is chosen to consistently correspond to the values of  $\ln(P)$  between 0.6 and 1.0, which effectively avoids a slight curvature at a small channel length in the spin diffusion plot. The slight curvature is attributed to the contact resistivity between the leads and the scattering channels and the transition between the ballistic and diffusive transport. As shown in Fig. 3.5(b), the linearity is restored in the chosen range of the channel lengths. It is observed that  $\beta_{surf}$  ranges from  $\sim 300$  to  $\sim 1000$  with the imposed surface roughness contrary to a relative constant value based on Elliott-Yafet theory. More specifically,  $\beta_{surf}$  shows a roughly linear dependence on  $\delta h/\xi$  as well. The wide range of  $\beta_{surf}$  arises from the fact that the spin-flip scattering is more resilient to the variation of surface roughness compared to the momentum relaxation.

It is found that the spin diffusion length is proportional to  $(\delta h/\xi)^{-1/2}$  in contrast to the linear dependence on  $\delta h/\xi$  of both  $\beta_{surf}$  and  $\rho_{surf}$  as illustrated in Fig. 3.6. Consequently, the corresponding spin relaxation rate is invariant with respect to  $\delta h/\xi$ , and the  $(\delta h/\xi)^{-1/2}$  dependence of spin diffusion length is completely attributed to momentum relaxation based on  $L_{sd} = \sqrt{D\tau_s}$  where the diffusion constant  $D = 1/ge^2\rho$  according to the Einstein relation. Considering that the spin coherence length is appreciably larger than the characteristic size of surface bumps or dents, it is apparent that within the channel length of interest, the effective scattering potentials are the collective outcome of multiple surface features, which is likely to outweigh the spin flip scatterings induced by each individual surface feature.

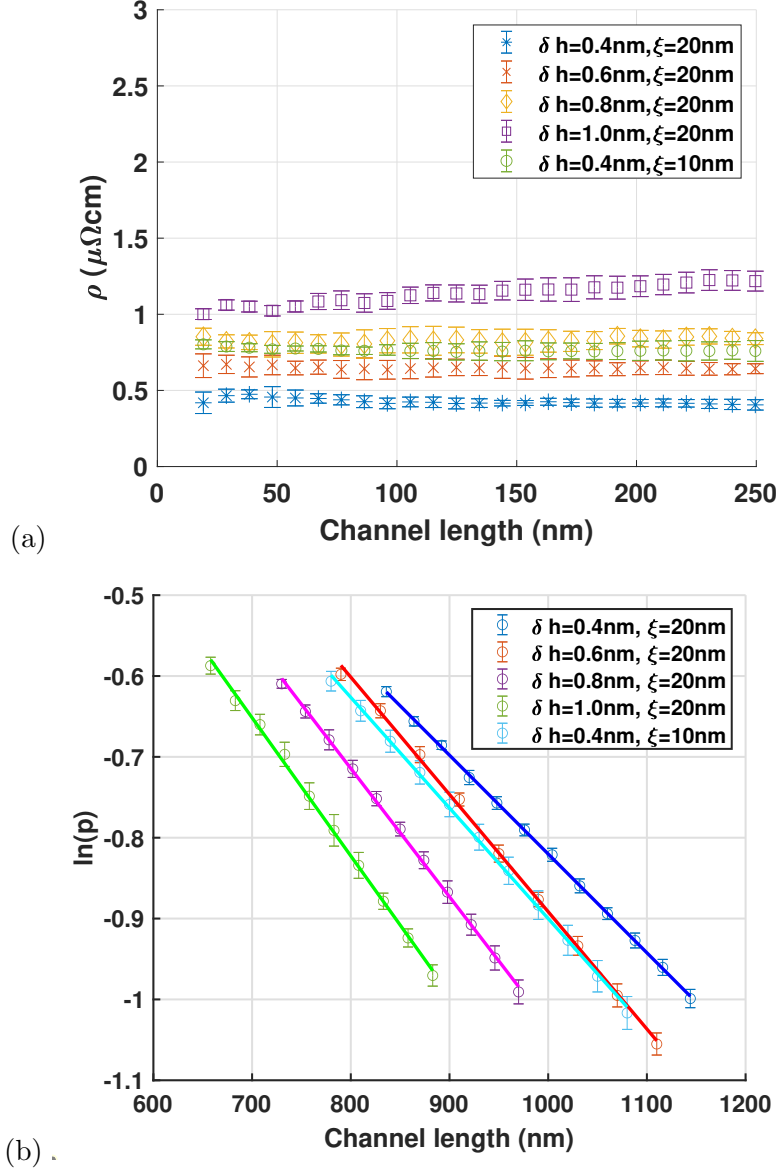


Figure 3.5: (a) Resistivity of Al with 3.6 nm thickness versus channel length under different sets of surface roughness parameters. (b) Spin diffusion lengths under the same sets of roughness parameters as above.  $P$  is the spin polarization.

Table 3.1: Summary of the effect of surface roughness on electric and spin transport in a 3.6 nm-thickness Al film at  $T = 0$  K.

$\delta h(nm)$	$\xi(nm)$	$\rho(\mu\Omega \cdot cm)$	$L_{sd}(nm)$	$\beta_{surf}$
0.4	20	0.42	820	248
0.4	10	0.75	731	630
0.6	20	0.67	693	452
0.8	20	0.83	645	600
1.0	20	1-1.2	583	861 <sup>1</sup>

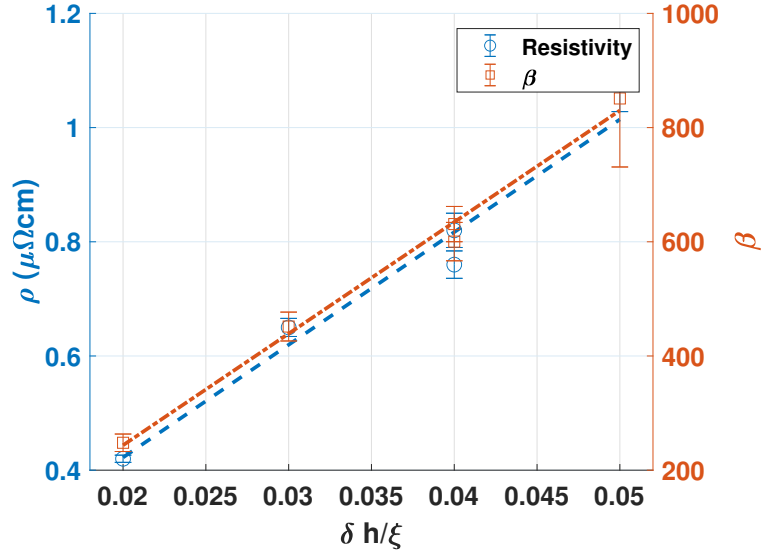


Figure 3.6: Resistivity of 3.6 nm thick film varies with  $\delta h/\xi$  in blue and the corresponding  $\beta$  in red. The fitting dashed lines are used to show the linear trend. Note that the larger error bar for  $\delta h/\xi = 0.05$  is due to the weak tunneling effect.

Overall, the values of resistivity are in a reasonable range compared to the simulated results from Ref. [54] after scaling with respect to thickness and surface roughness parameters. Note that the simulations in this article are executed with one-sided roughness

<sup>1</sup> determined with  $\rho = 1.1\mu\Omega \cdot cm$ , which is the average value.

imposed rather than double-sided as in the actual experiments. Assuming the surface roughness of top and bottom interfaces are uncorrelated and independent, the resulting momentum and spin relaxation rates will be approximately doubled. However, compared to the experimental results [75, 76, 77, 78], in particular, to that from Ref. [55], both resistivity and spin diffusion length are approximately one order of magnitude removed from the typical values for  $t_N < 25\text{nm}$  when accounting for the thickness [79, 80] and double-sided roughness, indicating that the dominant effect on the relaxation cannot be attributed to the surface roughness. Typically, as shown in Table 3.7,  $\rho$  is  $\sim 10\ \mu\Omega\cdot\text{cm}$ ,  $L_{sd}$  is between 100 nm and 1000 nm and  $\beta$  is  $\sim 10^4$  for  $10\text{ nm} < t_N < 20\text{ nm}$ .

### 3.4.2 Grain Boundary Scattering

Several factors have been investigated for GB scattering. Grain boundary spacing follows a log-normal distribution and grain boundaries are treated as potential barriers with heights and thickness. Two GB thicknesses  $t_{GB}$ , 0.4 nm and 0.8 nm, are used in our simulations since typical metallic grain boundary thickness is  $\sim 0.5\text{ nm}$  [81]. Given that the potential barrier height of the grain boundary strongly depends on the material and GB structure, two types of grain boundary barrier  $V_{GB}$  (-0.05 Ry and -0.2 Ry) are being studied, where -0.05 Ry is a potential drop for a typical GB barrier with impurities and -0.2 Ry is a potential drop to simulate oxidized grain boundaries. The relationship between the grain size and  $\rho_{GB}$  is also examined with average grain sizes  $d_{GB}$  of 50 nm and 30 nm which are realistic values measured in thin films [55]. For simplicity, only perpendicular grain boundaries are considered in the simulation.

Table 3.2: Summary of the effect of grain boundaries on electric and spin transport in a 3.6 nm-thickness Al film at T = 0 K.

$d_G(\text{nm})$	$V_{GB}(\text{Ry})$	$t_{GB}(\text{nm})$	$\rho(\mu\Omega \cdot \text{cm})$	$L_{sd}(\text{nm})$	$\beta_{GB}$
30	-0.05	0.8	0.13	$3.6 \times 10^4$	$4.5 \times 10^4$
50	-0.2	0.4	0.23	$1.6 \times 10^4$	$2.8 \times 10^4$
30	-0.2	0.4	0.34	$1.4 \times 10^4$	$5.5 \times 10^4$
Continued on next page					



---

30	-0.2	0.8	0.72	$0.9 \times 10^4$	$8.6 \times 10^4$
----	------	-----	------	-------------------	-------------------

---

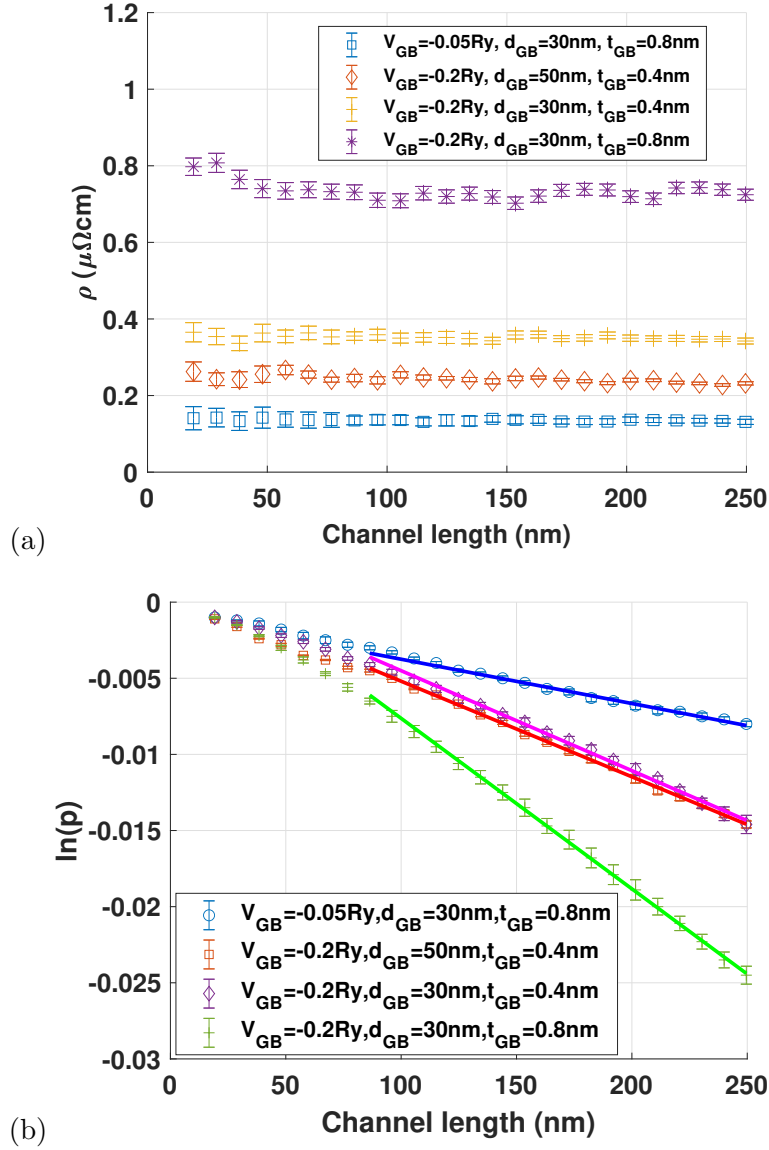


Figure 3.7: (a) Resistivity of 3.6 nm thick film versus channel length for different grain boundary parameters. (b) Spin diffusion lengths for a 3.6 nm thick channel under the same sets of grain boundary parameters as above.

As shown in Table 3.3 and Fig. 3.7(a) and 3.7(b), momentum and spin relaxation rates grow inversely with grain size and increase with increasing GB barrier and GB thickness, suggesting that momentum and spin relaxation are both enhanced by the grain boundaries. Note that because the spin diffusion length induced by grain boundaries is approximately two orders of magnitude larger compared to the surface-induced relaxation, available computational resources make it impossible to achieve the channel-length range corresponding to the value of  $\ln(P)$  that falls between 0.6 to  $\sim 1.0$ . To be consistent, a fixed channel-length range is used from 110 nm to 250 nm. But compared to the resulting spin diffusion lengths, the chosen channel-length range is too small to confirm the linear behavior, causing a relatively large uncertainty on the spin diffusion length. With the imposed practical GB parameters, the contribution of GB scattering to the momentum relaxation is generally at the same order but weaker than that of surface scattering. In addition,  $\rho_{GB}$  and  $L_{GB}$  are found to be at least one order of magnitude away from the experimental results as shown in Table 3.7. And  $\beta_{GB}$  is almost two orders of magnitude larger than  $\beta_{surf}$  in general, indicating that the contribution to spin relaxation induced by grain boundaries is negligible compared to that induced by surface roughness with the imposed parameters at sub-10nm thickness. Symmetry can account for the weak momentum and spin relaxation. With the imposed grain boundaries, translational symmetry along the traverse and thickness directions are preserved and thus momentum and spin relaxation are undermined as scatterings can only occur in the propagation direction.

Overall, it is still inconclusive regarding the exact dependence of the momentum and spin relaxation on the imposed GB parameters, given a relatively large uncertainty involved in the spin relaxation and weakly scattered GB parameters imposed. However, neither surface scattering nor GB scattering seem strong enough to account for the experimental results.

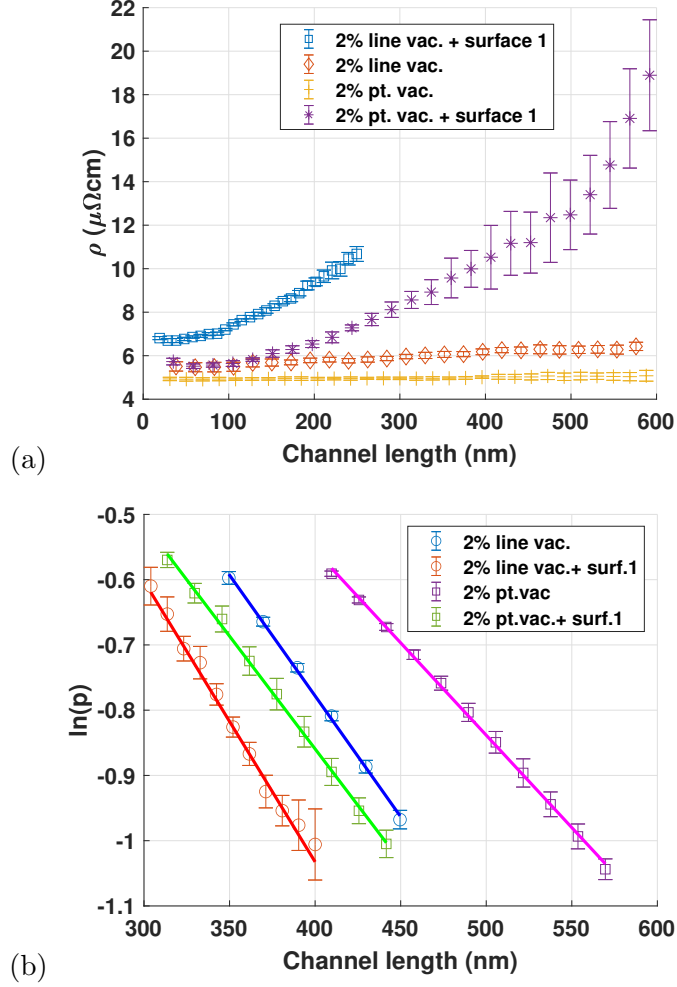


Figure 3.8: (a) Resistivity of 3.6 nm thick film versus channel length with 2% line vacancies (with surf.1) in purple (blue) and 2% point vacancies (with surf.1) in yellow (red); surface 1 is modulated by  $\delta h = 0.8$  nm and  $\xi = 20$  nm. Note that the case with the 2% line vacancies and surface 1 is only plotted to 250nm because the strong tunneling effect makes the transmission function too small to acquire an accurate resistivity. (b) Spin diffusion lengths for a 3.6 nm thick channel under the same condition as above.

### 3.4.3 Vacancy Scattering

Table 3.3: Summary of the effect of 2% vacancies on spin transport in an Al film with 3.6 nm thickness at  $T = 0$  K.

Relaxation Mechanism	$\rho(\mu\Omega \cdot cm)$	$L_{sd}(nm)$	$\beta$
line vacancies	nonohmic	270	-
line vac. + surf.1 <sup>2</sup>	nonohmic	233	-
point vacancies	4.95	353	6400
point vac. + surf.1	5.83	290	6000

So far, the effects of both surface roughness and grain boundary scattering on the properties of electron and spin transport in an Al thin film are not sufficiently strong to explain the experimental findings. Thus, a new source of scattering from vacancies is studied. 2% vacancies are assumed to be uniformly distributed throughout the thin film [82]. The effects of line vacancies and point vacancies with/without surface roughness on electronic and spin transport are simulated.

As shown in Fig. 3.8 (a), a strong tunneling effect occurs in the presence of line vacancies. However, in the presence of point vacancies,  $\rho$  recovers ohmic behavior, which indicates that point vacancies are a more realistic assumption, as expected. Note that the channel length in Fig. 3.8 (a) is extended to  $\sim 600nm$  to demonstrate the strong tunneling effect owing to the line vacancies and the ohmic character of resistivity for the point vacancies, i.e, resistivity is independent of channel length. For readability and accuracy, the resistivity for the case combining 2% line vacancies and surface roughness is only plotted to 250 nm. Hence, owing to the ohmic character of resistivity, the extraction of  $\beta$  with resistivity and spin diffusion length determined at different ranges of channel length is well-justified for surface roughness and point vacancies used in the simulation. Yet, one may argue that a weak tunneling effect presented in the case with surface roughness modulated by  $\delta h = 1.0$  nm and  $\xi = 20$  nm (Fig. 3.5 (a)) can result in channel-length dependent  $\beta$ . However, this case is only included as a marginal case to show the strong scattering effect of surface roughness considering that twice of  $\delta h$  could reduce the sample thickness to 1.6 nm.

Based on the combined resistivity from 2% point vacancies and surface roughness, a

<sup>2</sup> surface roughness modulated by  $\delta h = 0.8nm$  and  $\xi = 20nm$

3.7 nm mean free path can be obtained for the 3.6 nm thick sample in the presence of a rough surface with  $\delta h = 0.8\text{nm}$  and  $\xi = 20\text{ nm}$ , which is comparable to the experimental measurement [55]. Notice that both spin and momentum relaxation rates are smaller in the presence of point vacancies than line vacancies, which is expected as the vacancies along the traverse direction enhance the electron reflections and spin flip events. As shown in Table 3.3, the resistivity with the presences of both surface roughness and point vacancies is the sum of the resistivity from each individual source, i.e  $\rho_{pt.vac.+surf.} \approx \rho_{pt.vac.} + \rho_{surf.}$ , which is consistent with Matthiessen's rule within 5%. Compared to the resistivity induced by surface roughness, under reasonable assumptions, vacancy scattering is dominant over surface scattering for momentum relaxation.

Table 3.4: Summary of resistivity induced by vacancies at  $t_N = 3.6\text{ nm}$  and  $T = 0\text{ K}$ .

$C_{vac}$	0.1%	0.2%	0.4%	0.8%	1.0%	2.0%
$\rho(\mu\Omega \cdot cm)$	0.32	0.62	1.17	2.13	2.61	4.95

As shown in Table 3.4, a linear vacancy concentration dependence is found in  $\rho_{vac}$  when the vacancy concentration is below 1.0%, which can also be predicted analytically from the Green's function method as in Ref. [83]. In the diffusive regime, resistivity is inversely proportional to the product of the channel number  $M$  across the Fermi level and an ensemble average transmission function  $\bar{T}$ , i.e.  $\rho \propto 1/M\bar{T}$ . For a system with uniformly and independently distributed vacancies of a concentration  $C_{vac}$ , the correlation function for the vacancy scattering potential  $\Delta$  between any two sites is

$$\begin{aligned} \langle \Delta_{i,n,s} \Delta_{i',n',s'} \rangle &= \delta_{i,i'} \delta_{n,n'} \delta_{s,s'} (C_{vac} \Delta^2 - C_{vac}^2 \Delta^2) \\ &\quad + C_{vac}^2 \Delta^2, \end{aligned}$$

where  $i$ ,  $n$  and  $s$  are the indices for the position along the transverse and longitudinal directions respectively.

Transmission amplitude  $t_{k_1,k_2}$  (from incoming wave with transverse mode  $k_1$  at one lead to an outgoing wave with  $k_2$  at the other lead) and reflection amplitude  $r_{k_1,k_2}$  can be written in terms of Green's function as follows.

$$t_{k_1,k_2} = i\sqrt{v_{k_1}v_{k_2}}G_{0,k_1;N+1,k_2}^r, \quad (3.1)$$

$$r_{k_1, k_2} = i\sqrt{v_{k_1}v_{k_2}}(G_{0, k_1; 0, k_2}^r - \frac{\delta_{k_1, k_2}}{iv_{k_1}}), \quad (3.2)$$

with  $G_{m, k_1; n, k_2}^r = \langle m, k_1 | G^r | n, k_2 \rangle$ , where  $|m, k\rangle$  represents the generic electronic state of  $m_{th}$  longitudinal layer with transverse mode  $k$ .  $v_k$ , group velocity of transverse mode  $k$  is given by  $\frac{\partial Ef}{\partial k}$ . Using Dyson's equation,

$$G_{0, k; 0, k'}^r = g_{0, k; 0, k'}^r + \sum_{i=1}^N g_{0, k; i, k}^r V_{k, k'}^i g_{i, k'; 0, k'}^r \quad (3.3)$$

Here  $V_{k, k'}^i = \sum_{s, n} \phi_k^\dagger(n, s) \phi_{k'}(n, s) \Delta_{i, n, s}$ .  $\phi_k(n, s)$  denotes the wavefunction for an electron state  $|n, k, s\rangle$ . Based on the expression of reflection amplitude,  $iv_k g_{0, k; 0, k'}^r = \delta_{k, k'}$ . Then,  $r_{k, k'} = i \sum_i \sqrt{v_k v_{k'}} g_{0, k; i, k}^r V_{k, k'}^i g_{i, k'; 0, k'}^r$ . Applying Dyson's equation and collecting the terms linear in the channel length  $L$ , the reflection amplitude

$$\begin{aligned} \langle |r_{k, k'}|^2 \rangle &= 1/v_k v_{k'} \left( \sum_i \langle V_{k, k'}^i V_{k, k'}^{\dagger i} \rangle + \sum_{i \neq j} \langle V_{k, k'}^i V_{k, k'}^{\dagger j} \rangle \right) \approx L \sum_{n, s} C_{vac} (1 - C_{vac}) \Delta^2 \\ &\quad \times [|\phi_k(n, s)|^2 |\phi_{k'}(n, s)|^2 / v_k v_{k'}]. \end{aligned}$$

In the weak scattering limit (in the system with dilute vacancies),

$$1/M\bar{T} \approx 1/M + \sum_{k, k'} \langle |r_{k, k'}|^2 \rangle / M^2.$$

Ignore the contact resistivity (first term),

$$\rho \propto \sum_{n, s} C_{vac} (1 - C_{vac}) \Delta^2 [|\phi_k(n, s)|^2 |\phi_{k'}(n, s)|^2 / v_k v_{k'}].$$

Given that  $C_{vac} \ll 1$ , the linear dependence on  $C_{vac}$  can be seen. As the linear dependence on the vacancy concentration is derived from the independence of the vacancy distribution, when the vacancy concentration increase above a certain value, the associated scattering potential starts to overlap and interact, causing the deviation from linearity. This deviation from the linear dependence is observed when  $C_{vac}$  is above 1.0% as illustrated in Fig. 3.9 and the better quadratic fitting suggests that the vacancy overlapping matters as  $C_{vac}$  increases above 1.0%. Note that the quadratic fitting equation given in the form of  $y = 284.2x(1 - 6.56x)$  rather than in the form of  $C_{vac}(1 - C_{vac})$

as predicted, suggests that the interaction between vacancies is stronger than the prediction and a higher order of expansion in Dyson's equation is required to correctly describe it.

Note that the different effects on the momentum relaxation can be attributed to the nature of isolated defects and clustered defects. The features of surface roughness can be understood as the clusters of multiple vacancies, forming an effective scattering potential locally which is attenuated by the interaction of the local scattering potential associated with each vacancy. Therefore, the resulting  $\rho_{surf}$  is characterized by  $\delta h/\xi$ . In contrast, for the system with dilute vacancies, the average inter-vacancy separation  $d_{vac}$  is of comparable magnitude as  $\xi$  or longer so that it is safe to consider that each scattering event associated with each isolated vacancy is independent and additive, leading to  $\rho_{vac} \propto C_{vac}$ . Hence, momentum relaxation is more susceptible to point vacancy than surface roughness in the thin film regime.

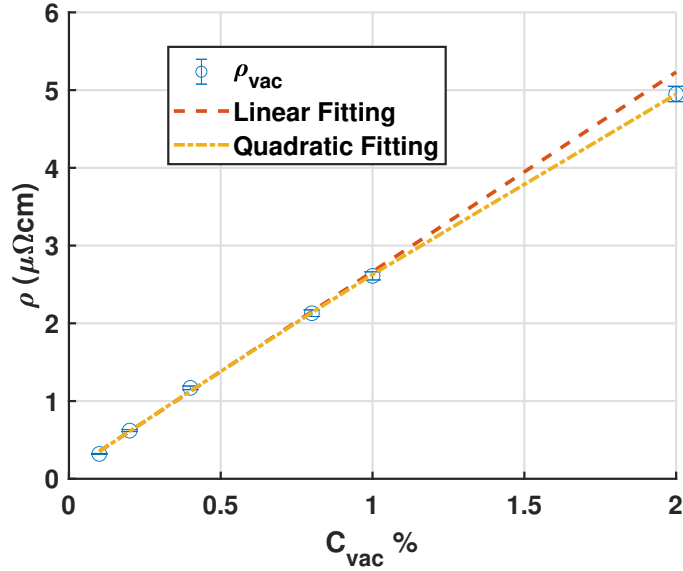


Figure 3.9: Resistivity of 3.6 nm thick film varies with  $C_{vac}$  in blue; the linear fitting on  $C_{vac}$  in a red dashed line and the quadratic fitting on  $C_{vac}$  in a yellow dashed line with the fitting equation  $y = 284.2x(1 - 6.56x)$ .

As given in Table 3.3 and Table 3.1, the spin diffusion length due to vacancies is generally  $\sim 2$  times shorter than that induced by surface roughness at  $t_N = 3.6\text{nm}$  while

the corresponding resistivity is more than 5 times larger. Consequently,  $\beta_{vac}$  is one order of magnitude larger than  $\beta_{surf}$ . This reflects the difference between bulk and surface defects. Generally, a surface band is narrower than a bulk band within a system which leads to a smaller electron level spacing or an energy gap  $\Delta E$ . Thus, a larger  $\beta_{vac}$  is expected, following  $\beta = (\Delta E/\lambda_{SOI})^2$  as predicted by Elliott-Yafet theory. This reflects the energy broadening due to spin flip scattering being suppressed by the surface energy spacing.

#### 3.4.4 Surface Reconstruction

Table 3.5: Summary of the effect of surface reconstruction on electric and spin transport in an Al film with 3.6 nm thickness at T = 0K.

$\delta w(nm)$	$C_{vac}\%$	$\rho(\mu\Omega \cdot cm)$	$L_{sd}(nm)$	$\beta_{recon+vac}$ <sup>3</sup>
0.4	0	0.06	1020	7.9
0.4	0.1	0.47	377	66
0.8	0.1	0.68	332	107
0.4	0.4	1.69	198	235
0.8	0.4	2.3	202	443
0.4	0.8	3.02	175	585
0.4	1.6	5.3	166	1620
RSC <sup>4</sup>	0.0	1.39	650	1710
RSC	0.1	1.96	325	850
RSC	0.4	2.96	245	1079
RSC	0.8	3.70	210	1265
RSC	1.6	5.60	190	2371

Spin and momentum relaxation induced by surface reconstruction has also been studied. A repetitive indentation with a given period is repeatedly placed at the top surface

<sup>3</sup> The extraction of  $\beta$  is based on its definition, which does not necessarily imply EY mechanism is responsible for the derived value.

<sup>4</sup> RSC symbolizes random surface corrugations



to simulate the surface reconstruction, equivalent to 50% missing atoms at the surface. To investigate the combined effect of point vacancies and surface reconstruction, 0.1%, 0.4%, 0.8% and 1.6% point vacancies are included along with surface reconstruction.

It is observed that the presence of surface reconstruction and point vacancies enhance both spin and momentum relaxation and the simulation results become similar to the experimental measurements. Note that constant resistivity is observed as shown in Fig. 3.10 (a). Thus, it is accurate to use the resistivity determined at 250 nm as representative to extract  $\beta$ .

As shown in Table 3.5, a nearly zero resistivity indicates that electron scattering due to the repetitive surface corrugation is negligible owing to little symmetry breaking in the propagation and transverse directions. The possibility of ballistic transport for periodic surface corrugations cannot be ruled out, although the signature trend as demonstrated in Fig. 4 in Ref.[84] is not observed. Given the nearly zero resistivity, the associated spin relaxation can be explained by the Rashba effect [85, 86] originating from the symmetry breaking in the thickness direction due to the surface corrugation such that the intra-band scattering matrix element is nonzero, i.e. causing the intraband spin scattering.

To investigate the effect of periodicity of surface reconstruction, random corrugations are introduced on the surface to replace the repetitive surface corrugations such that the resulting width of the average surface plateau is 0.8 nm without periodicity. As shown in Table V, in the presence of 0.1% vacancies, comparing the case with 0.8 nm-width repetitive surface corrugation to that with random surface corrugations, the resulting resistivity is increased  $\sim 300\%$  from  $0.68 \mu\Omega \cdot cm$  to  $1.95 \mu\Omega \cdot cm$  but the associated spin diffusion length merely decreases  $\sim 2\%$ . This suggests that the periodicity of surface corrugation breaks the connection between momentum relaxation and spin relaxation as indicated by the change of  $\beta$  in Table 3.5. Surface periodicity effectively mitigates the momentum relaxation owing to symmetry such that the electron momentum corresponding to the width of the surface corrugation is robust against backscattering, leading to a consistently smaller resistivity induced by periodic surface corrugations (PSC) compared to that induced by random surface corrugations (RSC).

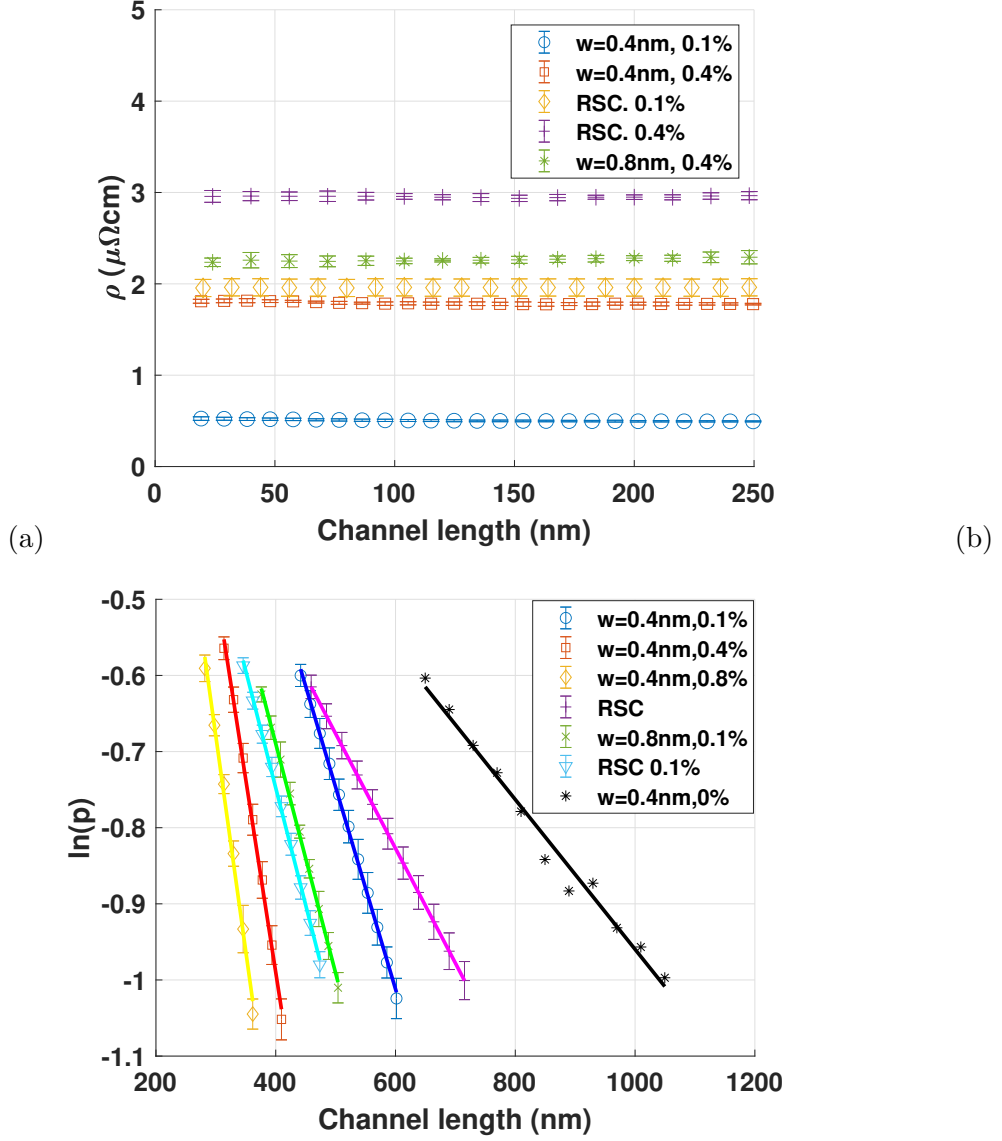


Figure 3.10: (a) Resistivity of 3.6 nm thick film versus channel length in the presence of periodic surface corrugations/random surface corrugations and 0.1%, 0.4% point vacancies.(b) Spin diffusion lengths for a 3.6 nm thick film with varying widths of surface corrugation and varying vacancy concentration.

In addition, a clear departure from Matthiessen's rule of resistivity is observed. For

example, the sum of  $\rho_{vac}$  with 0.1% vacancies (from Table 3.4) and  $\rho$  due to random surface corrugation as in Line 8 of Table V mispredicts the combined resistivity by  $\sim 15\%$ . In contrast, increasing the concentration of vacancies further breaks the symmetry along the propagation direction, leading to the increase in resistivity and the effective removal of the deviation from Matthiessen's rule. For instance, Matthiessen's rule accurately predicts the resistivity within 5% for the case of 0.8% vacancies and RSC.

Furthermore, the introduction of point vacancies results in further amplification of spin relaxation as shown in Fig. 3.10(b), which again is attributed to loss of inversion symmetry along the thickness direction and propagation direction. The resulting spin diffusion lengths for the cases with 0.4% vacancies or above are approximately 5 times shorter than the case with periodic surface corrugations alone. Interestingly, 0.1% vacancies brings about a spin diffusion length 2.5 times shorter ( $\sim 1000$  nm to  $\sim 400$  nm), but doubling from 0.4% to 0.8% vacancy concentration only decreases the spin diffusion length by  $\sim 10\%$  as shown in Table 3.5. Similar to the enhancement of momentum relaxation owing to the induction of random corrugations, this suggests that the inefficacy of periodic surface corrugations in relaxing spin momentum is easily broken by any kind of randomness in the system, even 0.1% vacancies.

Following EY theory,  $L_{sd} = \sqrt{3\beta}/\rho g(E_F)e^2v_F^2$ . As shown in Fig. 3.11, a fairly good fitting based on the EY theory in red with a reasonable  $\beta_{RSC+vac}$ . ( $1434 \pm 138$ ) suggests that EY prediction is valid for the cases with RSC. However, for the cases with PSC and vacancies, the presence of the positive constant term in the blue dash line violates the EY mechanism which predicts a linear relation between  $L_{sd}$  and  $\rho^{-1}$  with a constant  $\beta$  and a zero constant term. This can be attributed to the different responses to the symmetry breaking between momentum relaxation and spin relaxation, which closely depends on the scattering length scale and concentration of random defects. In the presence of PSC, the length scale associated with symmetry breaking is determined by the average distance of vacancy separation, which is comparable or longer than the typical length of momentum relaxation ( $\sim 10$  nm) depending on the vacancy concentration. Thus, symmetry can be better preserved at the typical scattering length of momentum relaxation ( $\sim 10nm$ ) than that at the typical length of spin relaxation ( $\sim 300nm$ ) such that electron transport within the typical length of momentum relaxation is nearly ballistic owing to PSC, while the spin transport between the spin scatterings is diffusive.

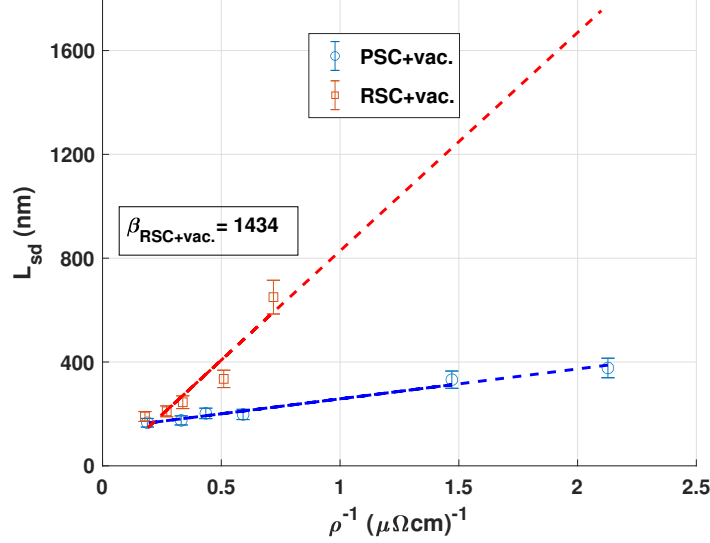


Figure 3.11:  $L_{sd}$  versus  $\rho^{-1}$  for all the cases shown in Table 3.5 except the case with PSC alone. The fitting equations are  $y = 115.2x + 143$  for vacancies and PSC in the blue dash line and  $y = 841x - 13.3$  for vacancies and RSC in the red dash line. The associated  $\beta_{RSC+vac.}$  is determined from the slope.

In contrast, the introduction of random surface corrugations breaks the translational symmetry at a much smaller length scale such that symmetry breaking is comparable at both length scales of momentum relaxation and spin relaxation. Note that the positive correlation between  $\beta_{PSC+vac.}$  and  $C_{vac}$  as shown in Table 3.5 could indicate that as the vacancy concentration increases, a non-constant  $\beta$  is attributed to the reduced contribution of surface spin-flip scattering [87], which has a larger spin-flip probability ( $1/\beta$ ) than that of bulk scattering. This is still inconclusive, however, as separating surface scattering from bulk scattering cannot be achieved accurately, limited by the departure from Matthiessen's rule. In addition, a clear overlap is observed between PSC and RSC at a larger vacancy concentration shown in Fig. 3.11, suggesting the Elliott-Yafet prediction is expected to recover when the bulk scattering dominates. This is also indicated by the relatively small difference between  $\beta_{1.6\%,PSC}$  (1620) and  $\beta_{1.6\%,RSC}$  (2371).

Compared to the cases with the presence of both surface roughness and 2% point

vacancies, the combined effect of point vacancies and 0.4nm-width surface corrugations gives rise to  $\sim 2$  times shorter spin diffusion length and therefore  $\sim$ one order of magnitude smaller  $\beta$  when the associated resistivities are of comparable magnitude.

Although surface corrugation is a special case of surface reconstructions, it reflects the significance of periodicity in momentum and spin relaxation, which can be extended to other surface reconstructions that have localized periodicity.

### 3.4.5 Anisotropy of Spin Relaxation

So far, spin relaxation has been studied for the spins along z direction, i.e. thickness direction as shown in Fig. 3.1. By rotating the spin basis of  $H_{so}$  to transverse directions, anisotropic spin relaxation is explored with two representative cases: a system with surface corrugations with the periodicity of 0.4 nm and 0.8% point vacancies and a system with 2% vacancies. Defining the eigenstates  $\sigma_x$  and  $\sigma_y$  as  $|\pm x\rangle = (1, \pm 1)/\sqrt{2}$  and  $|\pm y\rangle = (1, \pm i)/\sqrt{2}$ , respectively,  $H_{so}$  can be rewritten accordingly. As shown in Table 3.6, clearly the largest difference in spin diffusion lengths distinguishes the x direction (direction of surface corrugation periodicity) from the others. It is traceable to the surface corrugations: it vanishes within the film plane (x and y directions) when the corrugation is removed. There is also a second smaller anisotropy between the direction perpendicular to the plane (z) and parallel to the plane as one would expect from Rashba arguments as presented in Ref. [88]. The spin diffusion length for x spins is always found to be the largest, in qualitative agreement with the experimental Ref. [88] which, however, has edge effects not included in the periodically connected thin film used in this work.

Table 3.6: Summary of anisotropy of spin transport in an 3.6nm thick Al film with 0.4 nm periodicity of surface corrugation and 0.8% vacancies or 2% vacancies alone at T=0K.

$w = 0.4nm$	$C_{vac} = 0.8\%$	$C_{vac} = 2.0\%$
$L_{sd,x}(nm)$	490	492
$L_{sd,y}(nm)$	207	475

$L_{sd,z}(nm)$	175	353
----------------	-----	-----

Table 3.7: Summary of the experimental results on spin transport in Al-NLSV at T= 4K (Adapted from Ref.[52])

$t_N(nm)$	$\rho(\mu\Omega \cdot cm)$	$L_{sd}(nm)$	$\beta \times 10^4$	Ref.
6	33.3	200	9.0	[75]
8.5	9.5	70	0.07	[55]
10	9.1	420	2.95	[75]
12	9.52	455	3.80	[76]
15	2.5	660	0.55	[43]
20	5.2	450	1.11	[77]
20	4	850	2.34	[78]

### 3.4.6 Spin Hot Spots

To check the effect of spin hot spots, the variation of spin polarization with respect to the  $k$  vectors in the presence of surface roughness is examined. The outliers in spin polarization appear in a ratio of 1/20. The total transmission for the outliers are about half of that for regular  $k$  points. This implies that even for the 50% mixing of spin when  $P = 0$ , the removal of those outliers will only increase  $P$  by  $\sim 5\%$ . Thus, the inclusion of those outliers does not contribute much to the spin flip scattering that significantly changes an order of magnitude of spin relaxation time. It make senses because the presence of surface roughness breaks the space inversion symmetry and removes the contribution of spin hot spots as it effectively lifts the degeneracy of spin states and makes the band structure around the Fermi level smoother. Similarly, other defects which serve to break the space inversion symmetry can also smear out the spin hot spots, such as grain boundary, vacancies or surface corrugation.

### 3.5 Conclusion

In this paper, the effects of surface roughness, GB scattering, vacancies and surface reconstruction on the momentum and spin relaxation are investigated in a Al thin film with  $t_N = 3.6\text{nm}$  at  $T=0\text{K}$ . Point vacancies are found to be the dominant contribution to the momentum relaxation as the resulting resistivity is similar to experimental measurements, while the resistivity induced by the other defects are at least one order of magnitude smaller. Spin relaxation is dominated by the combined effect of surface reconstruction and point vacancies, which leads to  $L_{sd} \approx 200\text{nm}$  and  $\beta \leq 1000$  with a reasonable assumption of vacancy concentration.

It has been observed that the presence of surface corrugation results in a clear departure from Matthiessen's rule. The violation of the EY prediction for  $\beta$  is found in the presence of periodic surface corrugations and vacancies. This is attributed to the different responses to symmetry breaking between momentum relaxation and spin relaxation as symmetry breaking is not comparable at both length scales of momentum and spin. In addition, a strong anisotropy of spin relaxation for the spins parallel to the propagation direction is found, relevant to surface corrugations.

It has been found that the spin diffusion length induced by surface roughness is proportional to  $(\delta h/\xi)^{-1/2}$  as opposed to  $(\delta h/\xi)^{-1}$ , which can be attributed to the interference between multiple surface features. A linear vacancy concentration dependence is found for resistivity when the vacancy concentration is below 1.0% and a departure from linearity is attributed to the interaction between the vacancy scattering potentials.

## Chapter 4

# Part II: Micromagnetics

### 4.1 History of Hard Disk Drives

The history of hard disk drives (HDDs) spans several decades and is characterized by significant technological progress that has revolutionized data storage and computing. The initial attempt to recording information with magnetism can be dated back to the late-19th century. In 1877, the concept of magnetic recording was first proposed by the American engineer Oberlin Smith and later demonstrated practically by Danish engineer Valdemar Poulsen in 1898, who developed the first magnetic wire recorder, also referred to as the telegraphone [89]. The fundamental principle of the telegraphone became the norm for subsequent magnetic recording and playback designs: an information-coded electrical signal was received by a recording head, which then generated an associated magnetic field that wrote a magnetic pattern onto a recording medium where it persisted until demagnetized by external magnetic fields. Once recorded in the medium, the magnetic pattern can be sensed by a read head and converted into an electrical signal.

However, limited by capacity and performance, these early-stage storage devices were not massively commercialized until the post-war period. In 1956, IBM introduced the IBM 350 which was included in the IBM 305 RAMAC (Random Access Method of Accounting and Control) computer system, which is widely recognized as the world's first commercial hard disk drive. It featured a stack of fifty 24-inch diameter and 1/8-inch thick disks and had a storage capacity of 5 megabytes with an areal density of



2kB/in<sup>2</sup>. This innovation marked a significant milestone in magnetic recording technology and laid the foundation for modern HDDs. The HDD soon replaced magnetic tape drives as the dominant secondary storage in computer systems.

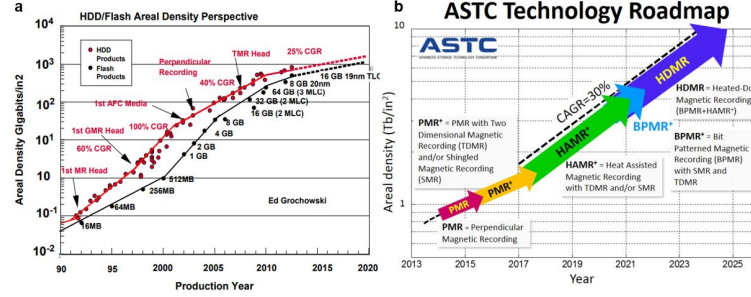


Figure 4.1: a. Areal density evolution of HDDs from Ref. [90]; b. the ASTC roadmap of areal density from Ref. [91].

Although flash memory-based solid state drives (SSDs) offer superior read and write speeds, durability, and energy efficiency compared to HDDs in mobile devices, HDDs continue to thrive due to their low cost per bit. This cost advantage puts HDDs in a favorable position to accommodate the demand for storing and processing more than 100 zettabytes of data in the current big data era, ten times the amount of data being produced in 2017 [92]. Ever since the HDD was invented, consistent effort has been devoted to improve its reliability and areal density which refers to the storage capacity per unit area in the disk platter of HDDs. Increasing areal density is essential to meet the growing demand for higher storage capacities, compatibility for a wider range of digital devices, enhanced energy efficiency and cost-effective storage solutions. Until 2015, the areal density of HDDs reached about  $1Tb/in^2$ , 8 orders of magnitude larger than the IBM 350 in 1956, driven by the introduction of giant magnetoresistance (GMR) and perpendicular magnetic recording (PMR) and other breakthroughs in recording media and read head designs [93, 94, 95].

However, due to the inherent limitations in magnetic recording (magnetic recording trilemma), the current prevailing recording technology, PMR, has slowly plateaued and reached its saturation limit of  $1Tb/in^2$  for areal density, as depicted in Fig. 4.1 [100]. Therefore, it is imperative to explore next-generation magnetic recording technologies

to replace PMR for sustainable growth in the areal density of HDDs.

Among all the next-generation recording techniques, Heat-assisted magnetic recording (HAMR) is usually regarded as the solution for higher areal density to succeed contemporary PMR. This is evidenced by the roadmap of areal density projection by Advanced Storage Technology Consortium (ASTC) in Fig. 4.1, representing the consensus from industry. In 2023, Seagate, the leading company for mass-capacity storage solutions, revealed its long-term technology roadmap, outlining plans to introduce hard drives with capacities of approximately 50 TB by 2026 and exceeding 120 TB by 2030. By Incorporating bit-patterned media (BPM) and other advanced recording technique, the projection of HAMR's areal density can reach up to approximately  $10 \text{ Tb/in}^2$ , 10 times higher than what PMR can offer [96]. Thus, hard disk drives will continue to be the predominant cost-effective data storage solution for the foreseeable future.

#### 4.1.1 Structure of HDDs

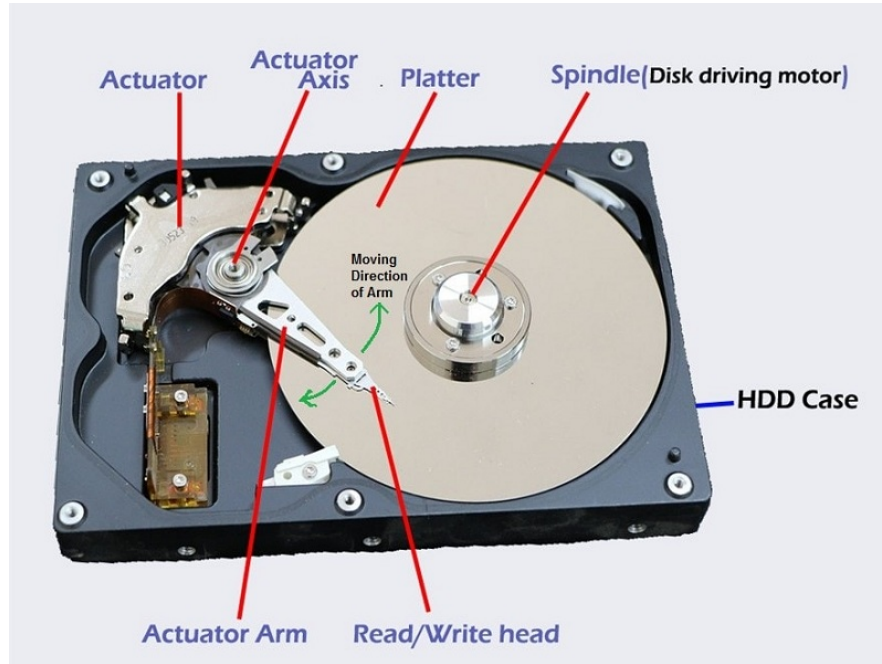


Figure 4.2: the basic structure of an HDD [97].

Fig. 4.2. illustrates the structure of HDDs with the key components labeled. A typical structure of a Hard Disk Drive (HDD) consists of several key components: platters, spindle motors, read/write heads, actuator arm and controllers. Platters are circular, metallic disks coated with a magnetic material storing magnetic information, mounted on a spindle driving the rotation of platters at high speeds (usually 5,400 to 15,000 revolutions per minute). Each platter has a read/write head mounted on a slider controlled by an actuator arm. The actuator arm positions the read/write heads over the correct location on the platters to read or write data, enabling read/write heads fly a few nanometers above the surface of platters. When approaching the media, the read/write heads read back signals from, and write information, to the platters by magnetizing or detecting changes in the magnetic patterns. The controller is a circuit board that manages the operation of the HDD. It communicates with the computer's operating system, controls the movement of the actuator arm, and handles data transfers between the platters and the computer's memory.

## 4.2 Magnetic Recording Trilemma

The magnetic information stored is binary, represented by a string of magnetization directions of each individual grain in the media. The actual recording media consists of grains with varying shapes and sizes and hence each bit with a given bit length has to be stored with several grains to ensure the coded information is retrieved correctly. To achieve high-precision readback, reducing the volume of grain enables higher signal to noise ratio (SNR) with larger number of grains per bit, which also favors high areal density.

However, the reduced volume of the grain compromises the thermal stability, which is detrimental to long-term storage reliability. This is attributed to the superparamagnetic effect: when reaching to a critical grain size, the magnetization of each grain is randomized due to thermal fluctuation even at room temperature, exhibiting similar properties as paramagnetism [99]. To compensate for the superparamagnetic effect, the energy barrier associated with thermal fluctuation between two energy minimum states demands a substantial anisotropy to balance the reduced volume. In general,  $K_u V / k_B T > 60$  is required to achieve a long term room-temperature storage of more

than 10 years, where  $K_u$  denote anisotropy,  $V$  is the volume of grain,  $k_B$  is Boltzmann constant and  $T$  represents temperature.

Writability, however, may be compromised with high anisotropy. Higher writability enables faster and more efficient data recording processes. As reliable recording requires the switching magnetic field be approximately equal to the anisotropy field  $H_k$ , equal to  $2K_u/M_s$ , high write field is necessary for achieving high writability and thermal stability, which is largely determined by the material and other components of the write head. The current upper limits stands at approximately 1.7 T. Furthermore, increasing head fields also requires the re-calibration of the magnetic properties of other components in HDDs to ensure consistent and stable performance for high writability.

This challenge to balance three key factors in magnetic recording technology (areal density (SNR), writability, and stability) is referred to as the trilemma of magnetic recording [98]. Addressing this trilemma for higher areal density and reliability is crucial to the future of the HDD industry; it requires careful optimization of magnetic materials, recording techniques, and device design to achieve a balance among areal density, writability, and stability. Ongoing research and endeavor focus on various strategies such as engineering magnetic materials with enhanced stability, using exchange-coupled or composite structures, or employing advanced recording techniques like heat-assisted magnetic recording (HAMR) or bit-patterned media (BPM).

### 4.3 From LMR to PMR to HAMR

The transition from longitudinal magnetic recording (LMR) to perpendicular magnetic recording (PMR) was marked by Toshiba's release of its first commercial PMR-based HDD products in 2005 [94], primarily motivated by achieving high areal density through the PMR design [101]. In conventional "longitudinal" magnetic recording, the magnetization of granular recording media is oriented parallel to the medium surface. A typical ring-shaped inductive write head generates a longitudinal fringing field that magnetizes the medium circumferentially along the down-track direction. However, at high recording density where bits are closely packed, the adjacent bits with opposite polarities can generate a strong demagnetizing field, leading to bit destabilization [102]. Additionally, smaller bits require a thicker medium to maintain sufficient coercivity, which yields an

even stronger unfavorable demagnetizing field.

In contrast, PMR aligns magnetic bits perpendicularly to the medium surface, thereby reducing the undesirable demagnetization field at the transition region. To enhance writability in PMR, a soft magnetic underlayer (SUL) is affixed beneath the recording medium, creating a closed magnetic flux loop. The incorporation of the SUL, coupled with the small pole-tip of the write head, enables a strong magnetic field to be generated between the pole tip and the soft underlayer by the dense flux beneath the small pole-tip. Consequently, materials with larger anisotropy and smaller grain size can be used as the recording medium, favoring high areal density recording.

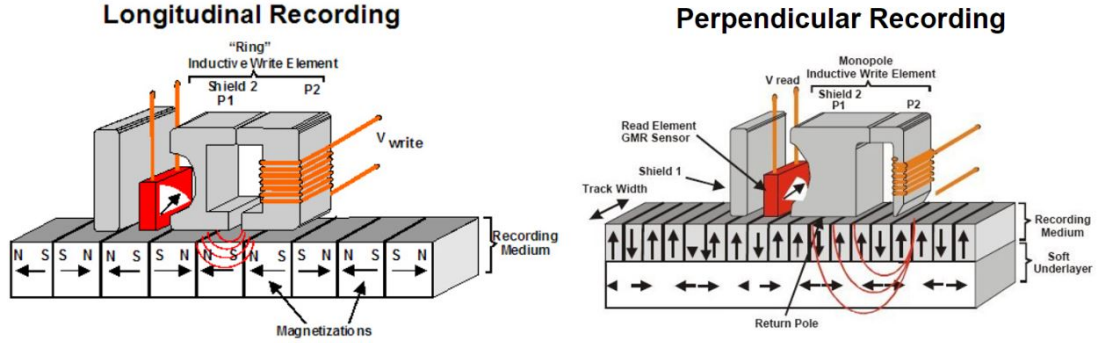


Figure 4.3: The basic illustration of longitudinal magnetic recording and perpendicular magnetic recording from Ref. [103].

#### 4.3.1 HAMR

Further increase in the areal density of HDDs demands new magnetic recording technology to surpass the saturation limit of PMR, such as heat-assisted magnetic recording (HAMR), and microwave-assisted magnetic recording (MAMR). In particular, HAMR, as the leading technology for next-generation magnetic recording, addresses the magnetic trilemma by decoupling writing from the storage process such that the competing requirements of writability, thermal stability and high areal density can reach consensus. Achieving high writability involves temporarily and locally heating medium to a lower coercivity. This is accomplished by a high-Ku medium that is locally heated with

a laser to a temperature near or above its Curie temperature where the coercivity is significantly reduced, allowing writing with a smaller head field. Within a nanosecond, the recorded bit is cooled down to the room temperature where the restored high  $K_u$  ensures the information is stored with long-term thermal stability. This allows reliable writing with a sufficiently small grain volume in the presence of limited head field. Additionally, with proper matching heat source and media thermal design, HAMR can offer larger effective field gradient, promoting higher areal density as well. The recording process is illustrated in Fig. 4.4.

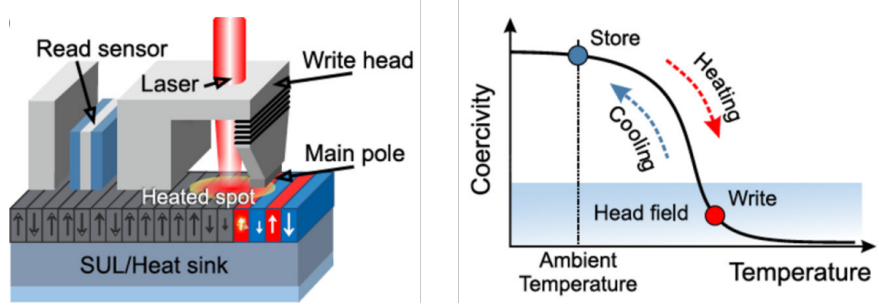


Figure 4.4: The schematic of HAMR demonstrating its recording mechanism [104].

### Near-Field Transducer

To ensure reliable recording in HAMR, a novel optical system with a laser must be integrated into the design of the HAMR write head to deliver optical energy transiently to a narrow spot with precision. This requirement is crucial for achieving fast heating and cooling, enabling high data rates and sharp transitions, and for accommodating high areal densities. The high areal densities demands a narrow heating spot for smaller bit lengths. For achieving densities of  $1Tb/in^2$ , the heat spot dimension is expected to be less than 50 nm [105]. However, the diffraction limit of optical spot size ( $d$ ) for focused propagating light waves in the far field prevents conventional laser focus-heating to meet this requirement, as defined by the equation  $\lambda/2NA$  (where  $\lambda$  is the wavelength and  $NA$  denotes the numerical aperture of the focusing lens) [106].

To overcome the bottleneck of the diffraction limit, a plasmonic near-field transducer (NFT) incorporated with a planar solid immersion mirror is utilized to confine optical waves to a narrower spot than the incident wavelength in Fig. 4.5. As shown in Fig.

4.5a, a typical ‘lollipop’ design of NFT consists of a metallic disk and a rectangular peg. When light is absorbed by the disk, the free electrons in the metal oscillate collectively in response to the incident electromagnetic radiation, generating a much stronger optical intensity of surface plasmonic current known as surface plasmon resonance. These surface plasmons converge along the outside edge of the disk to the peg, whose width is much narrower than the diffraction limit. This enables the tight confinement of the enhanced field and efficient delivery of optical energy to the recording medium below.

In summary, the plasmonic NFT is integrated into the write head of the HDD. When a laser beam is focused onto the NFT, plasmonic resonance generates a highly localized and intense near-field hotspot at the surface of the recording medium. Thus, higher areal density can be achieved with a narrower heat spot. To ensure a fast cooling cycle within approximately 1 ns and efficient heat conduction, a heat sink and an interlayer are attached to the recording medium to regulate the heat flow from the storage layer.

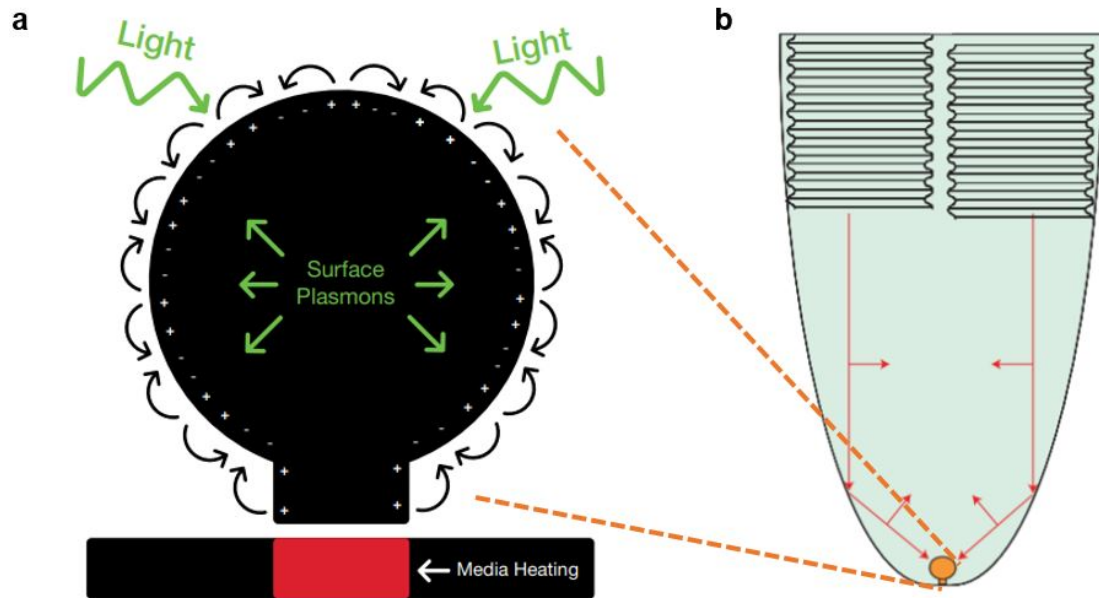


Figure 4.5: a. A illustration of a "lollipop" NFT heating a HAMR media [107]; b. A PSIM converging light waves to NFT [106].

### 4.3.2 HAMR Media

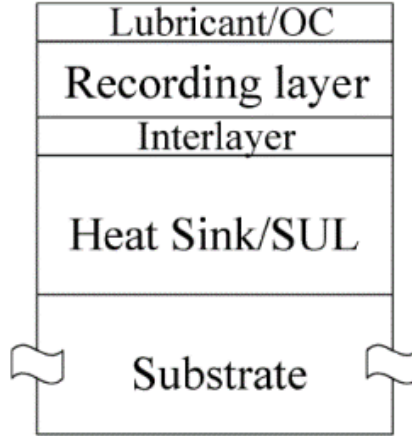


Figure 4.6: A schematic drawing of HAMR media consisting of a recording layer and functional layers from Ref. [109].

Fig. 4.6 illustrates the typical structure of HAMR media comprising a recording layer and functional layers. The recording layer, coupled with a lubricant and overcoat layer above it, is incorporated with an interlayer (control of magnetic property and microstructure) and a heat sink underlayer, which is supported by a substrate at the bottom. Based on the mechanism of HAMR, a solid HAMR media should present a well-ordered granular structure with high  $K_u$ , narrowly-distributed grain size, as well as a desirable thermal response for sharp transitions, including an efficient lateral heat flow confinement and vertical heat conductivity.

Table 4.1 includes several high- $K_u$  material as potential candidates for HAMR media, where  $K_u$  denotes magneto-crystalline anisotropy,  $M_s$  represents saturation magnetization,  $H_k$  is anisotropy field,  $T_c$  labels Curie temperature and  $DP$  is the minimum diameter to maintain thermal stability  $> 60k_B T$ . Among the materials listed in Table 4.1,  $\text{SmCo}_5$  exhibits the highest anisotropy,  $\sim 20 \times 10^7 \text{ erg/cm}^3$ , representing rare earth transition metals. And yet rare earth materials generally present fabrication challenges and corrosion issues at room temperature, which make it unsuitable for long-term storage. Some multilayer structures also exhibit moderately large anisotropy  $\sim 1 \times 10^7$



erg/cm<sup>3</sup> generated by the interface, yet the  $\sim 6.6$  nm threshold grain size diameters make it less appealing for data storage with high areal density.

Table 4.1: A list of high-Ku magnetic materials from Ref. [108].

Type	material	$K_u$	$M_s$	$H_k$ (KOe)	$T_C$ (K)	$D_P$ (nm)
Co-alloy	CoCr <sub>20</sub> Pt <sub>15</sub>	0.3	330	18.2	-	14.4
	Co <sub>3</sub> Pt(L1 <sub>2</sub> )	2	1100	36.3	-	6.9
L1 <sub>0</sub> alloys	FePd	1.8	1100	33	760	5.0
	FePt	6.6-10	1140	116	750	2.8-3.3
	CoPt	4.9	800	123	840	3.6
	MnAl	1.7	560	69	690	5.1
RE <sup>1</sup>	Fe <sub>14</sub> Nd <sub>2</sub> B	4.6	1270	73	585	3.7
	SmCo <sub>5</sub>	11-20	910	240-400	1000	2.2-2.7

L1<sub>0</sub> ordered alloys generally offers high anisotropy and reasonably small critical diameters for high thermal stability. In particular, L1<sub>0</sub> phase FePt exhibits the highest anisotropy,  $\sim 7 \times 10^7$  erg/cm<sup>3</sup>, among all of the L1<sub>0</sub> phases material considered in Table 4.1. Generally, however, achieving high Ku through elevated anneal temperatures during fabrication process can compromise the grain size distribution, potentially aggravating transition noise in HAMR application. Moreover, another critical parameter for achieving reliable HAMR performance is T<sub>c</sub>. Given that the writing process occurs near T<sub>c</sub>, it strongly influences the effective field gradient and largely dictates the operating temperature of the medium structure, thereby determining the recording quality. Hence, materials used for overcoats and lubricants as well as the design of the NFT must be tailored accordingly based on T<sub>c</sub>.

Additionally, stronger thermal fluctuations at the writing temperature due to higher T<sub>c</sub> value can degrade transition quality, thus adversely affecting recording performance. Moreover, the heat sink functional layer is also a key component to achieve high recording performance by promoting high thermal gradients and efficient heat conduction in vertical direction. Commonly used materials for heat sink layers include noble metals

<sup>1</sup> RE: rare earth transition metals

such as Au and Ag, as well as Al, Cu, and Cr which promote efficient vertical heat flow. Overall, L1<sub>0</sub> phase FePt remains a promising magnetic material for HAMR application, offering favorable properties for achieving high recording performance.

#### 4.3.3 Noise in HAMR

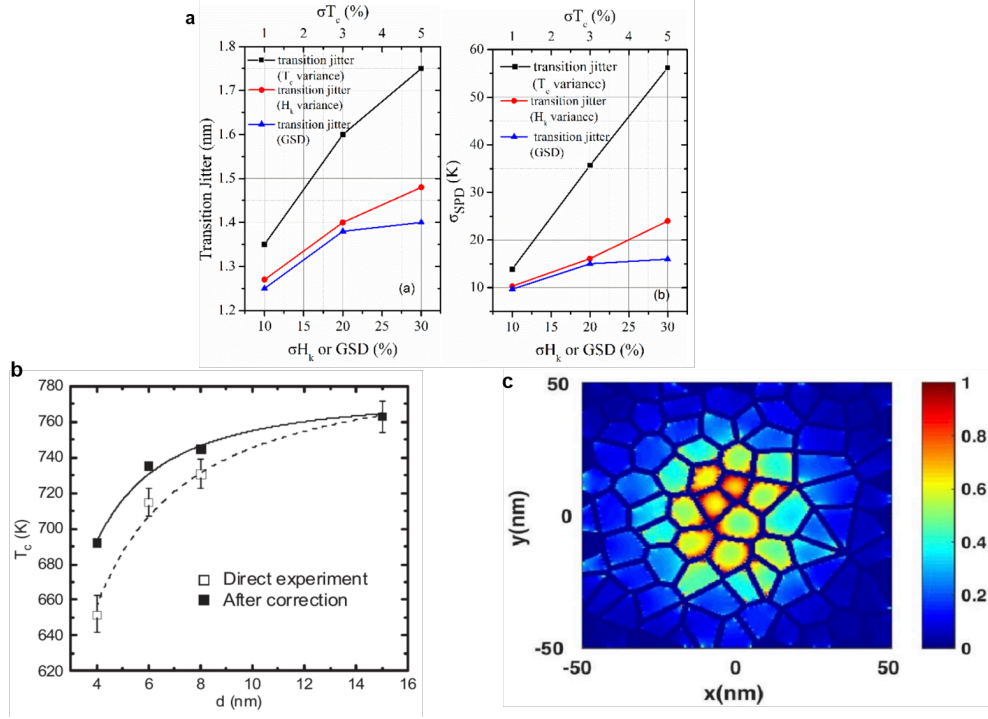


Figure 4.7: Typical HAMR noise contributors; a.  $\sigma T_c$  and  $\sigma H_k$  degrade transition jitters [113]; b. The Curie temperature dependence on grain size [114]; c. The grain geometry induced variation of power absorption [115].

In general, the medium noise in HAMR system typically falls into two categories, transition noise and remanence noise [146, 147, 148]. Transition noise stems from the variations of opposite magnetic polarity between two adjacent bits. Transition jitter serves as a common metric to evaluate the transition noise, representing the down-track variation of magnetic transition positions. On the other hand, remanence noise, also known as DC noise, is dominated by the thermal fluctuation during the cooling process. It is

crucial to understand the nature of HAMR noises and their impact on the recording performance for effectively addressing the noise-related challenges.

The introduction of thermal effects complicates the medium noise with temperature dependence, in addition to the existing PMR noise associated with anisotropy field variance and randomness of grain geometry. The total medium noise primarily includes the contributions from Curie temperature variance, thermal fluctuation, structural randomness in grains and the variations in anisotropy fields [150]. Given the HAMR mechanism, the writing process occurs near the Curie temperature where the magnetization and anisotropy momentarily enter a superparamagnetic state, i.e. effective magnitude close to zero. As a result, the switching of grains are driven mostly by the write head field and thermal fields. Thus, the recording quality significantly depends on thermal fluctuation and other temperature-dependent noise sources. In particular, variation of  $T_c$  across different grains, originating from the doping-induced chemical and magnetic ordering variation or grain size distribution, can cause the local grain switching at different temperatures, reducing the switching efficiency and quality.

Fig. 4.7.b illustrates a significant variation in  $T_c$ , especially in the HAMR grains smaller than 6 nm [113]. Moreover, structural randomness in HAMR media, including variations in magnetic grain size, shape, thickness, air gaps, and grain boundaries, can induce significant fluctuations in optical power absorption, leading to a further localized temperature variation on the media [114, 115]. In addition, the noise induced by anisotropy field variance and grain size distribution inherent to PMR is magnified even more with a smaller grain size in HAMR. This is because during fabrication process, high anneal temperature introduces further randomness in the grain size. The larger variation in recording temperature will in turn widen the Hk dispersion, further degrading the recording performance.

#### 4.3.4 Thermal exchange coupled composite media

Although tremendous progress has been achieved with the design and reliability in NFT, microstructure and magnetic properties of the recording medium, yet noise mitigation and media fabrication remains the primary challenges to improve the areal density of HAMR [141]. Intrinsically, HAMR suffers from superparamagnetism and thermal noise issues, such as  $T_c$  variance,  $K_u$  variance and grain size distribution. In particular,

as the writing occurs around the  $T_c$  of the storage medium, the recording quality is significantly affected by the Curie temperature distribution [140].

To mitigate the  $T_c$  variance of HAMR media, thermal exchange coupled composite (ECC) media was first proposed by Victora and Liu, et.al [119]. ECC consists of two layers: a superparamagnetic writing layer and storage layer. The recording process is initiated in the write layer that is magnetically softer than the long-term storage layer, commonly made of  $L1_0$  FePt. Via exchange coupling between the writing layer and storage layer, the coded information can be copied to the FePt layer during cooling process. This usually occurs at a temperature higher than the writing temperature of FePt whose  $T_c$  is lower. Because the recording process in the storage layer is initiated by exchange coupling from the writing layer and write head field at lower temperature, the dependence on the variance in  $T_c$  of the storage layer is reduced/removed. This two-stage writing process enables ECC to exhibit a robust tolerance to  $T_c$  variance of the storage layer and strong tunability of writing temperature, thus improving the recording efficiency and quality [119, 120].

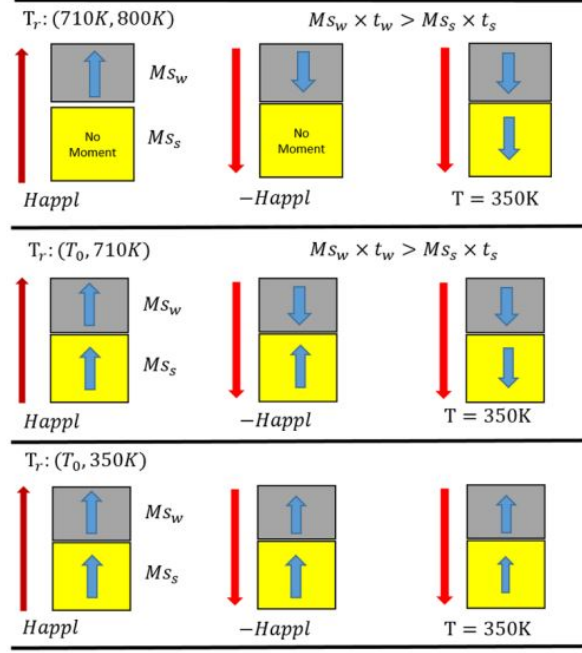


Figure 4.8: Illustration of switching mechanism in thermal ECC media initiated at different temperatures and cooled to 350 K (3rd column) [119].

Fig. 4.8 illustrates the switching mechanism of ECC medium.  $T_0$  denotes the highest temperature without switching [119]. As shown in the top row of Fig. 4.8, when temperature exceeds the writing temperature of the storage layer, the writing process of the top layer is initiated while the storage layer is still in its paramagnetic states, confining the writing process to the top layer alone. As temperature further reduces, the information written in the top layer can be copied and transferred into the storage layer. With properly chosen anisotropy of top layer, this process can occur at a temperature higher than  $T_c$  of a single storage layer, thus reducing/removing the dependence of  $T_c$  variance in the storage layer.

The second row illustrates the case when temperature lies between room temperature and writing temperature  $T_{sw}$ ,  $350K < T < T_{sw}$ . In this case, the reversal of top layer is attributed to its smaller anisotropy field and thus higher effective field while the information in the storage layer is protected by its high anisotropy. This reveals the potential of ECC design to protect the stored information from the adjacent track

writing. The last row illustrates the stability of long-term storage in the ECC design thanks to the high anisotropy of both layers at room temperature.

### Noise Mitigation

The probability of thermal switching is one of the key parameters in understanding and mitigating noise in HAMR. It is a statistical measure that quantifies the likelihood of the reversal of the magnetic moment for a given bit due to thermal fluctuations over a given period. It can serve as an alternative measure of transition jitter [119, 120]. Fig. 4.9a shows the switching performance of thermal ECC media, utilizing the Switching Probability Distribution (SPD) curve to characterize the transition noise. SPD is implemented to simulate the transitions between two adjacent bits with opposite magnetic polarity during the HAMR recording process. It follows a Gaussian distribution and is defined by two parameters: the switching temperature and the Full Width at Half Maximum (FWHM) of the SPD. The switching temperature represents the mean of the Gaussian curve, corresponding to the temperature of 50% switching, also known as the writing temperature. The FWHM of SPD characterizes the transition quality and is measured in term of temperature. It is imperative for a solid HAMR media to demonstrate a sharp transition, ensuring that switching occurs within a narrower temperature range, thus yielding a narrower FWHM.

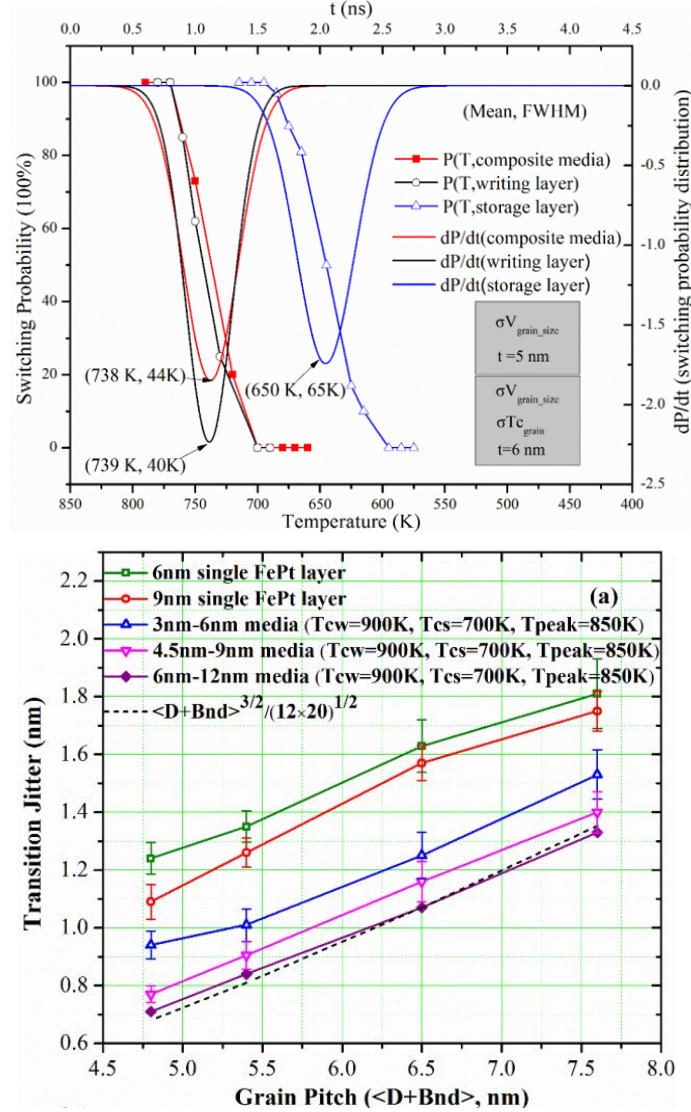


Figure 4.9: a. SPDs for conventional HAMR media and thermal ECC media [119]; b. The dependence of transition jitter on grain pitch for single-layer FePt and thermal ECC media [120].

As shown in Fig. 4.9a, the FWHM associated with thermal ECC media (red) is 42K, which exhibits a  $\sim 30\%$  improvement compared to conventional single-layer FePt (blue). Fig. 4.9b illustrates the transition jitter comparisons between thermal ECC and single-layer FePt with varying grain pitches and thicknesses, where better transition

jitter occurs with thicker thermal ECC media,  $\sim 0.3$  nm smaller than single layer FePt with the same thickness. This improvement can be attributed to higher thermal stability owing to the larger volume of grains suppressing the thermal fluctuations.

#### 4.3.5 Low-T ECC

In practice, fabricating thicker media is more challenging, involving a longer period of sputtering and annealing, which could lead to variation in media microstructure, e.g. larger grains, and increased cost. Moreover, the high operating temperature in the HAMR system may result in the deterioration of lubricant and overcoat layer, overheating of NFT and the heat-induced surface roughness of the recording medium. Thus, it is crucial to explore a new design of ECCs that presents comparable/superior recording performance in low temperature regime with reduced thickness as alternatives. Natekar and Victora proposed a novel design of thermal ECC with low writing temperature that demonstrates the same superior switching and recording performance as the high temperature thermal ECC media [121]. As shown in Table 4.2, the magnetic properties of Tc, Ms and Ku of new bilayer ECC design are reduced compared to the previous one. As a result, the peak temperature is reduced from 850 K to 650 K.

Table 4.2: Magnetic parameters in two different designs of thermal ECC media at 300 K [121].

Thermal ECC media	$T_{c,w}(\text{K})^2$	$T_{c,s}(\text{K})^3$	$M_{s,s}(\text{emu/cm}^3)^4$	$K_{u,s}(10^7 \text{ erg/cm}^3)$
High-T	900	700	922.3	4.11
Low-T	600	500	856	3.1

Fig. 4.10 compares the transition jitters between the low temperature thermal ECC and the previous design with higher writing temperature. As shown in Fig. 4.10, the transition jitters of the two configurations are identical with varying FWHM of heat spots, suggesting that potential comparable recording performance can be achieved with the new design. Compared to the old design with high writing temperature, the

<sup>2</sup>  $T_{c,w}$  denotes the Curie temperature of writing layer

<sup>3</sup>  $T_{c,s}$  denotes the Curie temperature of storage layer

<sup>4</sup>  $M_{s,s}$  denotes the magnetization of storage layer



new design lowers the writing temperature by 34% from 738 K to 486 K while still maintaining the same recording performance.

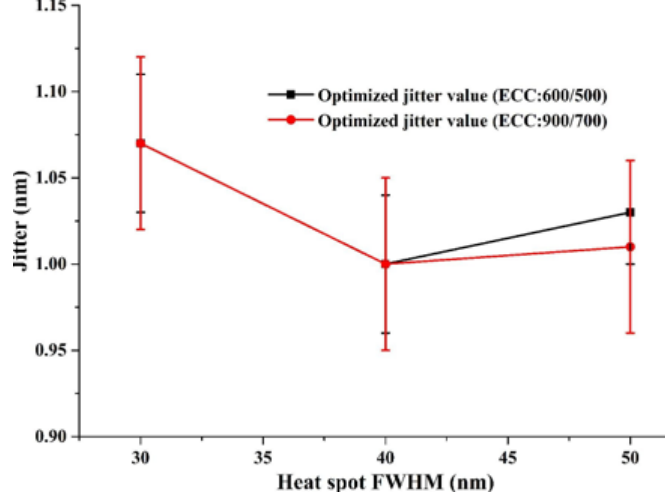


Figure 4.10: Transition jitters evaluated with high-T and low-T thermal ECC media at different grain pitches.

#### 4.3.6 Adjacent Track Erasure (ATE)

As the areal density is increased, it is expected that track pitch density continues to increase. In HAMR, a narrower track width presents a special challenge to NFT design to effectively confine the heating spot and to medium architecture to reduce cross-track heat conduction for high-quality transitions over the full track width, without compromising data integrity stored in adjacent tracks. Thus, minimizing adjacent track erasure (ATE) is crucial for HAMR to achieve high areal density.

The ATE effect in HAMR arises from poor cross-track thermal gradients, variation in magnetic properties of the recording media as well as narrow track spacing. To understand the ATE of HAMR media in-depth, ATE is assessed with two partially overlapped adjacent tracks. One track is written in a single-tone pattern (0101..) and the other track is overwritten multiple times with a pseudo-random bit sequence (PRBS). ATE is characterized with interference from the PRBS-track on the single-tone track and evaluated by parameter ‘B’ as in the equation below.

$$SNR = A + B \ln(N),$$

where N is the number of rewrites. Table 4.3 shows the ATE of three different media: conventional single-layer FePt, high writing temperature thermal ECC and low writing temperature thermal ECC [122].

Table 4.3: Adjacent track erasure evaluated with different HAMR media.

Thermal media	Thickness(nm) <sup>5</sup>	RW=15nm	RW=20nm
Single-layer FePt	[0, 9]	-0.08dB	-0.23dB
	[0, 6]	-0.30dB	-0.39dB
	[0, 7.5]	-0.27dB	-0.40dB
High-T ECC	[3, 6]	-0.19dB	-0.25dB
Low-T ECC	[3, 6]	-0.5dB	-0.46dB

Clearly, this table shows that reduced thickness of media aggravates ATE due to low thermal stability. For the same thickness of media, thermal ECC media is more susceptible to ATE compared to single layer-FePt. Yet, with the same thickness of FePt layer, ATE of high temperature ECC is improved compared to conventional single FePt layer; this is attributed to the presence of FePt stabilizing the structure despite the writing process exclusively occurring in the top layer. It has also been found that low-temperature ECC is more susceptible to ATE than high-temperature ECC. This can be attributed to the reduction of anisotropy in the storage layer and the decreased thermal gradient when lowering the T<sub>c</sub> of the medium and the peak temperature of heat spot. Although comparable single-track recording performance can be achieved by low-temperature ECC, it is also necessary to address high susceptibility to ATE in multiple track writing with other techniques, such as intergranular exchange and pulsed laser.

#### 4.3.7 Outline

The second part of this thesis, spanning from Chapters 4 to 6, focuses on optimizing magnetic parameters to reduce transition jitters in composite media for HAMR.

<sup>5</sup> Thickness for each layer is denoted in the form of [write, storage]

- Chapter 5 explores the principles of micromagnetics and simulation models, covering topics from the LLG equation to the primary contributors to the effective field in the recording system, effective renormalized media discretization, generation of Voronoi media, and the recording process in micromagnetic simulation.
- Chapter 6 is dedicated to optimizing HAMR recording performance with a novel three-layer composite media structure, characterized by transition jitters, erasure-after-write, bit error rate, and switching probability distribution. Comparative result and discussions with conventional two-layer ECC structures are provided, along with analytical analysis on switching behaviors, demonstrating the superiority of the novel media structure in terms of reducing transition noise and addressing its thermal susceptibility after writing.

## Chapter 5

# Modeling Methods of Magnetic Recording

Claim : CGS system of units is used in this chapter.

### 5.1 LLG equation

In 1935, Landau and Lifshitz first proposed a non-dissipative equation describing the precession of the magnetization  $\vec{M}$  around the effective magnetic field  $\vec{H}_{eff}$ , which is given by

$$\frac{d\vec{M}}{dt} = -\gamma\vec{M} \times \vec{H}_{eff}. \quad (5.1)$$

Later, a term of energy dissipation to the surroundings was introduced with dimensionless damping parameter  $\alpha'$  to the Landau-Lifshitz equation (LL) [123] and it became:

$$\frac{d\vec{M}}{dt} = -\gamma\vec{M} \times \vec{H}_{eff} - \frac{\gamma\alpha'}{M_s}\vec{M} \times \left(\vec{M} \times \vec{H}_{eff}\right). \quad (5.2)$$

It states the variation of  $\vec{M}$  with respect to time is equal to the net torque acting on it, following Newton's 2nd law of rotation for a rigid body.  $M_s$  denotes the saturation magnetization.  $\gamma\vec{M} \times \vec{H}_{eff}$  refers to the torque that initiates the energy-conserving precession (free precession) motion of  $\vec{M}$  around the direction of  $\vec{H}_{eff}$  with the associated angular velocity of  $\omega = \gamma H_{eff}$ . The second term accounts for damping, dissipating

energy to the surrounding via lattice vibration or spin waves, with the strength  $\alpha$  typically measured empirically. However, note that as  $\alpha' \rightarrow \infty$  in the second term,  $\frac{d\vec{M}}{dt}$  also goes to infinity ( $\rightarrow \infty$ ) instead of collapsing toward the direction of  $\vec{H}_{eff}$ , which is counter-intuitive. In 1955, T. L. Gilbert addressed this issue by proposing a modified equation for magnetization dynamics as

$$\frac{d\vec{M}}{dt} = -\gamma\vec{M} \times \vec{H}_{eff} + \alpha\vec{M} \times \frac{d\vec{M}}{dt}. \quad (5.3)$$

Here,  $\alpha$  represents the Gilbert damping constant [124]. Note that Eq. 5.3 can be recast into the same mathematical form as LL equation (Eq. 5.2) by taking the cross product of  $\vec{M}$  to both sides of the equation, which becomes

$$\frac{d\vec{M}}{dt} = -\frac{\gamma}{1+\alpha^2}\vec{M} \times \vec{H}_{eff} - \frac{\gamma\alpha}{(1+\alpha^2)M_s}\vec{M} \times (\vec{M} \times \vec{H}_{eff}). \quad (5.4)$$

This is the well-known form of the Landau-Lifshitz-Gilbert (LLG) equation, commonly used in numerical simulation of micromagnetics. Note that now when  $\alpha \rightarrow \infty$ ,  $\frac{d\vec{M}}{dt}$  reaches to its static state where  $\vec{M}$  aligns with  $\vec{H}_{eff}$  as expected. Conversely, for  $\alpha$  or  $\alpha' \rightarrow 0$ , both equations are simplified to the undamped form of LL equation without dissipation [125].

## 5.2 Numerical Implementation of LLG equation

The fourth order Runge-Kutta method (RK4) serve as the numerical solver for the LLG equation. Given an ordinary differential equation with initial conditions as follows.

$$\frac{dy}{dt} = f(t, y), y(t_0) = y_0.$$

Here  $y$  is a function of  $t$  and  $y_0$  is the initial value of  $y(t)$  evaluated at the initial time  $t_0$ . Based on RK4, the value of  $y$  at the next time step  $t_{n+1}$  is approximated by the value of  $y$  at the current time step  $t_n$  by four estimations of slopes  $k$ . Let  $h = \Delta t$  be the discretization time step.

$$y_{n+1} = y_n + \frac{1}{6}h(k_1 + 2k_2 + 2k_3 + k_4),$$

where the values of  $k_1, k_2, k_3$  and  $k_4$  are evaluated as follows.

$$k_1 = f(t_n, y_n),$$

$$k_2 = f(t_n + h/2, y_n + hk_1/2),$$

$$k_3 = f(t_n + h/2, y_n + hk_2/2),$$

$$k_4 = f(t_n + h, y_n + hk_3),$$

It is convenient to describe the precession motion of  $\vec{M}$  using spherical coordinates. Let  $\vec{m} = \frac{\vec{M}}{M_s}$  and  $\theta$  and  $\phi$  be the polar angle and the azimuthal angle respectively, then

$$m_x = \sin \theta \cos \phi,$$

$$m_y = \sin \theta \sin \phi,$$

$$m_z = \cos \theta.$$

Substituting expressions above into the LLG equation, it decomposes into two coupled ordinary differential equations between  $\theta$  and  $\phi$ , which will be solved by RK4.

$$\begin{aligned} \frac{d\theta}{dt} = & \frac{\gamma}{1 + \alpha^2} [-\sin(\phi)H_{eff,x} + \cos(\phi)H_{eff,y}] \\ & + \frac{\gamma\alpha}{1 + \alpha^2} [\cos(\theta)\cos(\phi)H_{eff,x} + \cos(\theta)\sin(\phi)H_{eff,y} - \sin(\theta)H_{eff,z}], \end{aligned} \quad (5.5)$$

$$\begin{aligned} \sin(\theta)\frac{d\phi}{dt} = & \frac{\gamma}{1 + \alpha^2} [-\cos(\theta)\cos(\phi)H_{eff,x} - \cos(\theta)\sin(\phi)H_{eff,y} + H_{eff,z}] \\ & + \frac{\gamma\alpha}{1 + \alpha^2} [-\sin(\phi)H_{eff,x} + \cos(\theta)H_{eff,y}] \end{aligned} \quad (5.6)$$

### 5.2.1 Hamiltonian of a spin system

The effective field in Eq. 5.4 is determined by

$$\vec{H}_{eff} = -\frac{\partial E}{\partial \vec{M}},$$

where E is the total Gibbs free energy of the system. The energy contribution to a spin system considered in the micromagnetic simulation, typically consists of the following terms.

$$E = E_{exchange} + E_{zeemann} + E_{anisotropy} + E_{demag} + E_{thermal}$$

Here  $E_{exchange}$  denotes the exchange energy,  $E_{zeemann}$  refers to the Zeemann energy from the write head field,  $E_{anisotropy}$  represents the crystalline anisotropy energy,  $E_{demag}$  is the magnetostatic interaction energy and  $E_{thermal}$  labels thermal agitation.

### 5.2.2 Crystalline Anisotropy Energy

Magneto-crystalline anisotropy refers to non-uniformity of magnetic behavior within the crystal structure of ferromagnetic material. In other words, there is a preferred orientation where magnetization is aligned. Magneto-crystalline anisotropy arises from spin-orbital interaction. Due to the typically nonspherical shapes and inherent symmetries of atomic orbitals, when interacting with the surroundings, the orientations and shapes of atomic orbitals are recast corresponding to the lattice symmetry. Consequently, via spin-orbit interaction, magnetization establishes its favored orientations, thereby giving rise to magnetocrystalline anisotropy characterized by certain preferred directions.

Two types of magnetocrystalline anisotropy are discussed : uniaxial and cubic. Uniaxial anisotropy is present in a hexagonal or tetragonal crystal structure, such as cobalt, or in L1<sub>0</sub> ordered alloys such as FePt and CoPt. For a system with a preferred axis  $\vec{k}$ , ignoring the higher order angular dependence,  $E_{ani}$  is approximately expressed as

$$E_{ani} = K_u V \left( 1 - (\vec{k} \cdot \vec{m})^2 \right) = K_u V \sin^2(\theta),$$

where  $\theta$  is the angle between  $\vec{k}$ -axis and the unit magnetization  $\vec{m}$ ,  $K_u$  is the energy density of anisotropy and  $V$  refers to the volume of system of interest. Depending on the sign of  $K_u$ , the preferred direction of magnetization can either be along  $\vec{k}$  axis or lie in the plane.

$$\vec{H}_{ani} = -\frac{\partial E_{ani}}{\partial \vec{m}} = \frac{2K_u}{M_s} (\vec{k} \cdot \vec{m}) \vec{k} \quad (5.7)$$

Cubic anisotropy is present in the cubic crystal and it can be expressed as

$$E_{anisotropy} = K_0 + K_1 (\alpha_1^2 \alpha_2^2 + \alpha_2^2 \alpha_3^2 + \alpha_1^2 \alpha_3^2) + \text{higher order terms}.$$

Here,  $\alpha_i$  are the direction cosines of magnetization for  $i = 1, 2$  and  $3$ .

### 5.2.3 Exchange field

Exchange interaction is a quantum mechanical effect, which can be described by the Heisenberg model with the Hamiltonian ( $H$ ) that sums over all the neighbors spins  $\vec{S}_j$  for each atom  $i$ :

$$E_{exchange} = - \sum_{i \neq j} J_{i,j} \vec{S}_i \cdot \vec{S}_j.$$

Here,  $\vec{S}_i$  and  $\vec{S}_j$  are the unit vector for spin i and j, and  $J_{i,j}$  is the exchange coupling constant between  $\vec{S}_i$  and  $\vec{S}_j$ . Assuming  $J_{i,j}$  is constant for the isotropic exchange coupling, then

$$\begin{aligned} E_{exchange} &= -J \sum_{i \neq j} \vec{S}_i \cdot \vec{S}_j = -J \sum_{i \neq j} \vec{S}_i \cdot (\vec{S}_i + \Delta \vec{S}_{i,j}) \\ &= -J \sum_{i \neq j} \vec{S}_i \cdot (\Delta \vec{S}_{i,j}) - J \sum_{i \neq j} \vec{S}_i^2. \end{aligned}$$

Since

$$\vec{S}_j^2 = (\vec{S}_i + \Delta \vec{S}_{i,j})^2 = \vec{S}_i^2 \Rightarrow \vec{S}_i \cdot \Delta \vec{S}_{i,j} = -\frac{\Delta \vec{S}_{i,j}^2}{2},$$

which is substituted into the expression of  $E_{exchange}$ . One can derive the following.

$$\begin{aligned} E_{exchange} &= J \sum_{i \neq j} \frac{\Delta \vec{S}_{i,j}^2}{2} - J \sum_{i \neq j} \vec{S}_i^2 \\ &\approx -J \sum_{i \neq j} \left[ 1 - \frac{1}{2} (\Delta \vec{r} \cdot \nabla \vec{S}(\vec{r}))^2 \right] \end{aligned}$$

Note that in the continuum approximation,  $\vec{S}_i$  and  $\vec{S}_j$  are replaced by  $\vec{S}(\vec{r})$  and  $\vec{S}(\vec{r} + \Delta \vec{r})$ , where  $\Delta \vec{r}$  is the position vector between two neighboring spins, then  $\Delta \vec{S}_{i,j}$  can be approximated by  $\Delta \vec{r} \cdot \nabla \vec{S}(\vec{r})$ . One can rewrite  $E_{exchange}$  as

$$E_{exchange} = \frac{1}{2} J S^2 \sum_{i \neq j} [\Delta \vec{r} \cdot \nabla \vec{m}(r)] = \frac{J S^2 a^2}{2} [(\nabla m_x)^2 + (\nabla m_y)^2 + (\nabla m_z)^2].$$

Consider a simple cubic with lattice constant  $a$  and define exchange stiffness constant as  $A_{ex} = J S^2 / a$  and volume of the unit cell be  $V = a^3$ . Then

$$E_{exchange} / V = \frac{A_{ex}}{M_s^2} (|\nabla_x \vec{M}|^2 + |\nabla_y \vec{M}|^2 + |\nabla_z \vec{M}|^2).$$

Thus, one can derive that exchange field  $\vec{H}_{exchange}$  is

$$\begin{aligned} \vec{H}_{exchange} &= \frac{\partial E_{exchange}}{\partial \vec{M}} \\ &= \frac{A_{ex}}{M_s^2} (\nabla_x^2 \vec{M} + \nabla_y^2 \vec{M} + \nabla_z^2 \vec{M}) \\ &= -\frac{2A_{ex}}{M_s a^2} \sum_{n,n} \vec{m}, \end{aligned}$$

where  $\vec{m}$  is the unit vector of  $\vec{M}$  and "n,n" denotes nearest neighbors.



### 5.2.4 Magnetostatic Energy

The magneto-static interaction refers to a long-range dipole-dipole interaction between magnetic moments within the system, defining the alignment and orientation of magnetic moments within a material and yielding various magnetic phenomena such as magnetic ordering, domain formation, and magnetic domain wall motion. Hence, accurate and efficient inclusion of the magneto-static interaction into the LLG equation is essential to the scalability of numerical micromagnetic simulation, especially for the systems with hundreds of thousands magnetic moments. The magneto-static interaction is governed by the Maxwell equations :

$$\nabla \cdot \vec{B} = 0$$

$$\nabla \times \vec{H}_{mag} = 0,$$

where the magnetic flux density  $\vec{B}$  and the magnetostatic field  $\vec{H}_{mag}$  are related by  $\vec{B} = \vec{H}_{mag} + 4\pi\vec{M}$  in CGS unit. By solving the Maxwell equations above, the total magnetostatic field at position  $\vec{r}$  is given by

$$\begin{aligned} \vec{H}_{mag}(\vec{r}) = & -\frac{1}{4\pi} \int_{volume} \frac{\nabla' \cdot \vec{M}(\vec{r}')(\vec{r} - \vec{r}')}{|\vec{r} - \vec{r}'|^3} dV' + \\ & \frac{1}{4\pi} \int_{surface} \frac{\vec{n} \cdot \vec{M}(\vec{r}')(\vec{r} - \vec{r}')}{|\vec{r} - \vec{r}'|^3} d\vec{S}'. \end{aligned} \quad (5.8)$$

where  $\vec{H}_{mag}$  can be separated into the contribution from the volume poles,  $\nabla \cdot \vec{M}(\vec{r})$  and the surface poles,  $\vec{n} \cdot \vec{M}(\vec{r}')$ . Note that it is numerically expensive to obtain  $\vec{H}_{mag}$  by Eq. 5.8 directly and the time complexity scale as  $N^2$  where  $N$  is the number of dipoles in the system.

Instead, rearranging Eq. 5.8 to the form of Eq. 5.9 allows the adoption of a Fast Fourier Transform (FFT) algorithm to determine  $\vec{H}_{mag}$ , reducing computational time to  $N \ln N$ .

$$\vec{H}_{mag} = - \int_{volume} \nabla \nabla' \left( \frac{1}{|\vec{r} - \vec{r}'|} \right) \cdot \vec{M}(\vec{r}') dV' = - \int_{volume} \overleftrightarrow{N}(\vec{r} - \vec{r}') \cdot \vec{M}(\vec{r}') dV', \quad (5.9)$$

where  $\overleftrightarrow{N}$  is the Green's function, given by

$$\overleftrightarrow{N} = \nabla \nabla' \left( \frac{1}{|\vec{r} - \vec{r}'|} \right).$$

$\overleftrightarrow{N}$  can be expressed in the following form as well.

$$\overleftrightarrow{N} = \begin{bmatrix} N_{xx} & N_{xy} & N_{xz} \\ N_{yx} & N_{yy} & N_{yz} \\ N_{zx} & N_{zy} & N_{zz} \end{bmatrix} \quad (5.10)$$

A detailed description of FFT can be found in Ref. [126]. In addition to FFT, parallel-computing in graphics processing unit (GPU) is applied to further improve the computational efficiency. Nonetheless, even with the FFT and parallel computing in GPU, the calculation of  $\vec{H}_{mag}$  remains the most time-consuming part in the simulation.

### 5.2.5 Thermal agitation field

Accurately introducing thermal agitation is crucial for characterizing micromagnetic dynamics, particularly in HAMR where the switching occurs near Curie temperature. At this point, the contributions to writing from other fields are practically zero except the write head field and thermal field. Thus, it is crucial to investigate the impact of thermal fluctuations on magnetization dynamic for high recording quality. Based on Brown's work [127], thermal fluctuations and the agitation effect are characterized by a Gaussian thermal field  $\vec{H}_{th}$ . At a given temperature  $T$  and time  $t$ , thermal field  $\vec{H}_{th}$  is given as:

$$\vec{H}_{th}(t) = \vec{h}(t) \sqrt{\frac{2\alpha k_B T}{\gamma M_s \Delta V \Delta t}},$$

where  $\vec{h}(t)$  is a white noise vector generated by a normal distribution with a mean of zero,  $k_B$  represents the Boltzmann constant,  $\Delta V$  and  $\Delta t$  are the discretization volume and time step used to the LLG solver. The  $\vec{h}(t)$  is subject to the following statistical requirements :

$$\langle h_{i,m}(t) \rangle = 0, \langle h_{i,m}(t_1) h_{j,n}(t_2) \rangle = \delta_{i,j} \delta_{m,n} \delta(t_1 - t_2). \quad (5.11)$$

Here,  $i$  and  $j$  refer to the components of the Cartesian coordinate.  $m, n$  refer to the indices of the discretized volume used in the LLG solver. Eq. 5.11 suggests that there is no correlation between any two thermal fields component-wise and position-wise. Note that the validity of Eq. 5.11 relies on the sufficiently small time discretization to justify the linearization of the stochastic LLG equation.

### 5.2.6 Zeeman Energy

Zeeman energy refers to the potential energy of magnetization under an external applied field  $\vec{H}_{appl}(\vec{r})$ .

$$E_{Zeeman} = - \int \vec{M}(\vec{r}) \cdot \vec{H}_{appl}(\vec{r}) dV$$

### 5.3 Renormalization method for HAMR

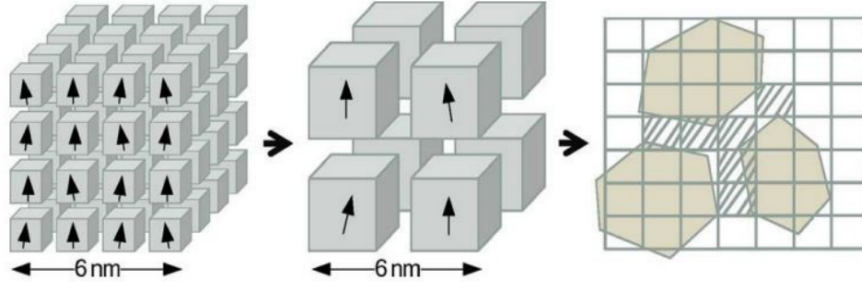


Figure 5.1: An illustration of the atomistic discretized (left) and coarse-grained (middle) 6-nm spin blocks with 0.3 nm and 1.5 nm-renormalized cells, respectively, along with the mapping from the renormalized cell to Voronoi media (right).

In LLG simulations, accurately representing the dynamics of magnetic characteristics within a single grain relies on the judicious discretization of space and time. While atomistic-scale discretization, where each unit cell contains only one spin, can provide the most precise depiction of spin dynamics within a grain consisting of thousands of atoms, it becomes computationally impractical for handling large systems with hundreds of grains, especially when magnetostatic interactions are involved. Alternatively, grain-size discretization can offer a solid approximation for multi-grain systems in PMR at room temperature. However, this approach inevitably neglect the contribution of high-frequency modes on the spin dynamics within the grain size length scale, which is crucial for the accuracy of HAMR simulations near the Curie temperature.

Victora and Huang [128] addressed this resolution issue by proposing a renormalized-cell method in LLG simulations. As shown in Fig. 5.1, a coarse grid ( $\sim 1\text{-}2$  nm) is used to discretize the a grain, instead of an atomic-size grid, to ensure computational

efficiency in handling multi-grain systems. Near  $T_c$ , it can be well-justified because the correlation length of spin approaches infinity based on renormalization theory. At the same time, to retrieve temperature dependent spin dynamics for short length scales, a new set of magnetic properties are determined to ensure the spin block discretized by atomic size ( $\sim 0.3$  nm) yields the same macroscopic values of magnetic properties on average as the coarse-grained spin block does.

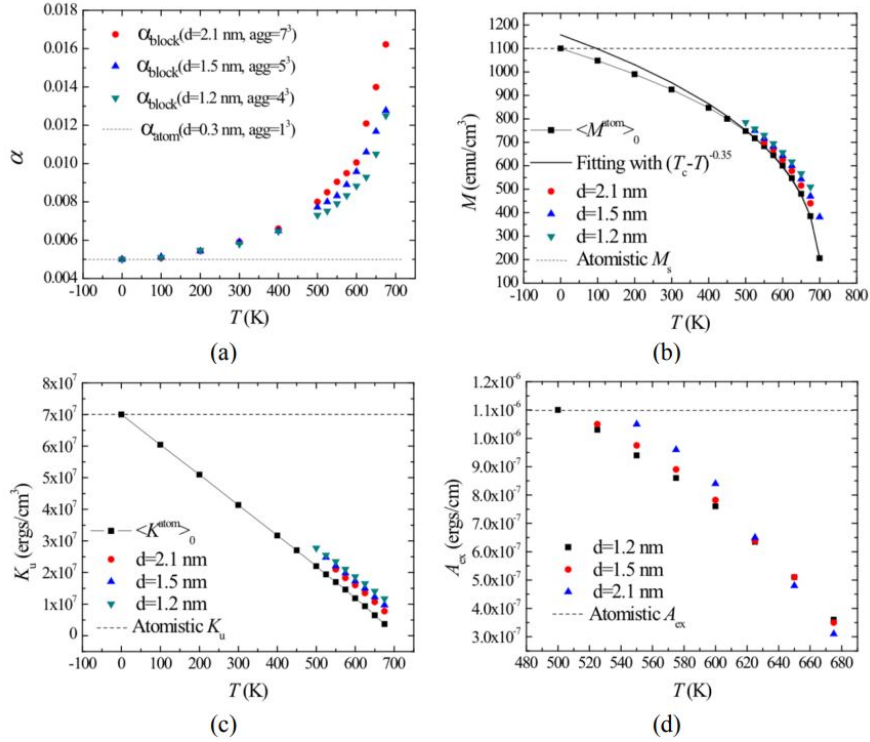


Figure 5.2: The renormalized parameters determined with different grid sizes [128].

Detailed description of this method can be found in Ref. [128]. Magnetization,  $M_{\text{renorm}}$ , anisotropy  $K_{\text{renorm}}$  and exchange stiffness  $A_{\text{ex,renorm}}$  are obtained base on the following equations by trial and error methods.

$$\langle M_{\text{atom}} \rangle = \langle M_{\text{renorm}}(M_{\text{renorm}}, K_{\text{renorm}}, A_{\text{renorm}}) \rangle$$

$$\langle H_K^{\text{atom}} \rangle = \langle H_K^{\text{renorm}}(M_{\text{renorm}}, K_{\text{renorm}}, A_{\text{renorm}}) \rangle$$

$$\langle \delta H_K^{\text{atom}} \rangle = \langle \delta H_K^{\text{renorm}}(M_{\text{renorm}}, K_{\text{renorm}}, A_{\text{renorm}}) \rangle$$

The renormalized damping constant  $\alpha_{renorm}$  is determined by the Green-Kubo method developed by Feng and Visscher [129]:

$$\frac{\alpha_{renorm}}{1 + \alpha_{renorm}^2} = \frac{-M_i \langle \sum_i^{block} \frac{d\vec{M}_i}{dt} \cdot \vec{M}_s \times (\vec{M}_i \times \vec{H}_i^{eff}) \rangle_t}{\gamma \langle \sum_i^{block} (\vec{M}_i \times (\vec{M}_i \times \vec{H}_i^{eff}))^2 \rangle_t},$$

where the summation is performed over each atomic unit cell and  $\langle \cdots \rangle_t$  denotes the time average.

Fig. 5.2(a)-(d) shows the renormalized parameter determined for isotropic L1<sub>0</sub> FePt with different sizes of renormalized cell [128]. Here, d refers to the size of renormalized cell. As d increases, the value of renormalized parameters approaches to the macroscopic values. Note that all renormalized magnetic parameters are temperature and size dependent rather than the constant values for atomistic-scale parameters.

## 5.4 Voronoi Media

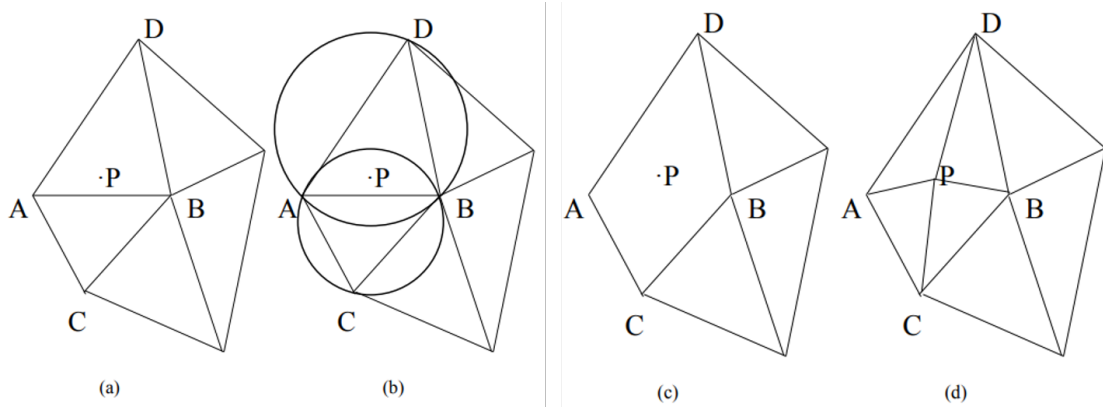


Figure 5.3: An illustration of Bowyer-Watson algorithm [132].

Voronoi media is usually used for capturing the characteristics of geometric variation in fabricating granular magnetic media. Voronoi tessellation is a method to partition a plane into regions based on the proximity to a set of points called seeds or generators. Given a set  $P$  of  $n$  points :  $P = \{p_1, p_2, \dots, p_n\}$  in a plane, the Voronoi cell  $V(p_i)$  associated

with each point  $p_i$  is defined as a region that contains all the points  $x$  in the plane such that the distance between  $x$  and  $p_i$  is less than or equal to the distance between  $x$  and any other point in  $P$  [130].

$$V(p_i) = \{x : d(x, p_i) \leq d(x, p_j), \forall p_j \in P\}.$$

The Bowyer–Watson algorithm is typically used to realize the Voronoi diagram. The algorithm iteratively adds points to the triangulation mesh while maintaining the Delaunay property, which ensures that no point is inside the circumcircle of any triangle in the mesh [130, 131]. The algorithm is illustrated by Fig. 5.3. Start with an initial triangulation covering all the points. For each new point to be added: a. Identify the triangle in the existing mesh that contains the new point ( $\triangle ABD$ ). b. Remove this triangle and all other triangles that share an edge with it ( $\triangle ABD$  and  $\triangle ABC$ ). c. Re-triangulate the resulting cavity by connecting the new point to the vertices of the removed triangles. d. Update the triangulation to maintain the Delaunay property. Then the each vertex of the Voronoi diagram is the circumcenter of Delaunay triangles. The Voronoi diagram is completed by connecting all the adjacent vertices. Note that the time complexity of this algorithm is  $O(n^2)$ , where  $n$  is the number of seeds. The details of Voronoi media with grain boundaries can be found in Ref. [130, 132].

## 5.5 Recording Process

The recording simulation involves applying a write head field whose direction is dictated by the designated recording pattern to a Voronoi media under a moving heat spot. The temperature distribution on the recording media is approximated by a 2-D Gaussian thermal distribution, assuming uniform temperature along the thickness direction, given as:

$$T(x, y, t) = 300 + (T_{peak} - 300) \exp \left( \frac{-(x - x_0 - vt)^2 - (y - y_0)^2}{2\sigma^2} \right).$$

This 2-D moving temperature distribution  $T(x, y, t)$  describes a Gaussian thermal profile at any given time  $t$ , with the peak temperature  $T_{peak}$  and standard derivation  $\sigma$  defined as  $\sigma = \text{FWHM}/(2\sqrt{2\ln 2})$ , moving at velocity  $v$  along down-track direction  $x$  from the starting position  $(x_0, y_0)$ . The cross-track direction is denoted by  $y$ , with room temperature assumed to be 300 K. The transition position is approximately determined

by the condition  $H_{eff} = H_{appl}$ , which can be further reduced to  $H_k \sim H_{appl}$  due to the dominant contribution of anisotropy field to the total effective field. During the recording process, the Gaussian thermal profile heats a circular region on the medium within which the magnetization can be switched following the condition above. Thus, for the adjacent bit with opposite polarity, the resulting recording pattern is in the crescent-moon shape.

Fig. 5.4 demonstrates that the transition position closely depends on the down-track thermal gradient generated by a strong thermal sink [133]. As shown in Fig. 5.4, a strong heat sink leads to a larger down-track thermal gradient as the strong vertical heat conduction substantially confines the in-plane heat flow, resulting in smaller transition jitters, i.e. less variation in the transition position.

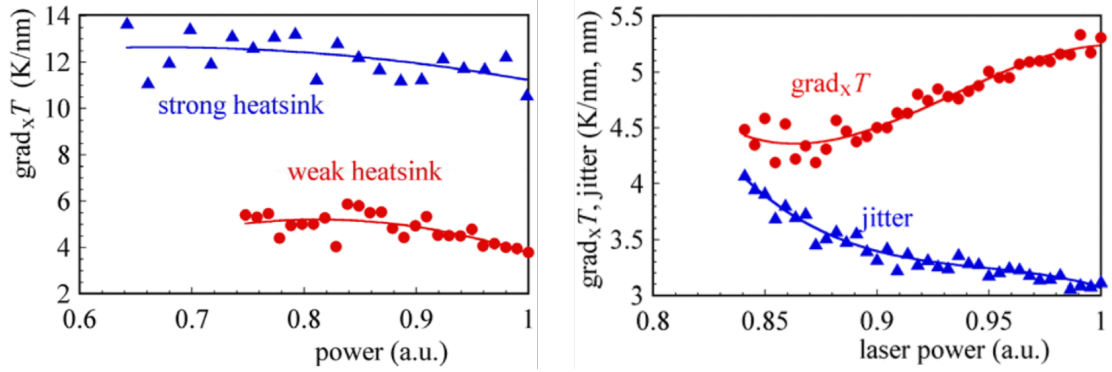


Figure 5.4: The dependence of down-track thermal gradient on heatsink (left) and the response of transition jitters to down-track thermal gradient (right) [133].

## 5.6 Readback Process

The read head consists of shields and a magnetoresistive (MR) component such as tunneling magnetoresistance (TMR) stacks positioned in between. MR elements are responsible for sensing the magnetic fields emitted from the media while shields serve to block the interference from the background. During the readback process, the read head detects the magnetic field generated by recorded magnetization patterns, inducing a readback voltage that mirrors the pattern of the media, known as the playback signal.

Ideally, the playback signal should result from the interaction between media magnetic field and magnetization from a read head. However, accurate generation of the media field is practically challenging.

Fortunately, the reciprocity principal reveals that interactions between magnetic recording medium and read/write heads are reciprocal in nature. Thus, the playback can be determined by convoluting the magnetization of media with the read head field which is more straightforward to generate [134]. Exerting a source of a unit field and boundary conditions of zero potential in the shields and at the bottom of the media, the read head field is determined by solving 3D Poisson's equation. Based on the reciprocity principal, the generalized three-dimensional form for the playback signal  $V(x)$  is given by

$$V(x) = c \int_{medium} \vec{h}(\vec{r}' + x) \cdot \frac{d\vec{M}(\vec{r}')}{dz'} d^3r',$$

where  $\vec{h}(\vec{r})$  refers to the normalized read head field,  $\vec{M}(\vec{r})$  is the magnetization of media and  $\frac{d\vec{M}(\vec{r}')}{dz'}$  represents the associated surface charge and  $c$  is a unit-dependent constant proportionality.



## Chapter 6

# Reducing Transition Jitter with Composite Media for HAMR

### 6.1 Introduction

In the era of big data, it is more paramount than ever to accommodate the burgeoning demand for very high capacity data storage and access. Among all the magnetic storage technologies, Heat-assisted magnetic recording (HAMR) stands out as one of the most promising and evolutionary candidates to succeed conventional perpendicular magnetic recording (PMR) with its potential to achieve areal density above 10 Tb/in<sup>2</sup> [135, 136, 137]. HAMR capitalizes on the fact that near the Curie temperature, magnetic properties of granular media become vanishingly small and yet return to their thermally and magnetically stable values at room temperature. Thus, writing process can be achieved with smaller switching fields, higher anisotropy and smaller volume of grains, leading to a higher areal density (AD) [138].

To mitigate noise induced by the  $T_c$  variance of HAMR media, two-layer thermal exchange coupled composite (ECC) media was first proposed by Liu, et.al [142]. This structure introduces a moderately softer writing layer with a higher  $T_c$  than the FePt-storage layer, effectively decoupling the recording process from long-term storage process, thus enabling the removal or reduction of the dependence on  $T_c$  variance of the storage layer and improving the recording efficiency and quality [142, 143]. However, the conventional two-layer ECC structure encounters adjacent track-erasure issue

at reduced operating temperature owing to the soft material used in the writing layer [145]. Despite improvements in the sustainability of media structure, thermal stability is compromised due to a lower  $K_u$  at the expense of the reduced writing temperature.

In this section, HAMR performance is evaluated with three-layer ECC which incorporates a middle layer between the superparamagnetic writing layer and the storage layer. By inserting a middle layer, 3ly-ECCs exhibit higher tunability with additional magnetic parameters introduced and therefore hold the promise to further optimize the thermal noise and stabilize the structure after writing. The 3ly-ECCs are first optimized based on transition jitter, followed by an analytical analysis of the switching behaviors to identify the switching mechanism for improved transition jitters. Erasure-after-write effect as a preliminary evaluation of ATE along with BER are determined between optimized 2ly-ECC and 3ly-ECC to further gauge HAMR quality. Lastly, switching probability distribution (SPD) calculations are included as supplemental evaluation technique for comprehensive analysis. Note that the effect of intergranular exchange coupling on HAMR performance is thoroughly assessed across all noise measures for all 3ly-ECC and 2ly-ECC configurations.

## 6.2 Methods

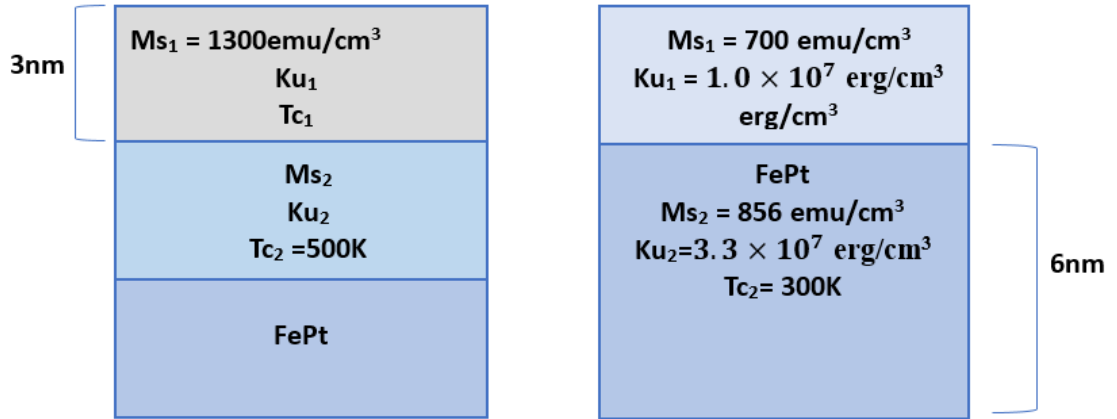


Figure 6.1: Sketches of the proposed 3ly-ECC and 2ly-ECC [143] structure with total thickness of 9nm. The magnetic properties listed are evaluated at 300 K.

In order to evaluate the recording performance, the spin dynamics of the ECC media is first analyzed with micromagnetic simulation described by the Landau-Lifshitz-Gilbert (LLG) equation as in 6.1, where applied external field, magnetic-crystalline anisotropy field, exchange field, dipole interaction field and thermal fluctuation field are included as the total effective field  $H_{eff}$ . The LLG equation is solved with the Runge-Kutta fourth-order method with time step (dt) set to be  $10^{-14}$ s. The convergence for the given time step has been confirmed within 1% for all the simulations.

$$\frac{d\vec{M}}{dt} = -\frac{\gamma}{1+\alpha^2}\vec{M} \times \vec{H}_{eff} - \frac{\gamma\alpha}{(1+\alpha^2)M_s}\vec{M} \times (\vec{M} \times \vec{H}_{eff}). \quad (6.1)$$

The micromagnetic simulation is performed on  $384 \text{ nm} \times 48 \text{ nm} \times 9 \text{ nm}$  ECC media that includes 884 Voronoi grains with an average grain diameter of 4.5 nm (5.5 nm grain pitch) and grain size distribution (GSD) of 20%. 3ly-ECC is achieved by inserting a middle layer that separates the superparamagnetic writing layer and storage layer (FePt), each layer being 3 nm thick with 9 nm in total. Based on the 2ly-ECC counterpart [143], the magnetization, anisotropy and the Curie temperature of FePt-storage layer in 3ly-ECC is set to be 856 emu/cm<sup>3</sup>,  $3.3 \times 10^7$  erg/cm<sup>3</sup> and 500 K respectively. The magnetizations, anisotropies and Curie temperatures of a superparamagnetic layer and a middle layer are varied to optimize the transition jitter while maintaining its writing temperature within 2% of that in 2ly-ECC in order to achieve a fair comparison of the recording performance between 2ly-ECC and 3ly-ECCs. Otherwise, a high writing temperature narrows the writing width, but usually improves the thermal gradient. For computational efficiency, a coarse-grid unit cube of 1.5 nm is used in micromagnetic simulation to replace the atomistic spin discretization ( $\sim 0.3$  nm). The renormalized magnetic properties for superparamagnetic writing layer and middle layer can be scaled based on those of FePt layer following Ref.[141, 153], assuming that the varying of magnetic properties (Ms, Ku and Tc) can be achievable by doping in L1<sub>0</sub> FePt. For instance, doping Ni to L1<sub>0</sub> FePt can reduce its Tc to 500 K.

A switching calculation is first used to determine the writing temperature of ECC media, which is defined as 50% switching at room temperature. As an analogy to the writing process, the default setting in all simulations is a constant head field of 8 KOe with canting angle of 22.5° applying to the thickness direction and a peak temperature of 650 K being consistent with Ref.[143]. Analogous to the moving recording head, the

media temperature is assumed to decrease linearly with a constant cooling rate of 400 K/ns. Note that this cooling rate is a projected future value, though it is slightly higher than the practical value (300 K/ns) currently in use. The temperature in different layers is assumed to be uniform and the same. To simulate the realistic HAMR media, a reasonable  $\sigma Ku$  of 15% and  $\sigma Tc$  of 3% are included in all layers of ECC media.

In the recording simulation, a 2D Gaussian thermal profile with 40 nm isotropic FWHM, 650 K peak temperature and head velocity of 20 m/s is used as a default setting. Transition jitter is calculated using a single tone recording pattern with 20 nm bit length (BL). The track widths for all the media are observed to be very similar because the writing temperatures are controlled within 2% for all the media. The read head geometry is assumed to be as follows: magnetic fly height of 6 nm, the reader width of 20 nm, and the shield-to-shield spacing (SSS) of 22 nm.

Transition jitter is determined by the resulting playback signals generated with read head geometry based on the reciprocity principle [154]. The read head potential is calculated by the finite difference method. The zero-crossing points in the corresponding playback signals are defined as the transition positions between two adjacent bits with different polarity. In total, 544 zero-crossings over 32 different media are used to reduce statistical noise.

Bit error rate is also evaluated to characterize the recording performance of ECC media. A Viterbi algorithm [155] is used to decode the recording pattern of a pseudo-random binary sequence (PRBS). To achieve sufficient statistics, 160 playback signals with 4960 bits in total are generated over 32 different media such that each of them is written 5 times at shifting starting points. 50% of playback signals are used as training in Viterbi algorithm and the rest of 50% is used to calculate BER.

Erase-after-write (EAW) effect is determined as a preliminary estimation of adjacent track interference issue. The number of grains erased after recording during cooling process is used to as a measure of EAW. The switching status of each grain is evaluated at two moments: after writing and after cooling [156]. “After writing” is defined as the time step right before the applied field starts to record the next bit. This moment occurs when the center of heat spot moves twice the BL from the left edge of the written bit. “After cooling” is defined as the time step after the written bit is cooled down to the room temperature where the switching status has reached to stationary state. EAW

calculation is performed on the optimized 3ly-ECCs and compared to that of 2ly-ECC.

## 6.3 Results and Discussions

### 6.3.1 Transition Jitter

By inserting a middle layer between the writing layer and storage layer, more degrees of freedom in the 3ly-ECC allow the Zeeman effect and the gradient of effective magnetic field, in particular, anisotropy field gradient to be decoupled for a potential better switching performance. The proposed writing layer in the 3ly-ECC is designed to take full advantage of Zeeman energy while reducing the anisotropy field by a substantial magnetization  $M_s$  and a small anisotropy  $K_u$  for easy and rapid switching.

This adversely lowers the writing temperature of the whole structure which can potentially introduce dependence on  $T_c$  variation in the FePt layer and thus downgrade the writing efficiency. To bring back the writing temperature above that of pure FePt layer and make it comparable to the two-layer counterpart, a substantial anisotropy  $K_{u2}$  is introduced in the middle layer in addition to a smaller  $M_{s2}$  (than FePt). This enables switching to be controlled by the anisotropy field of the middle layer, which has a very large gradient. The magnetization of top layer ( $M_{s1}$ ) is set to be  $1300 \text{ emu/cm}^3$ , which is a large value compared to commercial recording media.

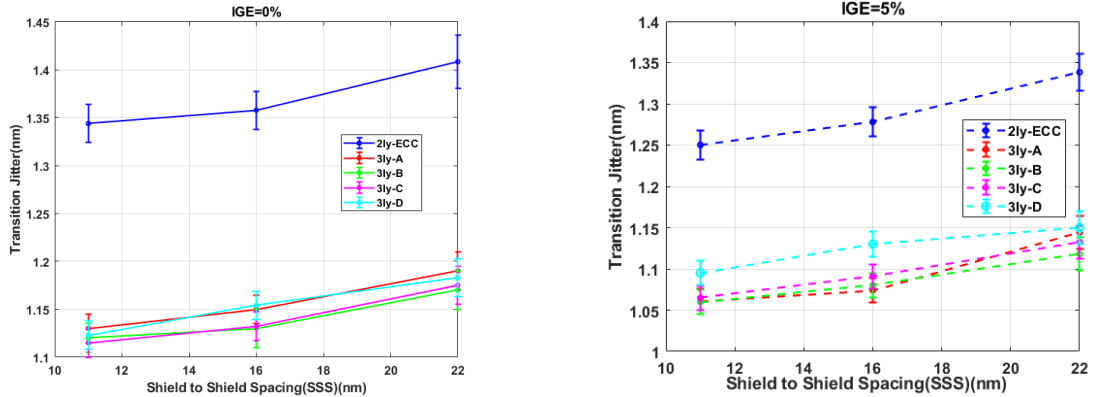


Figure 6.2: (a) Transition jitters comparison between 2ly-ECC and 3ly-ECCs at different SSSs in absence of IGE. (b) Transition jitters comparison between 2ly-ECC and 3ly-ECCs at different SSSs in the presence of 5% IGE.

$T_{c2}$  of middle layer is set to be 500 K, which is the same as that of the FePt layer used in 2ly-ECC in [143], and the upper bound for  $K_{u2}$  is subject to that of FePt, which is  $3.3 \times 10^7$  emu/cm<sup>3</sup>. The parameters to be tuned are Curie temperature of top layer,  $T_{c1}$ ,  $M_{s2}$ , and anisotropy of top and middle layer,  $K_{u1}$  and  $K_{u2}$ . Those parameters are chosen to be tuned within the range as given in Table 6.1-6.3 such that the resulting writing temperatures are within 2% of that of 2ly-ECC (495 K). Further tuning of the parameters either produces invalid writing temperatures or invalid anisotropies. The configuration of 2ly-ECC refers to [143]. The resulting jitters is determined by the associated playback signals, which can be computed by summing over the cross correlation of potential gradient along thickness direction and the associated magnetization of each layer.

Note that the writing temperature refers to the temperature of 50% switching of the entire medium structure and is determined by a switching probability distribution curve. Although the overall switching temperature (495 K) is close to the  $T_{c3}$  of the FePt (500 K), the switching of the middle and FePt layer actually occurs at a lower temperature owing to the lagging response of domain wall propagation, which takes time to establish and propagates vertically. Thus, no artifact near  $T_{c3}$  would impact the simulation results. Unless mentioned otherwise, the intergranular exchange for each layer is set to be 0% and interlayer exchange is set to be 100% of the bulk renormalized exchange value.

Table 6.1, 6.2 and 6.3 show transition jitters for different 3ly-configurations. The cross signs in these tables indicate invalid configurations whose writing temperatures fall outside the acceptable range. Even though the overlapping of jitter for different configurations could pose uncertainty regarding the exact local minimum configurations, considering the  $\sim 2\%$  error associated with jitters, the four local minima for jitters of 1.20nm as shown in Table 6.1, 6.2 and 6.3 can be determined with confidence. Table 6.4 summarizes the four configurations of 3ly-ECC with optimized interlayer exchange between 100% and 80%, where  $M_{s1} = 1300$  emu/cm<sup>3</sup> and  $T_{c2} = 500$ K. Each 3ly-ECC structure in Table 6.4 exhibits reasonable thermal stability with  $K_u V / k_B T > 70$  evaluated at  $T = 300$  K, where  $V$  is the grain volume of the middle and FePt layer with a diameter of 4.5 nm. Note that thermal stability is evaluated for the storage layer and therefore, only the bottom two layers are included.

Fig. 6.2 and Table 6.5 compares jitter between the four proposed 3ly-ECCs and the 2ly-ECC in the presence/absence intergranular exchange (IGE) at different shield to shield spacings (SSS). Note that although the variation of SSSs will change MT10 and reader SNR, all the comparisons are achieved with consistent head field and geometry. As shown in Fig. 6.2, in general, smaller SSS results in better jitter due to a higher head resolution. The introduction of 5% IGE helps reduce jitter by  $\sim 3\%$  to  $5\%$  which is expected as the IGE serves to make local grains switch collectively, thus mitigating the thermal fluctuations. Compared to the 2ly-ECC, 3ly-ECCs effectively reduce transition jitters by  $\sim 17\%$  in the presence of 5% IGE and  $\sim 15\%$  in the absence of IGE respectively at  $SSS = 22$  nm. Note that four 3ly-configurations show comparable jitter in the presence/ absence of IGE with 3ly-A and 3ly-D  $\sim 3\%$  worse. The marginal improvement in jitters by reducing SSS from 16nm to 11nm is  $\sim 2\%$ , compared to  $\sim 4.5\%$  for the case from 22nm to 16nm. This suggests that the jitters associated with media characteristics such as GSD dominates. Overall, the transition noises associated with the four proposed 3ly-ECCs are approximately the same with/without IGE considering the associated error bars.

Table 6.1: Summary of Transition Jitter for  $T_{c1} = 560$  K and 0% IGE.

$Ku_2$ ( $10^7 \text{erg/cm}^3$ )	$Ms_2=300 \text{emu/cm}^3$ $Ku_1(10^7 \text{erg/cm}^3)$			$Ms_2=350 \text{emu/cm}^3$ $Ku_1(10^7 \text{erg/cm}^3)$			$Ms_2=400 \text{emu/cm}^3$ $Ku_1(10^7 \text{erg/cm}^3)$		
	1.3	1.5	1.8	1.3	1.5	1.8	1.3	1.5	1.8
2.7	1.25	1.28	1.34	$\times$	$\times$	1.34	$\times$	$\times$	1.31
3.0	1.34	1.28	1.24	1.24	1.24	1.29	$\times$	1.33	1.30
3.3	1.24	1.26	1.21	1.26	1.21	1.24	1.27	1.27	1.28

Table 6.2: Summary of Transition Jitter for  $T_{c1} = 600$  K and 0% IGE. Note that All the Associated Errors are within 3%.

$Ku_2$	$Ms_2=300 \text{emu/cm}^3$ $Ku_1(10^7 \text{erg/cm}^3)$	$Ms_2=350 \text{emu/cm}^3$ $Ku_1(10^7 \text{erg/cm}^3)$	$Ms_2=400 \text{emu/cm}^3$ $Ku_1(10^7 \text{erg/cm}^3)$
--------	--	--	--

$(10^7 \text{erg/cm}^3)$	1.1	1.3	1.5	1.1	1.3	1.5	1.1	1.3	1.5
2.7	×	1.25	1.31	×	1.33	1.29	×	1.34	1.32
3.0	1.24	1.35	1.27	1.29	1.32	1.30	×	1.28	1.26
3.3	1.26	1.28	1.23	1.21	1.27	1.32	×	1.31	1.21

Table 6.3: Summary of Transition Jitter for  $T_{c1} = 630$  K and 0% IGE. Note that All the Associated Errors are within 3%.

$\text{Ku}_2$ $(10^7 \text{erg/cm}^3)$	$\text{Ms}_2=300 \text{emu/cm}^3$ $\text{Ku}_1(10^7 \text{erg/cm}^3)$			$\text{Ms}_2=350 \text{emu/cm}^3$ $\text{Ku}_1(10^7 \text{erg/cm}^3)$			$\text{Ms}_2=400 \text{emu/cm}^3$ $\text{Ku}_1(10^7 \text{erg/cm}^3)$		
	1.1	1.3	1.5	1.1	1.3	1.5	1.1	1.3	1.5
2.7	×	1.29	1.38	×	1.38	1.36	×	1.34	1.32
3.0	1.28	1.31	1.34	1.29	1.25	1.34	×	1.28	1.26
3.3	1.25	1.26	1.27	1.30	1.24	1.28	×	1.28	1.26

Table 6.4: Summary of the Optimized 3ly-ECC's Configurations.

ECC	$T_{c1}(\text{K})$	$\text{Ms}_2$ (emu/cm <sup>3</sup> )	$\text{Ku}_1$ ( $10^7 \text{erg/cm}^3$ )	$\text{Ku}_2$ ( $10^7 \text{erg/cm}^3$ )	$\text{Aex}_{1,2}$	$\text{Aex}_{2,3}$
3ly-A	600	350	1.1	3.3	0.9	0.9
3ly-B	600	400	1.5	3.3	1.0	0.8
3ly-C	560	350	1.5	3.3	0.9	1.0
3ly-D	560	300	1.8	3.3	1.0	1.0

### Analytical Model

To comprehend the improvement in transition jitters in the 3ly-ECCs, a 3-spin model is used to quantify the energy barrier between different switching states of the middle and FePt layers [157]. Owing to the substantial Ms and small Ku in the top layer, the switching of middle and FePt are supposed to occur when the top layer has already reached the energy minimum. Hence, the 3-spin model can be reduced to a 2-spin model



assuming the top layer is in its energetically stationary state. For simplicity, a uniform external magnetic field  $H$  is applied along the perpendicular easy axis ( $-z$ ). Assuming that the switching occurs near the Curie temperature,  $K(T)$ ,  $M(T)$  and  $J_{ex}(T)$  can be approximately with  $K_0(1 - T/T_c)$ ,  $M_0(1 - T/T_c)^{1/3}$  and  $J_0(1 - T/T_c)^{1/3}$ , respectively based on mean field theory. Note that the exponent of temperature dependence for exchange energy  $J(T)$  is assumed to follow the magnetization  $M(T)$  as explained in [158] and numerically confirmed in [159].  $J_0$ ,  $K_0$  and  $M_0$  denote the zero-temperature values respectively.

Table 6.5: Summary of Transition Jitters of 3LYs and 2LY-ECC at Different Shield to Shield Spacing with IGE = 0 and 5%.

ECC	SSS(nm)					
	22	16	11	22	16	11
	IGE=0%			IGE=5%		
2ly	1.41	1.36	1.35	1.34	1.28	1.25
3ly-A	1.20	1.15	1.13	1.14	1.07	1.06
3ly-B	1.17	1.14	1.12	1.12	1.08	1.06
3ly-C	1.18	1.13	1.12	1.13	1.09	1.07
3ly-D	1.18	1.15	1.12	1.15	1.13	1.10

The total energy of the 3-layer system is given as in equation 6.2, where  $J_{ex,1,2}(T)$  and  $J_{ex,2,3}(T)$  are the exchange energy between the top and middle layer and middle and FePt layer respectively. Subscripts 2 and 3 denote the middle and FePt layer, respectively.  $\theta_2$  and  $\theta_3$  are the switching angles between the anisotropy axis and magnetization for the middle and FePt layers, both with an initial angle of zero.  $V$  denotes the volume of each layer.  $\theta_1$  is assumed to be  $\pi$ , aligning with the applied field.

$$\begin{aligned}
E(T) = & -J_{ex,1,2}(T) \cos(\theta_1 - \theta_2) - J_{ex,2,3}(T) \cos(\theta_2 - \theta_3) \\
& + \sum_{i=1}^3 (K_i(T) \sin^2(\theta_i) V_i + M_i(T) H \cos(\theta_i) V_i) .
\end{aligned} \tag{6.2}$$

Exact determination of the critical switching temperature and switching angle required to minimize the energy function demands solving complicated and coupled expressions

of derivatives involving  $dE/d\theta_i$  and  $d^2E/d\theta_i^2$ , where  $i = 2, 3$ . Instead, a straightforward way is to determine the critical temperature by visualizing the energy contour plots at varying temperatures until the local energy extremes disappear. Based on the energy barrier associated with critical energy extremes at different temperatures, the temperature dependence of thermal activation energy can be fitted, from which the switching mechanism and switching angles of  $\theta_i$  for middle and FePt layers can be determined.

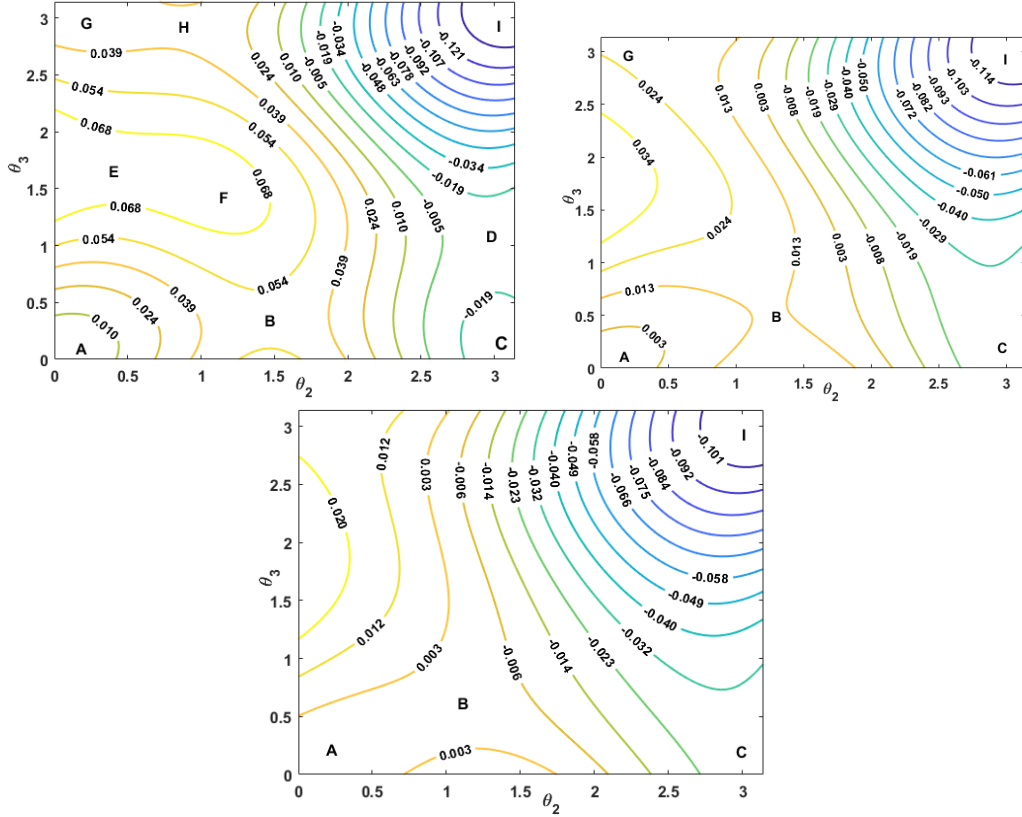


Figure 6.3: Energy contour plots for 3ly-model at  $T = 420\text{K}$  (a),  $T=450\text{K}$  (b) and  $T=475\text{K}$  (c) from left to right, where critical points are labeled from A to I.  $H_{appl}=7400$  Oe.  $M_1(T) = 1600(1-T/560)^{1/3}$ ,  $K_1(T) = 2.4 \times 10^7(1-T/560)$ .  $M_2(T) = 460(1-T/500)^{1/3}$ ,  $K_2(T) = 7.4 \times 10^7(1-T/500)$ .  $M_3(T) = 1100(1-T/500)^{1/3}$ ,  $K_3(T) = 7.0 \times 10^7(1-T/500)$ .  $J_{ex,1,2}/V = 4.8 \times 10^6 \text{erg/cm}^3$  and  $J_{ex,2,3}/V = 4.6 \times 10^6 \text{erg/cm}^3$ . Note all the energy is scaled with  $E/Ku_{3,0}V$ .

Fig. 6.3 illustrates the evolution of the critical points labeled in the energy contour plots with respect to temperature. Points A, C, G and I label the local minima around  $(0,0)$ ,  $(\pi,0)$ ,  $(0, \pi)$  and  $(\pi, \pi)$  respectively. F labels the local maximum around  $(\pi/2, \pi/2)$ . Four saddle points occurring around  $(\pi/2, 0)$ ,  $(0, \pi/2)$ ,  $(\pi/2, \pi)$  and  $(\pi, \pi/2)$  are denoted with B, E, D and H respectively. As temperature further increases, Point E and Point F merge first as shown in Fig. 6.3(b) and the energy barrier AB diminishes to zero at the switching temperature as shown in Fig. 6.3(c).

Similarly, the switching energy barrier and energy barrier gradient of the 2ly-model can also be evaluated as shown in Fig. 6.4. For comparison, the FePt with double volume in 2ly-model is treated as two layers with the same temperature-dependence magnetic parameters. Comparing the magnitude of energy barrier between critical points,  $\Delta E_{AB}/\Delta E_{AF} \leq 50\%$  for the selected temperature 25K below the critical temperature as shown in Fig.6.3(b). Thus, the switching process is most likely to occur via the perpendicular propagation of a domain wall where the switching of the top layer drives the switching of FePt via the middle layer. The middle layer first overcomes the energy barrier between point A around  $(0,0)$  to point B around  $(\pi/2, 0)$  and reaches the local minimum at point C around  $(\pi, 0)$ , followed by the switching of FePt from  $(\pi, 0)$  to  $(\pi, \pi)$  by overcoming the energy barrier between point C and point D around  $(\pi, \pi/2)$ . As the primary energy barrier (AB)  $\Delta E_{AB}$  is at least 3.5 times larger than secondary energy barrier (CD)  $\Delta E_{CD}$ , the switching of the middle layer and FePt are dominantly determined by energy barrier AB.

An identical switching process is observed in the 2ly-model as shown in Fig. 6.4, where the middle-layer FePt switches first to the state around  $(\pi, 0)$  and the bottom FePt follows by overcoming barrier CD to reach the final equilibrium states  $(\pi, \pi)$ . Note that the  $\Delta E_{AB}$  in the 2ly-model diminishes slower than that in the 3ly-model. As shown in Fig. 6.4(a), Point E and Point F merge around 420K rather than 450K in the 3ly-model of Fig. 6.3(b) and yet  $\Delta E_{AB}$  still diminishes to zero around 475K. Given that the thermal and magnetostatic energy are not included in the calculation, unlike the actual media, the switching temperature between 3ly-model and 2ly-model differ slightly by 6K.

Based on the energy contour plots,  $\Delta E_{AB}$  is determined with respect to different temperatures below the critical temperature as shown in Fig. 6.5. The fitting function

is in the form of  $\Delta E_z + \Delta E_{ani} + \Delta E_{ex}$  for all layers included as given in equation 6.3, assuming that  $\theta_1$  is fully reversed to align with the applied field and the initial state of  $\theta_{2,0}$  and  $\theta_{3,0}$  is (0,0).

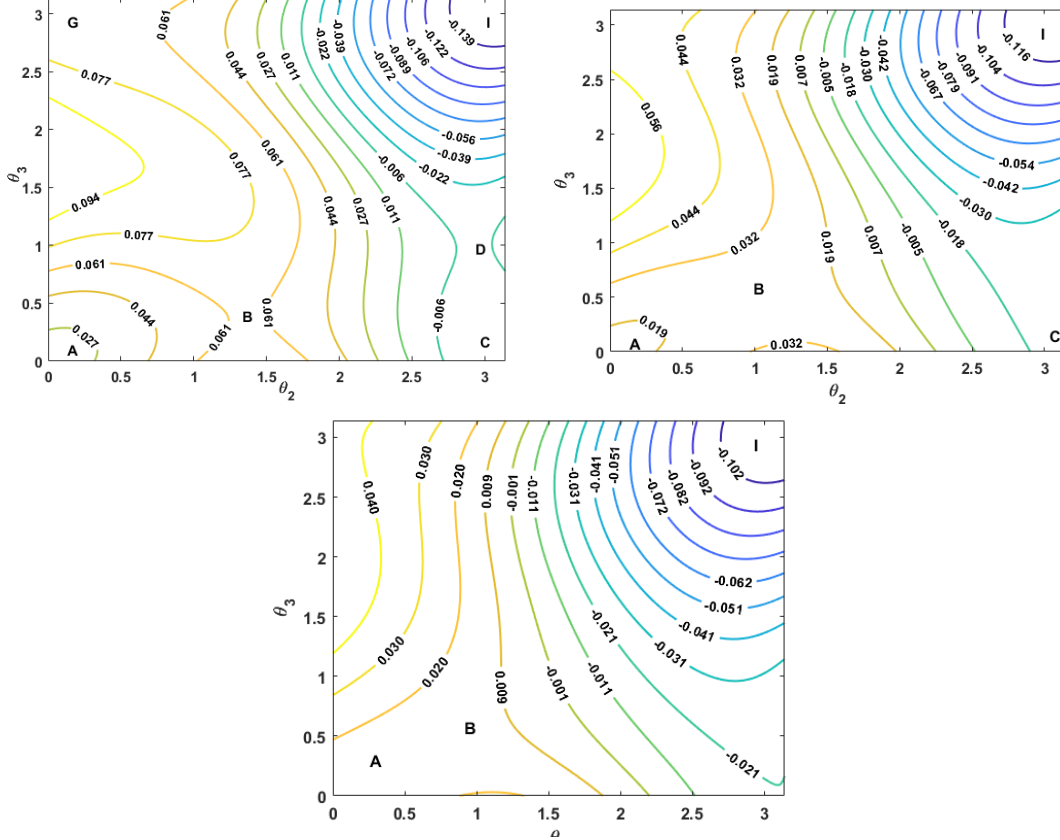


Figure 6.4: Energy contour plots for 2ly-model at  $T = 420\text{K}$  (a),  $T=450\text{K}$  (b) and  $T= 470\text{K}$  (c) from left to right, where critical points are labeled from A to I.  $H_{appl}=7400$  Oe.  $M_1(T) = 960(1-T/600)^{1/3}$ ,  $K_1(T) = 1.8 \times 10^7(1-T/600)$ .  $M_2(T) = 1100(1-T/500)^{1/3}$ ,  $K_2(T) = 7.0 \times 10^7(1-T/500)$ .  $M_3(T) = 1100(1-T/500)^{1/3}$ ,  $K_3(T) = 7.0 \times 10^7(1-T/500)$ .  $J_{ex,1,2}/V = 4.5 \times 10^6 \text{erg/cm}^3$  and  $J_{ex,2,3}/V = 5.3 \times 10^6 \text{erg/cm}^3$ . Note all the energy is scaled with  $E/Ku_{2,0}V$ .

$$\begin{aligned}
\Delta E_z + \Delta E_{ani} &= \sum_{i=1}^3 K_i(T) (\sin^2(\theta_{i,sw}) - \sin^2(\theta_{i,0})) \\
&\quad + M_i(T) H(\cos(\theta_{i,sw}) - \cos(\theta_{i,0})), \\
\Delta E_{ex} &= \sum_{i=1}^3 \Delta E_{ex,ij} \\
&= -J_{ex,i,j}(T) \cos(\theta_{i,sw} - \theta_{j,sw}) \\
&\quad + J_{ex,i,j} \cos(\theta_{i,0} - \theta_{j,0}).
\end{aligned} \tag{6.3}$$

Based on the fitting curve, the switching angles of  $\theta_2$  and  $\theta_3$  are 1.266 (72.5°) and 0.287 (16.4°) respectively for the 3ly-model.

In contrast, the switching angles associated with the primary energy barrier for the 2ly-model are (1.059, 0.287) (60.7°, 16.4°). Given that the energy barrier gradient is given as

$$\frac{d(\Delta E)}{dx} = \frac{d(\Delta E)}{dT} \times \frac{dT}{dx},$$

taking the derivative of the fitting curve with respect to temperature  $d(\Delta E)/dT$  (shown in the inset of Fig. 6.5) illustrates the relative magnitude of energy gradient  $d(\Delta E)/dx$  for 3ly and 2ly models, considering  $dT/dx$  evaluated in the vicinity of switching temperature changes slowly with respect to  $T$ . As

$$\sigma_{jitter} \sim \frac{\delta E}{(|d(\Delta E)|/(dT) \times dT/dx)}. \tag{6.4}$$

then  $d(\Delta E)/dT$  can be understood as an indication of resilience to the variation of transition position with respect to temperature. Assuming  $\delta E$  determined by thermal energy evaluated at the switching temperature is approximately constant for both 2ly and 3ly-model, and thus the 3ly-model with a larger  $|d(\Delta E)/dT|$  has a better transition jitter than the 2ly-model.

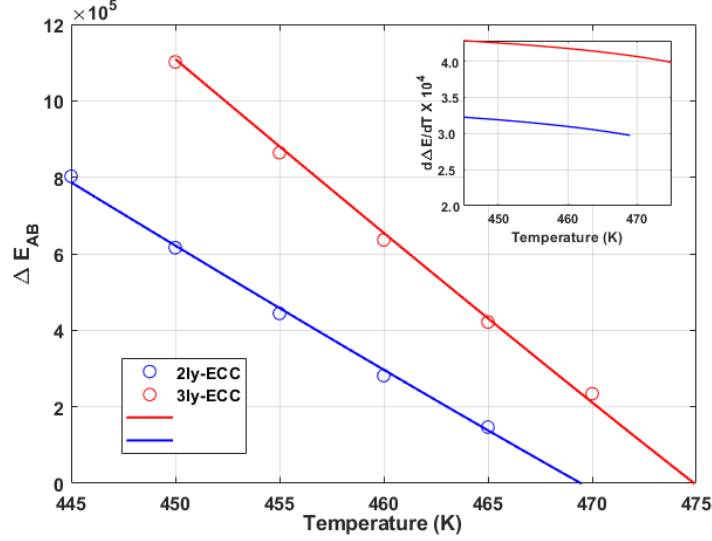


Figure 6.5: The energy barrier AB  $\Delta E_{AB}$  varies with temperature for 3ly-model in red and 2ly-model in blue. Inset: derivative of the fitting function of  $\Delta E_{AB}(T)$ .

As shown in Fig. 6.5, the energy barrier gradient associated with 3ly-model is about  $\sim 40\%$  higher than that of 2ly-model, which can be attributed to the switching angle, anisotropy and saturation magnetization of the middle layer. Note that the dominant contribution in the expression of  $|d(\Delta E)/dT|$  is approximately

$$\left( K_0 \sin^2(\theta_{2,sw}) - \frac{1}{3} H M_0 (1 - \cos(\theta_{2,sw})) \right) / T_c,$$

owing to the larger switching angle and anisotropy of the middle layer compared to the FePt layer. This expression suggests that sharp transitions benefit from high  $K_u$ , small  $M_s$  and low  $T_c$ . Note that despite the same anisotropy in the middle layer of 3ly-ECC and 2ly-ECC at 300K, the  $K_0$  is slightly higher in the middle layer than that in FePt layer for 3ly-ECCs owing to the variation in exchange stiffness from the smaller saturation magnetization  $M_{s2}$ . Moreover, the switching angle in 3ly-ECC is larger than that in the FePt of 2ly-ECC, which can be attributed to the stronger anisotropy field in the middle layer of 3ly-model. Combining these two factors, equation 6.4 reveals 85% improvement in  $|d(\Delta E)/dT|$  and the rest of 15% can be explained by the contributions from exchange coupling. As a result, the primary  $|d(\Delta E)/dT|$  in the 3ly-ECC guarantees sharper transitions than that for 2ly-ECC, improving transition jitters as indicated by

equation 6.4 in spite of  $\sim 6\text{K}$  difference in switching temperature between 3ly-ECC and 2ly-ECC, which merely varies  $\delta E$  by  $\sim 1\%$  and  $dT/dx$  by  $\sim 3\%$ . Overall,  $|d(\Delta E)/dT|$  is the most dominant factor for the jitter improvement, though overall transition jitter improvement will be diluted by erasure-after-write effect and other media characteristics such as Voronoi grain size distribution [160].

### Notes on the analytical explanation

Recall that the switching temperature of the ECC structure determined by SPD is  $\sim 495\text{ K}$ , which is approximately  $25\text{ K}$  higher than that determined by the analytical model. This discrepancy can be attributed to the presence of constant cooling rate in the SPD simulation, which facilitates the higher-temperature switching of the entire medium. Generally, the switching process is roughly initiated when the temperature-dependent anisotropy field  $H_k$  equals to constant head field  $H_w$ , i.e.  $H_k = H_w$ . In fact, owing to the presence of decreasing temperature, the thermal agitation field can promote this process to occur at a higher temperature, even though the random thermal field direction averages to zero over time. Note that, however, the magnitude of thermal field  $|H_{th}| \propto \sqrt{T(t)}$  decreases over time during switching process. As a result, some randomized thermal agitation field can first assist in initiating the switching and then be suppressed by the decreasing temperature, locking in the switching against reversal along with the elevated anisotropy field. This effect is pronounced especially in the vicinity of the Curie temperature, driving the switching of the entire medium to occur at a higher temperature. In contrast, the writing temperature based on the analytical model is determined in a static process with a fixed temperature. Hence, the switching can occur only when the overall thermal agitation is sufficiently large to overcome the energy barrier, leading to a smaller writing temperature. Nevertheless, the overall impact of constant cooling rate on 2-layer and 3-layer structure is roughly the same. Despite the difference in writing temperature between the dynamic process (constant temperature decline) and the static process, the analytical argument remains valid. It is observed that this analytical argument does not effectively explain the variation in jitters for different 3ly-ECC configurations shown in Table 6.1, 6.2 and 6.3. As indicated in the analytical argument, higher  $Ku_2$  and smaller  $Ms_2$  and  $T_{c1}$  (less thermal fluctuation) improve jitters.

However, it is not always the case as in Table 6.1, 6.2 and 6.3. First, given that  $Ku_2$  the dominant energy scale in the argument of  $|d(\Delta E)/dT|$ , only varies  $\sim 10\%$  in Table 6.1, 6.2 and 6.3, it is reasonable to expect that jitter is more susceptible to the switching angle which is determined by the specific configuration of the whole structure rather than  $Ku_2$ . Moreover, the assumption of  $\theta_1 = \pi$  is ill-justified when taking erasure-after-write effect and thermal fluctuations into account. This is supported by the fact that a clear decreasing trend of jitter with higher  $Ku_2$  occurs at higher  $Ku_1$ , which can effectively suppress the erasure-after-write effect. In addition, further lowering  $Tc_1$  may also invalidate the assumption of  $\theta_1 = \pi$  as a smaller thermal gradient reduces the efficiency of top layer switching. Thus, the decline in switching temperature of the top layer undermines contribution of the exchange field, degrading jitters.

### 6.3.2 Erasure-After-Write effect

To further evaluate the recording performance of 3ly-ECCs, EAW effects are also studied with 2ly-ECC and four proposed 3ly-structures at  $BL = 21$  nm. For each bit written in the single tone pattern, the number of grains erased during the cooling process is calculated to serve as an EAW measure. Note that due to the lagging response of different layers to the Gaussian thermal profile, the recording moment is chosen based on the recording of the top layer for consistency. The switching status of each grain is determined by the majority switching status of each cell within one grain. Note that the EAW in the top layer and FePt layer is  $\sim 2\%$  difference owing to different anisotropy fields in these two layers.

Table 6.6: Summary of EAW for 3Lys and 2Ly-ECC in the Presence/Absence of IGE.

ECC	IGE=0%		IGE=5%		$2Ku_1/Ms_1$ ( $10^4$ Oe)	$2\overline{Ku}/\overline{Ms}$ ( $10^4$ Oe)
	top layer	FePt	top layer	FePt		
2ly	1.13	1.10	0.68	0.66	2.86	5.52
3ly-A	3.32	3.24	1.77	1.68	1.69	5.33
3ly-B	2.21	2.16	1.32	1.23	2.31	5.64
3ly-C	2.23	2.16	1.12	1.02	2.31	5.82



3ly-D	1.36	1.38	0.78	0.74	2.77	6.38
-------	------	------	------	------	------	------

Based on Table 6.6, the 3ly-ECCs are more susceptible to EAW, approximately varying from 20% to  $\sim 30\%$  worse than the 2ly-ECC when  $BL = 21$  nm. In particular, 3ly-A shows the strongest EAW, which causes the worst jitter in 3ly-A. In contrast, 3ly-D shows the strongest tolerance to EAW among all the 3ly-configurations in the presence/absence of IGE. In Table 6.6, the ratio of  $2Ku/Ms$  and average ratio of  $2Ku/Ms$  are listed for the writing layer and layers above the bottom FePt, respectively. It is revealed that EAW is strongly related to anisotropy field of the top layer. The trend of  $2Ku/Ms$  suggests that the soft top layer is responsible for the susceptibility to EAW in the 3ly-ECCs without IGE.

Comparing 3ly-C with 3ly-B suggests, for the same ratio of anisotropy of top layer, a larger  $T_{c1}$ /smaller anisotropy field above the FePt layer worsens the EAW due to thermal noise associated with a higher writing temperature above FePt. Although the overall writing temperature of 3ly-B and 3ly-C is within 2%, the switching temperature associated with different layers varies. For the case without IGE, as the higher  $T_{c1}$  of 3ly-B, the top layer of 3ly-B switches at higher temperature which introduces the thermal noise to the switching of the middle layer via interlayer exchange. However, it is also possible that the weaker anisotropy field can also results in thermal instability. Consider the variation of average anisotropy is within 3% vs 7% variation in  $T_{c1}$ , the dominant cause could be both, especially for the case with IGE.

Given that  $Ms_1$  and  $Ku_2$  are fixed, it is suggestive that reduced  $Ms_2$  and  $T_{c1}$  and larger  $Ku_1$  benefit EAW. However, a larger  $Ku_1$  may decrease the switching efficiency as indicated by the increased jitter in 3ly-D. Although IGE can be helpful in both aspects, the metallic grain boundary caused by introduction of IGE can undesirably affect the local thermal gradient, reducing overall recording quality. Accordingly, based on the previous discussion, future progress can be made by optimizing the following two strategies to improve the overall recording performance of 3ly-ECC: a) a reduced  $Ms_2$  while preserving top switching, b) a higher  $Ku_1$  while maintaining the ease of switching in the top layer.

### 6.3.3 Switching Rate

To further investigate the reduction in transition jitters of 3ly-ECCs, the switching rate as a function of temperature is analyzed in the presence/absence of IGE. An external applied field of 8000 Oe is turned on along +z direction to initiate the switching process, with the initial states of the magnetization in the ECC structures pointing in the opposite direction. Note that in order to explore the spin dynamics initiated by Zeeman effect, thermal gradient in the recording process is removed such that the entire switching process occurs at constant temperatures. Switching rate is determined by the time required to reach an average normalized magnetization of 0.5 on average from the initial state of -1. Fig. 6.6 illustrates the comparison of the switching rates for the top layer between 2ly-ECC and 3ly-ECCs with/without IGE. Overall, the switching rate is improved with the reduction of coercivity except at temperatures near  $T_c$ , where it is suppressed by thermal fluctuation.

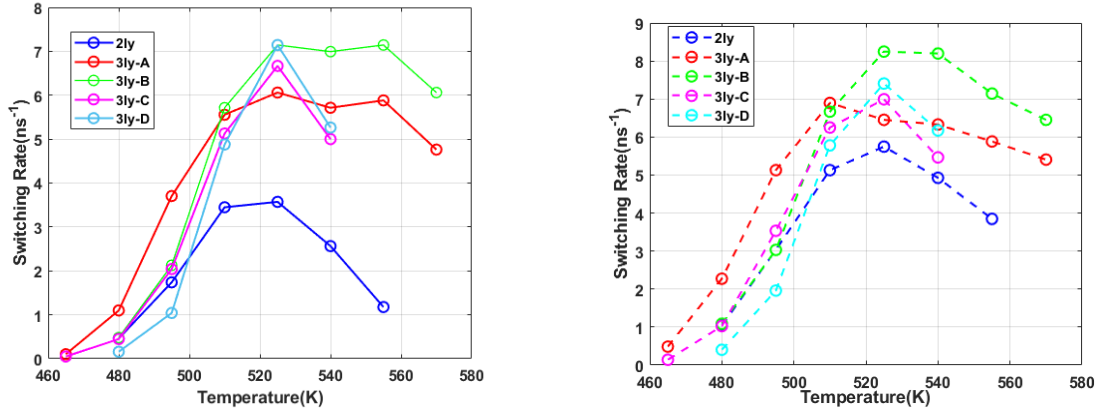


Figure 6.6: (a) Switching rate comparisons between 2ly-ECC and 3ly-ECCs in absence of IGE. (b) Switching rate comparison between 2ly-ECC and 3ly-ECCs in the presence of 5% IGE.

As shown in Fig. 6.6, 3ly-ECC consistently switches faster than 2ly-ECC with/without IGE when temperature are above 500 K. This is dominantly attributed to Zeeman field in the head with a higher  $M_s$  in the top layer of 3ly-ECCs. In addition, a smaller anisotropy field due to softer magnetic top layer and larger magnetization also promotes the faster switching of the entire structure. This positive correlation between

switching rate and  $2\text{Ku}/\text{Ms}$  is more pronounced when  $T < 500\text{ K}$ , exhibiting the identical trend as  $2\text{Ku}/\text{Ms}$  given in Table. 6.6. Similarly, compared to the other 3ly-ECCs, 3ly-A with the smallest  $2\text{Ku}/\text{Ms}$  is more susceptible to thermal fluctuation, resulting in a smaller switching rate. Note that when  $T < 500\text{ K}$ , the slower switching rate of 3ly-D compared to 2ly-ECC results from the higher anisotropy field in the middle layer, which inhibits the switching of the top layer via exchange coupling. Fast response to the effective fields implies fast propagation of the domain wall. Under the assumption of no variations in media characteristics, transitions are expected to complete at a shorter period of time. Therefore, during the recording process, three-layer media switches more accurately because there is less chance of media exposure to variations in thermal gradient and a higher probability of experiencing a single head field. In contrast, switching takes longer to achieve for the two-layer structure, which potentially make the 2ly-ECC more susceptible to variations in recording conditions that compromise the switching accuracy and ultimately result in larger jitters.

Nuances can be discerned despite nearly identical transition jitters observed for 3ly-A and 3ly-D: the rapid switching of 3ly-A and its large middle-layer  $d|Hk|/dx$  may have promoted a sharp transition, but is degraded by stronger EAW; conversely, larger middle-layer  $d|Hk|/dx$  can alleviate slower switching which could have compromised transition jitter. In the presence of 5% IGE, the overall switching rate is increased by  $\sim 15\%$  for 3ly-ECCs and  $\sim 50\%$  for 2ly-ECC. However, the corresponding jitter is only improved by  $\sim 5\%$  suggesting that the other effects dilute the contributions from fast switching, such as the EAW.

#### 6.3.4 BER

Bit error rate is also calculated with 2ly-ECC and 3ly-ECC media and compared at different SSSs in the presence/absence of IGE. In general, smaller SSS improves BER as expected. In absence of IGE, BER for 3ly-ECCs are better than that of 2ly-ECC. In particular, as illustrated in Fig. 6.7 and Table 6.7, 3ly-C shows  $\sim 85\%$  improvement in BER at  $\text{SSS} = 16\text{ nm}$  compared to 2ly-ECC. Note the 50% overlap in error bars between 3ly-A and 2ly-ECC at  $\text{SSS} = 22\text{ nm}$ , which can be explained by statistical uncertainty. Consistent with the trend in jitter, BER for 3ly-A and 3ly-D are higher than that in 3ly-B and 3ly-C by at least 50% when  $\text{SSS} \leq 16\text{ nm}$ . However, the effect of IGE on

3ly-ECC is inconclusive. IGE improves BER for 3ly-A by  $\sim 40\%$ , but yet only shows consistent improvement for all 3ly-ECCs with  $SSS = 11$  nm. As a result, in the best case, BER in 3ly-C is  $\sim 70\%$  better than BER in 2ly-ECC in the presence of 5% IGE. Overall, in the absence of IGE, BER favors 3ly-B and 3ly-C owing to a better trade-off between EAW and ease of switching.

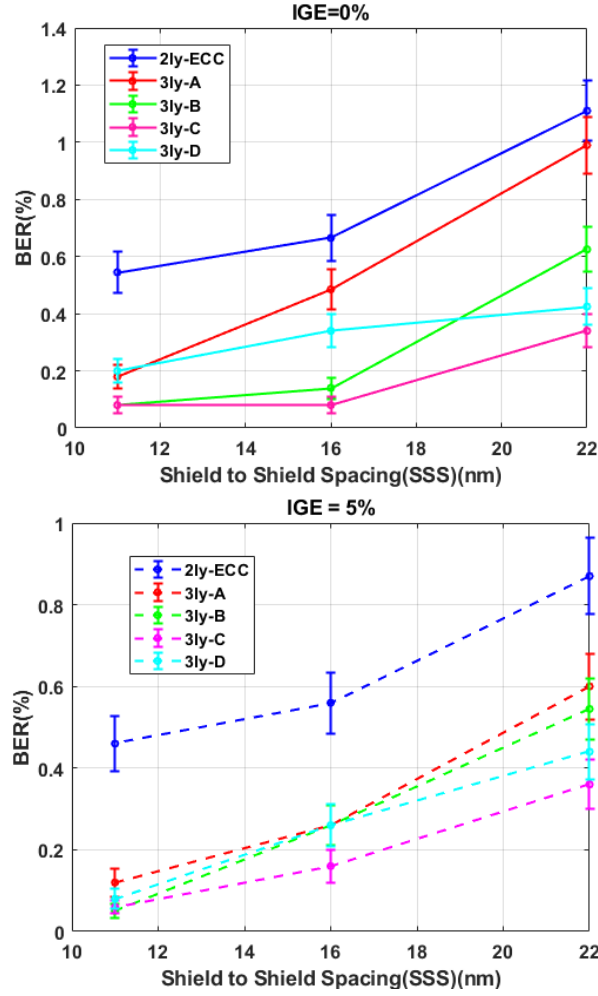


Figure 6.7: (a) BER comparisons between 2ly-ECC and 3ly-ECCs in absence of IGE.(b) BER comparison between 2ly-ECC and 3ly-ECCs in the presence of 5% IGE.

Table 6.7: Summary of BERs of 3LYs and 2LY-ECC at Different Shield to Shield Spacing with IGE = 0 and 5%.

ECC	SSS(nm)					
	22	16	11	22	16	11
	IGE=0%			IGE=5%		
2ly	1.11(0.21)	0.67(0.16)	0.55(0.15)	0.87(0.19)	0.56(0.15)	0.46(0.14)
3ly-A	0.99(0.20)	0.49(0.14)	0.18(0.09)	0.60(0.16)	0.26(0.10)	0.12(0.07)
3ly-B	0.63(0.16)	0.14(0.08)	0.08(0.06)	0.55(0.15)	0.26(0.10)	0.05(0.03)
3ly-C	0.34(0.12)	0.08(0.06)	0.08(0.06)	0.36(0.12)	0.16(0.08)	0.06(0.04)
3ly-D	0.43(0.13)	0.34(0.12)	0.20(0.09)	0.44(0.13)	0.26(0.10)	0.08(0.05)

### 6.3.5 SPD

As shown in Fig. 6.8, 5% IGE improves FWHM by at least 20% and yet the FWHMs of 3ly-ECCs vary within 10% of 2ly-FWHM in the presence/absence of IGE, which is not consistent with jitters nor BERs. Note that FWHMs of 3ly-ECCs show the same trend as the top layer ratio of 2Ku/Ms in Table 6.6, in particular in the presence of 5% IGE. This suggests that in the SPD calculation, the sharp transitions of 3ly-ECCs are driven by the easy switching of the writing layers. Moreover, the inconsistent trend between FWHM and jitters can be attributed to the absence of EAW effect in the SPD calculation. Recall that the SPD is designed to model the transition with a statistical average of switching status with multiple grains by just a single applied field reversal. Thus, SPD provides no information of EAW effect on switching performance for ECC media during the cooling process. In addition, the constant cooling rate used in SPD is not well-justified to reflect the switching quality of the grains at the center of the heat spot, which can also lead to discrepancies between FWHM and other noise measures.

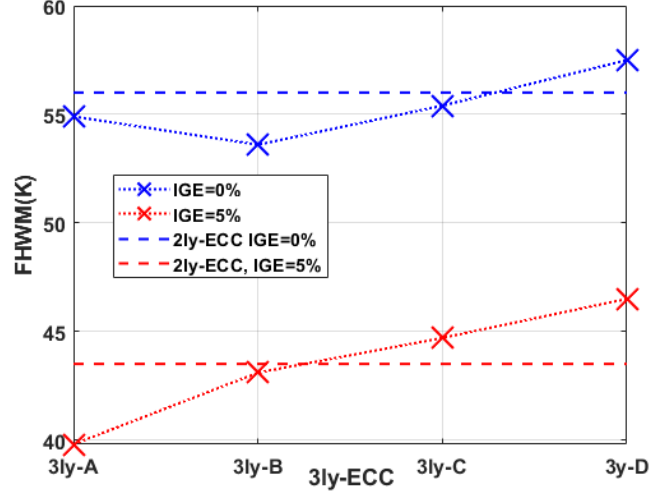


Figure 6.8: FWHM comparison between 2ly-ECC and 3ly-ECCs with/without IGE.

## 6.4 Conclusion

In this section, 3ly-ECC media are proposed to optimize the HAMR performance evaluated with transition jitters, erasure-after-write effect, bit error rate and SPD at low operating temperature. It is found that compared to 2ly-ECC, the proposed 3ly-ECCs effectively reduce transition jitter by  $\sim 15\%$  and BER by  $\sim 85\%$  in the absence of intergranular exchange. The analysis of energy function with a simple spin model demonstrates that large anisotropy and small magnetization in the middle layer are responsible for the improvement in transition jitters of 3ly-ECCs. In addition, exploration of the switching rate at a constant temperature suggests that fast switching can potentially contribute to jitter improvement at the expense of enhanced EAW. It is also found that the 3ly-ECC is more susceptible to erasure-after-write effect than 2ly-ECC: the most tolerant 3ly-ECC to EAW is still 20% worse than 2ly-ECC. Calculations indicate that the suppression of EAW in 3ly-ECCs relies on the increase in the anisotropy of writing layer which adversely affects BER due to the loss of rapid switching. Overall, the 3ly-ECCs effectively balance fast switching and EAW, showing superior jitter and BER. The results suggest the importance of investigating and developing suitable high-Ku and low-Ms magnetic media.

# References

- [1] A. Hirohata, K. Yamada, Y. Nakatani, I. Prejbeanu, B. Diény, P. Pirro and B. Hillebrands, Review on spintronics: Principles and device applications, *JMMM*, vol. 509, 166711, Sept. 2020
- [2] S. A. Wolf et al., Spintronics: A Spin-Based Electronics Vision for the Future, *Science*, vol. 294, 1488-1495, 2001
- [3] M.N. Baibich, J.M. Broto, A. Fert, F.N. Van Dau, F. Petroff, P. Eitenne, et al., Giant magnetoresistance of (001)Fe/(001)Cr magnetic superlattices, *Phys. Rev. Lett.*, vol. **61**, p. 2472 (1988), p. 2472
- [4] G. Binasch, P. Grünberg, F. Saurenbach, W. Zinn, Enhanced magnetoresistance in layered magnetic structures with antiferromagnetic interlayer exchange, *Phys. Rev. B*, **39**, 4828. (1989)
- [5] Wikipedia, “Giant magnetoresistance — Wikipedia, the free encyclopedia,” 2021. [Online].
- [6] N.F. Mott, Electrons in transition metals, *Adv. Phys.*, **13**, p. 325, (1964)
- [7] T. Valet, A. Fert, Theory of perpendicular magnetoresistance in magnetic multilayers, *Phys. Rev. B*, **48**, p. 7099. (1993)
- [8] J. Barnaś, A. Fuss, R. E. Camley, P. Grünberg, and W. Zinn. Novel magnetoresistance effect in layered magnetic structures: Theory and experiment. *Phys. Rev. B* **42**, 8110 (1990).

- [9] M. A. M. Gijs. *Experiments on the Perpendicular Giant Magnetoresistance in Magnetic Multilayers*, pages 129–177. Springer Berlin Heidelberg, 2000.
- [10] W. P. Pratt, S.-F. Lee, J. M. Slaughter, R. Loloee, P. A. Schroeder, and J. Bass. Perpendicular giant magnetoresistances of Ag/Co multilayers. *Phys. Rev. Lett.*, **66**:3060–3063, Jun 1991.
- [11] Kees M. Schep, Paul J. Kelly, and Gerrit E. W. Bauer. Giant magnetoresistance without defect scattering. *Phys. Rev. Lett.* **74**:586–589, Jan 1995.
- [12] P.M. Levy, in *Solid State Physics Series*, edited by H. Ehrenreich and D. Turnbull (Academic Press, New York, 1994) vol.41, p. 367
- [13] J. Barnaś, A. Fert, Interfacial scattering and interface resistance for perpendicular transport in magnetic multilayers, *J. Magn. Magn. Mater.*, **136** (1994), p. 260
- [14] M. Johnson and R.H. Silsbee, Interfacial charge-spin coupling: Injection and detection of spin magnetization in metals, *Phys. Rev. Lett.* **55**, 1790 (1985)
- [15] M. Johnson, *Phys. Rev. Lett.*, **67** (1993), p. 3594
- [16] F.J. Jedema, A.T. Filip, and B.J. van Wees, Electrical spin injection and accumulation at room temperature in an all-metal mesoscopic spin valve, *Nature* **410**, 345 (2001).
- [17] T. Nakatani, Z. Gao, and K. Hono, Read sensor technology for ultrahigh density 117 magnetic recording, *MRS Bull.* **43**, 106 (2018)
- [18] M. Takagishi, K. Yamada, H. Iwasaki, H.N. Fuke, and S. Hashimoto, Magnetoresistance Ratio and Resistance Area Design of CPP-MR Film for 2–5 Tb/in<sup>2</sup> Read Sensors, *IEEE Trans. Magn.* **46**, 2086 (2010). )RA figure)
- [19] A.W. Overhauser, *Phys. Rev. B* **89** 689,1953
- [20] Žutić I,J. Fabian and S. Sarma Das *Rev. Mod. Phys.* **76** 323(2004)
- [21] H.C.Torrey, ‘Bloch equations with diffusion terms,’ *Phys. Rev.* **104**, 563–565,1956,



- [22] R.J. Elliott, Theory of the effect of spin-Orbit coupling on magnetic resonance in some semiconductors, *Phys. Rev.* **96**, 266 (1954).
- [23] Y. Yafet, in Solid State Phys., edited by F. Seitz and D. Turnbull (Academic, New York, 1963), pp. 1–98
- [24] M. P. M. Dean, Y. Cao, X. Liu, S. Wall, D. Zhu, R. Mankowsky, V. Thampy, X. M. Chen, J. G. Vale, D. Casa et al., *Nat. Mater.* **15**, 601 (2016).
- [25] F. Meier and B. P. Zakharchenya, Optical Orientation (Elsevier, Amsterdam, 2012).
- [26] T. Miyamoto, Y. Matsui, T. Terashige *et al.* Probing ultrafast spin-relaxation and precession dynamics in a cuprate Mott insulator with seven-femtosecond optical pulses. *Nat. Commun.* **9**, 3948 (2018).
- [27] A. Avsar, H. Ochoa, F. Guinea, B. Özyilmaz, B. J. van Wees, and I. J. Vera-Marun, *Rev. Mod. Phys.* **92**, 021003 (2020)
- [28] D. Hägele, S. Döhrmann, J. Rudolph and M. Oestreich, *Adv. Solid State Phys.*, **45** 253 (2005)
- [29] A. Baral et al, Re-examination of the Elliott–Yafet spin-relaxation mechanism, *New J. Phys.*, **18**, 023012 (2016)
- [30] P. Monod and F. Beuneu, Conduction-electron spin flip by phonons in metals: Analysis of experimental data, *Phys. Rev. B* **19**, 911 (1979)
- [31] T.W. Griswold, A.F. Kip, and C. Kittel, Microwave Spin Resonance Absorption by Conduction Electrons in Metallic Sodium, *Phys. Rev.* **88**, 951 (1952).
- [32] J. D. Watts, L. O’Brien, J. S. Jeong, K. A. Mkhoyan, P. A. Crowell and C. Leighton, Magnetic impurities as the origin of the variability in spin relaxation rates in Cu-based spin transport devices, *Phys. Rev. Mater.* **3**, 124409 (2019)
- [33] J. D. Watts, J. T. Batley, N. A. Rabideau, J. P. Hoch, L. O’Brien, P. A. Crowell, and C. Leighton, Finite-Size Effect in Phonon-Induced Elliott-Yafet Spin Relaxation in Al, *Phys. Rev. Lett.* **128**, 207201 (2022)

- [34] K. T. Raić, An explanation of hillock growth in thin Al films, *Surface Engineering*, 32:11, 823-828 (2016)
- [35] S. Aceto, C.Y. Chang, R.W. Vook, Hillock growth on aluminum and aluminum alloy films, *Thin Solid Films*, 219, 80-86 (1992),
- [36] B.Cao Martin, C.J. Tracy, J.W. Mayer, L.E. Hendrickson, A comparative study of Hillock formation in aluminum films, *Thin Solid Films*, Volume 271, Issues 1-2, 1995, Pages 64-68,
- [37] Y. Shim, V. Borovikov, B. P. Uberuaga, A. F. Voter, and J. G. Amar, *Phys. Rev. Lett.* 101, 116101 (2008).
- [38] M. W. Finnis and V. Heine, *J. Phys. F: Met. Phys.* 4, L37 (1974).
- [39] W. Gruber, S. Chakravarty, C. Baetz, W. Leitenberger, M. Bruns, A. Kobler, C. Kubel, and H. Schmidt, *Phys. Rev. Lett.* 107, 265501 (2011).
- [40] J. Fabian and S. Das Sarma, Phonon-Induced Spin Relaxation of Conduction Electrons 119 in Aluminum, *Phys. Rev. Lett.* 83, 1211 (1999)
- [41] J. Fabian and S. Das Sarma, Spin Relaxation of Conduction Electrons in Polyvalent Metals: Theory and a Realistic Calculation, *Phys. Rev. Lett.* 81, 5624 (1998).
- [42] F. Beuneu and P. Monod, Conduction-electron spin resonance in cold-worked Al, Cu, and Ag: The spin-flip cross section of dislocations, *Phys. Rev. B* 13, 3424 (1976).
- [43] N. Poli, M. Urech, V. Korenivski, and D. Haviland, Spin-flip scattering at Al surfaces. *J. Appl. Phys.*, **99**, 08H701 (2006).
- [44] F. J. Jedema, M. S. Nijboer, A. T. Filip, and B. J. van Wees, *Phys. Rev. B* 67, 085319 (2003).
- [45] H. Idzuchi, Y. Fukuma, and Y. Otani, *Physica E Low Dimens. Syst. Nanostruct.* 68, 239 (2015).
- [46] H. Idzuchi, Y. Fukuma, and Y. Otani, *Physica E Low Dimens. Syst. Nanostruct.* 68, 239 (2015).

- [47] S. Roche and S. O. Valenzuela, J. Phys. D: Appl. Phys. 47, 094011 (2014).
- [48] S. B. Touski and M. Pourfath, Appl. Phys. Lett. 103, 143506 (2013).
- [49] S. B. Touski, R. Roldan, M. Pourfath, and M. Pilar Lopez-Sancho, Phys. Rev. B 95, 165301 (2017).
- [50] G. Mihajlovic, J. E. Pearson, S. D. Bader, and A. Hoffmann, Phys. Rev. Lett. 104, 237202 (2010).
- [51] E. Villamor, M. Isasa, L. E. Hueso, and F. Casanova, Phys. Rev. B 87, 094417 (2013).
- [52] S. Rakheja, S. -C. Chang, and A. Naeemi, IEEE Trans. Electron Devices 60, 3913 (2013).
- [53] A. Matthiessen and C. Vogt, Ann. Phys. 198, 19 (1884).
- [54] K. Moors, B. Sore, Z. Tkei, and W. Magnus, J. Appl. Phys. 116, 063714 (2014)
- [55] J. D. Watts, Ph.D. thesis, University of Minnesota-Twin Cities (2018), retrieved from the University of Minnesota Digital Conservancy, <https://hdl.handle.net/11299/202195>
- [56] K. Fuchs, Math. Proc. Cambridge Philos. Soc. 34, 100 (1938).
- [57] E. H. Sondheimer, Adv. Phys. 1, 1 (1952).
- [58] A. F. Mayadas and M. Shatzkes, Phys. Rev. B 1, 1382 (1970).
- [59] A. F. Mayadas and M. Shatzkes, Phys. Rev. B 1, 1382 (1970).
- [60] R. Landauer, Philos. Mag. **21**, 863 (1969).
- [61] M. Büttiker, Phys. Rev. Lett. **57**, 1761 (1986).
- [62] D. A. Ryndyk, (2016). *Landauer-Büttiker Method. In: Theory of Quantum Transport at Nanoscale*, **184** (Springer, Cham., 2016)
- [63] M.P.Lopez Sancho et al , "Highly convergent schemes for the calculation of bulk and surface Green functions," *J. Phys. F : Met. Phys.*, vol 15, no. 4, pp. 851, 1985.

- [64] W. Harrison, *Elementary electronic structure and the Properties of Solids* (World Scientific, 1999)
- [65] D. A. Papaconstantopoulos, *Handbook of the Band Structure of Elemental Solids* (Plenum, New York, 1986).
- [66] C. Caroli, R. Combescot, P. Nozieres, and D. Saint-James, J. Phys. C: Solid State Phys. 4, 916 (1971).
- [67] T. Kimura, T. Sato, and Y. Otani, Phys. Rev. Lett. 100, 066602 (2008).
- [68] H. Zou and Y. Ji, Appl. Phys. Lett. 101, 082401 (2012).
- [69] R. L. Graham et al., Appl. Phys. Lett. 96, 042116 (2012).
- [70] A. Vogel, J. Wulforth, and G. Meier, Appl. Phys. Lett. 94, 122510 (2009).
- [71] L. Kiss, J. Sderlund, G. Niklasson, and C. Granqvist, Nanotechnology 10, 25 (1999).
- [72] N. W. Ashcroft and N. D. Mermin, *Solid State Physics* (Saunders College Publishing, 1976).
- [73] P. Y. Zhang, T. Zhou, B. Engler, J. Chawla, R. Hull, and D. Gall, J. Appl. Phys. 122, 095304 (2017).
- [74] P. Prange and T.-W. Nee, Phys. Rev. 168, 779 (1968).
- [75] S. Valenzuela and M. Tinkham, Appl. Phys. Lett 85, 5914 (2004).
- [76] S. Valenzuela and M. Tinkham, Nature 442, 176 (2006).
- [77] C. H. L. Quay, D. Chevallier, C. Bena, and M. Aprili, Nat. Phys. 9, 84 (2013).
- [78] M. Urech, V. Korenivski, N. Poli, and D. Haviland, Nano Lett. 6, 871 (2006).
- [79] M. Yamamoto et al., Micromachines 11(5), 454 (2020).
- [80] Z.Q. Chen, W.C. Tian, X.T. Zhang, and Y. K. Wang, J. Micromech. Microeng. 27, 113003 (2017).

- [81] J. Ding et al., *Nanoscale* 48, 23449 (2019). [50] J. Mkinen et al., *Surf. Sci.* 175, 385 (1986)
- [82] J. Mkinen et al., *Surf. Sci.* 175, 385 (1986).
- [83] X. Chen and R. H. Victora, *Appl. Phys. Lett.* 93, 162105 (2008).
- [84] P. Esquinazi, J. Barzola-Quiquia, S. Dusari, and N. Garca, *J. Appl. Phys* 111, 033709 (2012).
- [85] E. I. Rashba, *Sov. Phys. Solid State* 2, 1109 (1960).
- [86] Y. A. Bychkov and E. I. Rashba, *JETP Lett.* 39, 7
- [87] Y. J. Cai, C. Qin, F. Kandaz, X. Y. Shen, C. Zhou, M. W. Jia, Y. M. Luo, Y. Z. Wu, and Y. Ji, *Phys. Rev. B* 100, 144419 (2019).
- [88] C. Zhou, F. Kandaz, Y. J. Cai, C. Qin, M. W. Jia, Z. Yuan, Y. Z. Wu, and Y. Ji, *Phys. Rev. B* 96, 094413 (2017)
- [89] O. Smith, Some possible forms of phonograph. *Electrical World*, 1888.
- [90] E. Grochowski. Future technology challenges for NAND flash and HDD products. In *Flash Memory Summit*, 2012.
- [91] "https://idema.org/astc-technology-roadmap/"
- [92] D. R.-J. G.-J. Rydning, "The digitization of the world from edge to core," Framingham: International Data Corporation, 2018.
- [93] Hans Jrgen Richter. Recent advances in the recording physics of thin-film media. *Journal of Physics D: Applied Physics*, 32(21):R147, 1999.
- [94] S. N. Piramanayagam. Perpendicular recording media for hard disk drives. *J. Appl. Phys.*, 102:011301, 2007
- [95] Eric E. Fullerton, D. T. Margulies, M. E. Schabes, M. Carey, B. Gurney, A. Moser, M. Best, G. Zeltzer, K. Rubin, H. Rosen, and M. Doerner. Antiferromagnetically coupled magnetic media layers for thermally stable high-density recording. *Appl. Phys. Lett.*, 77:3806–3808, 2000

- [96] "https://s24.q4cdn.com/101481333/files/doc\_financials/2024/q1/STX-Supplemental-FQ1-24.pdf"
- [97] Wikipedia, "Hard disk drive — Wikipedia, the free encyclopedia," 2021. [Online].
- [98] H J Richter. The transition from longitudinal to perpendicular recording. *J. Phys. D: Appl. Phys.*, 40(9):R149, 2007
- [99] A. Chernyshov et al., "Measurement of Curie temperature distribution relevant to heat assisted magnetic recording", *J. Appl. Phys.*, vol. 117, pp. 17D111, 2015.
- [100] S.N. Piramanayagam and K. Srinivasan. Recording media research for future hard disk drives. *J. Magn. Magn. Mater.*, 321(6):485 – 494, 2009
- [101] H J Richter. The transition from longitudinal to perpendicular recording. *J. Phys. D: Appl. Phys.*, 40(9):R149, 2007.
- [102] S. Iwasaki and K. Takemura. An analysis for the circular mode of magnetization in short wavelength recording. *IEEE Trans. Magn.*, 11(5):1173–1175, Sep 1975.
- [103] Perpendicular Magnetic Recording Technology by HGST (November 2007), available online: [https://www.hgst.com/sites/default/files/resources/PMR\\_white\\_paper\\_final.pdf](https://www.hgst.com/sites/default/files/resources/PMR_white_paper_final.pdf).
- [104] D. Weller, G. Parker, O. Mosendz, A. Lyberatos, D. Mitin, N. Y. Safonova, and M. Albrecht, "FePt heat assisted magnetic recording media," *Journal of Vacuum Science & Technology B, Nanotechnology and Microelectronics: Materials, Processing, Measurement, and Phenomena*, vol. 34, no. 6, p. 060801, 2016.
- [105] Nan Zhou et al. Plasmonic near-field transducer for heat-assisted magnetic recording. *Nanophotonics*, 3:141–155, 2014.
- [106] W. A. Challener, A. V. Itagi C. Peng, D. Karns, W. Peng, Y. Peng, X. Yang, X. Zhu, N. J. Gokemeijer, Y.-T. Hsia, G. Ju, R. E. Rottmayer, M. A. Seigler, and E. C. Gage. Heat-assisted magnetic recording by a near-field transducer with efficient optical energy transfer. *Nature Photon.*, 3:220–224, 2009.

- [107] [https://www.seagate.com/www-content/ti-dm/tech-insights/en-us/docs/TP707-1-1712US\\_HAMR.pdf](https://www.seagate.com/www-content/ti-dm/tech-insights/en-us/docs/TP707-1-1712US_HAMR.pdf)
- [108] T. Klemmer, D. Hoydick, H. Okumura, B. Zhang, and W. A. Soffa, "Magnetic Hardening and Coercivity Mechanisms in L10 Ordered FePd Ferromagnets", *Scripta Metallurgica et Materialia*, vol. 33, pp. 1793-1805, (1995).
- [109] M. H. Kryder et al., "Heat Assisted Magnetic Recording," *Proceedings of the IEEE*, vol. 96, no. 11, pp. 1810-1835, Nov. 2008.
- [110] ] W. -H. Hsu and R. H. Victora, "Micromagnetic Study of Media Noise Plateau in Heat-Assisted Magnetic Recording," *IEEE Transactions on Magnetics*, vol. 55, no. 2, pp. 1-4, Feb. 2019
- [111] ] Y. Jiao, J. Hohlfield, and R. H. Victora, "Understanding transition and remanence noise in HAMR," *IEEE Transactions on Magnetics*, vol. 54, no. 11, pp. 1-5, 2018
- [112] ] J. -G. Zhu and H. Li, "Understanding Signal and Noise in Heat Assisted Magnetic Recording," *IEEE Transactions on Magnetics*, 49(2):765-772, Feb. 2013
- [113] Zengyuan Liu, Pin-Wei Huang, Ganping Ju, and R. H. Victora, "Thermal switching probability distribution of L10 FePt for heat assisted magnetic recording", *Appl. Phys. Lett.*, 110:182405 (2017).
- [114] C. -. Rong et al., "Size-dependent chemical and magnetic ordering in L10-FePt nanoparticles," *Adv. Mater.*, 18(22):2984-2988, 2006.
- [115] R. H. Victora and A. Ghoreyshi, "Optical Analysis of HAMR Media," *IEEE Trans. Magn.*, 55(3):8480864, 2018.
- [116] G. Ju et al., "High density heat assisted magnetic recording media and advanced characterization: progress and challenges", *IEEE Trans. Magn.*, 55(4), 2015.
- [117] T.W. McDaniel, "Ultimate limits to thermally assisted magnetic recording", *J. Phys.: Condens. Matter.*, 17 :R315, 2005.

- [118] C.Vogler, C. Abert, F. Bruckner, D. Suess and D. Praetorius , “Basic noise mechanisms of heat-assisted-magnetic recording”, *J. Appl. Phys.*, 120:153901, 2016.
- [119] Z. Liu and R. H. Victora, ”Composite Structure with Superparamagnetic Writing Layer for Heat-Assisted Magnetic Recording,” *IEEE Transactions on Magnetics*, 52(7):1-4, July 2016
- [120] Z. Liu, Y. Jiao and R. H. Victora, “Composite media for high density heat assisted magnetic recording”, *Appl. Phys. Lett.*, 108: 232402, 2016.
- [121] ] N.A. Natekar, W. Tipcharoen, R.H. Victora, “Composite media with reduced write temperature for heat assisted magnetic recording”, *J. Magn. Magn. Mater.*, 486:165253, 2019.
- [122] N. A. Natekar and R. H. Victora, ”Analysis of Adjacent Track Erasure in the HAMR Media,” *IEEE Transactions on Magnetics*, 57(3): 1-11, March 2021,
- [123] L. Landau and E. Lifshitz, “On the theory of the dispersion of magnetic permeability in ferromagnetic bodies,” in *Perspectives in Theoretical Physics*, pp. 51–65, Elsevier, 1992.
- [124] T. L. Gilbert, “A phenomenological theory of damping in ferromagnetic materials,” *IEEE Trans. Magn.*, 40(6):3443–3449, 2004.
- [125] R. Kikuchi, “On the minimum of magnetization reversal time,” *J. Appl. Phys.*, 27(11): 1352–1357, 1956.
- [126] M. Mansuripur and R. Giles, “Demagnetizing field computation for dynamic simulation of the magnetization reversal process,” *IEEE Trans. Magn.*, 24(6): 2326–2328, 1988.
- [127] W. F. Brown Jr. Thermal fluctuations of a single-domain particle. *J. Appl. Phys.*, 34, 1319–1320 (1963)
- [128] R. H. Victora and P. -W. Huang. Simulation of Heat-Assisted Magnetic Recording Using Renormalized Media Cells. *IEEE Trans. Magn.*, 49(2): 751-757, Feb. 2013



- [129] Xuebing Feng and P. B. Visscher. Coarse-graining LandauLifshitz damping. *J. Appl. Phys.*, 89:6988, 2001.
- [130] M. de Berg, O. Cheong, M. van Kreveld, and M. Overmars, *Computational geometry: algorithms and applications.3rd ed.* (Springer,Berlin, 2008).
- [131] E. N. Gilbert. Random subdivisions of space into crystals. *Ann. Math. Stat.*, 33: 958–972, 1962
- [132] S. W. Sloan and G. T. Houlsby. An implementation of Watson’s algorithm for computing 2-dimensional Delaunay triangulations. *Adv. Eng. Softw.*, 6, 1978. no. 4, pp. 192–197, 1984
- [133] H. J. Richter, C. C. Poon, G. Parker, M. Staffaroni, O. Mosendz, R. Zakai, and B. C. Stipe. Direct measurement of the thermal gradient in heat assisted magnetic recording. *IEEE Trans. Magn.*, 49(10):5378–5381, Oct 2013
- [134] H. N. Bertram, Theory of magnetic recording. Cambridge University Press, 1994.
- [135] C.Vogler, C. Abert, F. Bruckner, D. Suess and D. Praetorius. Heat-assisted magnetic recording of bit-patterned media beyond 10Tb/in2. *Appl. Phys. Lett.*, 108 ,102405 (2016).
- [136] H. Yamane, S. J. Greaves and Y. Tanaka. Heat-Assisted Magnetic Recording on Dual Structure Bit Patterned Media. *IEEE Trans. Magn.*, 57(2): 1-6 (2021).
- [137] W.-H. Hsu and R. H. Victora. Heat-assisted magnetic recording — Micromagnetic modeling of recording media and areal density: A review. *J. Magn. Magn. Mater.*, 563, 169973 (2022).
- [138] S. Hernandez et al., Geometrical Scaling Limits of Heat-Assisted Magnetic Recording. *IEEE Trans. Magn.*, 57(3): 1-5 (2021).
- [139] A. Chernyshov et al. Measurement of Curie temperature distribution relevant to heat assisted magnetic recording. *J. Appl. Phys.*, 117, 17D111 (2015).
- [140] T. W. McDaniel. Ultimate limits to thermally assisted magnetic recording. *J. Phys.: Condens. Matter.*, 17, R315 (2005).

- [141] G. Ju et al. High density heat assisted magnetic recording media and advanced characterization: progress and challenges. *IEEE Trans. Magn.*, 51(2015).
- [142] Z. Liu and R. H. Victora. Composite Structure with Superparamagnetic Writing Layer for Heat-Assisted Magnetic Recording. *IEEE Trans. Magn.*, 52 (7):1-4 (2016).
- [143] Z. Liu, Y. Jiao, and R. H. Victora. Composite media for high density heat assisted magnetic recording. *Appl. Phys. Lett.*, 108, 232402 (2016).
- [144] N. A. Natekar, W. Tipcharoen, and R. H. Victora. Composite media with reduced write temperature for heat assisted magnetic recording. *J. Magn. Magn. Mater.*, 486,165253 (2019).
- [145] N. A. Natekar and R. H. Victora. Analysis of Adjacent Track Erasure in the HAMR Media. *IEEE Trans. Magn.*, 57(3): 1-11 (2021).
- [146] W.-H. Hsu and R. H. Victora. Micromagnetic Study of Media Noise Plateau in Heat-Assisted Magnetic Recording. *IEEE Trans. Magn.*, 55(2): 1-4 (2019).
- [147] Y. Jiao, J. Hohlfield, and R. H. Victora. Understanding transition and remanence noise in HAMR. *IEEE Trans. Magn.*, 54(11): 1–5 (2018).
- [148] J.-G. Zhu and H. Li. Understanding Signal and Noise in Heat Assisted Magnetic Recording. *IEEE Trans. Magn.*, 49(2): 765-772 (2013).
- [149] m S. Hernández et al., Effect of Recording Conditions on the Downtrack Thermal Gradient in Heat-Assisted Magnetic Recording. *IEEE Trans. Magn.*, 54, (11): 1-4 (2018).
- [150] C. Vogler, C. Abert, F. Bruckner, D. Suess, and D. Praetorius. Basic noise mechanisms of heat-assisted-magnetic recording. *J. Appl. Phys.*, 120, : 153901 (2016).
- [151] Z. Liu, P.-W. Huang, G. Ju, and R. H. Victora. Thermal switching probability distribution of L10 FePt for heat assisted magnetic recording. *Appl. Phys. Lett.*, 110: 182405, (2017).
- [152] R. H. Victora and P.-W. Huang. Simulation of Heat-Assisted Magnetic Recording Using Renormalized Media Cells. *IEEE Trans. Magn.*, 49(2): 751-757 (2013).

- [153] N. A. Natekar, Z. Liu, S. Hernandez, and R. H. Victora. SNR improvement by variation of recording and media parameters for a HAMR exchange coupled composite media. *AIP Adv.*, 8(5):7-12 (2018).
- [154] H. N. Bertram, *Theory of magnetic recording*. Cambridge University Press, 1994.
- [155] R. D. Yates and D. J. Goodman, *Probability and stochastic processes: a friendly introduction for electrical and computer engineers*. John Wiley & Sons, 2014.
- [156] K. Xue and R. H. Victora. Dependence of HAMR Transition Curvature on Bit Length. *IEEE Trans. Magn.*, 58 (2): 1-5 (2022).
- [157] R. H. Victora and Xiao Shen. Composite media for perpendicular magnetic recording. *IEEE Trans. Magn.*, 41(2): 537-542 (2005).
- [158] J.-G. Zhu. The Scaling of Signal-to-Noise in Heat Assisted Magnetic Recording. *IEEE Trans. Magn.*, doi: 10.1109/TMAG.2023.3315285.
- [159] N. A. Natekar, W.-H. Hsu, and R. H. Victora. Calculated dependence of FePt damping on external field magnitude and direction. *AIP Adv.*, 7, 056004 (2017).
- [160] N. A. Natekar and R. H. Victora. Analytical Estimation of Transition Jitter for the Heat-Assisted Magnetic Recording Process. *IEEE Magn. Lett.*, 11 :1-4 (2020).